UNIVERSITÉ DE GENÈVE
Département de physique
nucléaire et corpusculaire

FACULTÉ DES SCIENCES
Professeur Alain Blondel
Docteur Lucie Linssen

Mesures de production de la particule neutre et étrange K^0_S dans l'expérience HARP

THÈSE

présentée à la Faculté des sciences de l'Université de Genève
pour obtenir le grade de Docteur ès sciences, mention physique

par

Gersende Prior
de Suisse, originaire de Gollion (VD) et Genève (GE)

Thèse N° 3596

GENÈVE
Atelier de reproduction de la Section de Physique
2005

La Faculté des sciences, sur le préavis de Monsieur A. BLONDEL, professeur ordinaire et directeur de thèse (Département de physique nucléaire et corpusculaire), Madame Lucie LINSSEN, docteur et co-directrice de thèse (CERN - Organisation Européenne de Recherches Nucléaires – Département de physique – Meyrin, Suisse), Messieurs A. CLARK, professeur ordinaire (Département de physique nucléaire et corpusculaire), J. PANMAN, docteur (CERN – Organisation Européenne de Recherches Nucléaires – Département de physique – Meyrin, Suisse), et J. DUMARCHEZ, docteur (Universités de Paris VI et VII – Laboratoire de Physique Nucléaire et de Hautes Energies – IN2P3 – CNRS – Paris, France), autorise l'impression de la présente thèse, sans exprimer d'opinion sur les propositions qui y sont énoncées.

Genève, le 2 février 2005

Thèse - 3596 -

Le Doyen, Pierre SPIERER

Résumé

L'expérience de production hadronique HARP (PS214), a pris des données au synchrotron à protons (PS) de l'Organisation Européenne pour la Recherche Nucléaire (CERN), en 2001 et en 2002. Ces mesures vont servir à différentes fins. D'une part, il est nécessaire de connaître la production de pions à partir de faisceau de protons, afin de choisir le meilleur concept pour les usines à neutrinos. D'autre part, les calculs de flux de neutrinos atmosphériques utilisés par les expériences de mesure d'oscillations de neutrinos doivent être plus précis. Les données de HARP vont aussi servir de prédiction pour la simulation du passage des particules à travers la matière ainsi que pour les faisceaux de neutrinos des expériences MiniBooNE et K2K.
Le but de cette thèse est de fournir une mesure de production de la particule étrange K^0_S à partir des données de HARP. Cette étude présente un intérêt pour les expériences d'oscillations de neutrinos qui utilisent un faisceau produit par un accélérateur. En effet, la contamination en kaons chargés du faisceau produit un bruit de fond de neutrinos de type électronique dans le faisceau de neutrinos muoniques. La connaissance de ce bruit de fond pour les domaines d'énergie de faisceau de HARP et pour différents types de cible est indispensable, afin d'optimiser l'énergie du faisceau de protons primaires, le matériau de la cible et le système de focalisation du faisceau.
Le rapport de thèse est divisé en cinq parties. Dans la première nous décrivons l'utilité pour la physique d'une expérience de production de hadrons, à travers une présentation du Modèle Standard et de ses limites. La deuxième partie est consacrée à une description détaillée de l'expérience, des performances attendues et du type de données que HARP doit fournir. Nous expliquons aussi en quoi l'étude de la production de K^0_S est importante. La troisième partie décrit avec précision la chambre à projection temporelle (TPC), un détecteur à la construction duquel j'ai participé activement. En quatrième partie, le programme que j'ai développé pour calculer le vertex primaire est présenté ainsi que ses performances pour un échantillon de données simulées et de physique de HARP. Dans la dernière partie, les résultats préliminaires de recherche de masse invariante de K^0_S produits dans une cible de beryllium de 5% de longueur d'interaction et pour un faisceau de 12 GeV/c sont présentés. Au préalable, une étude des performances de la reconstruction a été effectuée sur un générateur produisant des pions et dont la cinématique peut être contrôlée. Ensuite la même étude a été poursuivie avec un générateur hadronique.

Parmi les différents modèles qui tentent d'expliquer notre univers à l'échelle microscopique, le Modèle Standard est le plus répandu d'entre tous. A l'aide de deux familles de particules élémentaires (les leptons et les quarks) et d'une famille de particules médiatrices des interactions, en inscrivant les équations du mouvement des particules dans le formalisme de la théorie des champs, il décrit de manière satisfaisante les phénomènes qui nous entourent.
Les découvertes récentes des expériences de physique des neutrinos comme SNO ou Super-Kamiokande ont soulevé à nouveau la question de l'hypothèse d'oscillation des neutrinos et de leurs masses, un phénomène que le Modèle Standard ne décrit pas.
Les rayons cosmiques qui bombardent la terre en permanence par interaction avec les composants gazeux de l'atmosphère, produisent des douches hadroniques parmi lesquelles une large fraction de kaons et de pions qui se désintégrent et donnent naissance à des neutrinos. Les taux de production de ces neutrinos atmosphériques ont été mesurés à travers la mesure des interactions par courants chargés et comparés aux taux prédits par les modèles qui décrivent les interactions atmophériques. Les mesures de taux sont accompagnées d'erreurs systématiques très larges dues au manque de connaissance sur le taux absolu de rayons cosmiques primaires et aux incertitudes de la modélisation des interactions hadroniques dans l'atmosphère. Néanmoins, il est possible de mesurer le double rapport RR entre données (DATA) et simulation (MC), du

flux de neutrinos électroniques sur le flux de neutrinos muoniques :

$$RR = \frac{(\nu_\mu/\nu_e)_{DATA}}{(\nu_\mu/\nu_e)_{MC}}$$

Si la simulation reproduit bien les phénomènes rencontrés dans la nature, on devrait obtenir une valeur du double rapport égale à un. Les expériences IMB et Super-Kamiokande ont mesuré un rapport inférieur à un, confirmé par l'expérience Soudan-2. Cependant le calcul du double rapport ne permet pas de conclure à une surabondance de neutrinos de type ν_e ou à un déficit de neutrino de type ν_μ. Par contre, pour les neutrinos de grande énergie, la direction de production du lepton chargé est fortement corrélée à celle du neutrino agissant. Cela permet donc une mesure directe de la distance de vol entre la source et le détecteur, et, en cas d'oscillation, la distribution du double rapport en fonction de l'angle de zénith est dépendante du rapport de la distance parcourue L sur l'énergie du neutrino E. Kamiokande a été la première expérience à publier la distribution du double rapport en fonction de l'angle de zénith montrant un désaccord avec la distribution attendue en l'absence d'oscillation.
Super-Kamiokande, en séparant les événements avec muons voyageant dans la direction montante (U) par rapport à l'axe vertical du détecteur, des événements avec muons voyageant dans la direction descendante (D), a publié une mesure du double rapport AA :

$$AA = \frac{(U/D)_{DATA}}{(U/D)_{MC}}$$

Les résultats montrent un déficit en ν_μ, interprété comme une oscillation des neutrinos de saveur muonique en une autre saveur. L'expérience MACRO a aussi publié un double rapport en fonction de l'angle de zénith favorisant l'hypothèse d'oscillation des neutrinos atmosphériques mais avec une structure qui n'est pas totalement comprise.
Le soleil produit continuellement des neutrinos de type électronique, à travers plusieurs cycles de transformation de l'hydrogène et de l'hélium, décrit parfaitement par le Modèle Solaire Standard (SSM). Les neutrinos solaires ont été détectés expérimentalement avec des flux et des énergies qualitativement comparables à ce que prédit le SSM mais en désaccord sur le plan quantitatif.
Les expériences pionnières dans ce domaine à observer les neutrinos solaires furent des expériences de radiochimie telles que Homestake d'abord, GALLEX ou SAGE ensuite. Elles fonctionnent toutes sur le même principe mais avec une sensibilité différente aux réactions entrant dans le cycle solaire, permettant d'offrir des résultats complémentaires. La méthode expérimentale consiste à mesurer le taux de production d'un isotope radioactif, à partir de la capture d'un neutrino sur un autre isotope et après exposition de la cible aux neutrinos solaires durant plusieurs mois. Homestake (sensible aux neutrinos émis dans le cycle ^8B) a observé seulement un tiers du flux de neutrinos prédits. GALLEX et SAGE (qui détectent les neutrinos provenant du cycle *pp*) ont aussi observé un déficit important ($\sim 50\%$).
Les expériences Kamiokande et Super-Kamiokande (sensibles aussi aux neutrinos ^8B) ont confirmé le déficit observé par Homestake avec une valeur du flux égale à la moitié du flux attendu.
Longtemps on s'est posé la question de savoir si le modèle solaire était correct ou non jusqu'à ce que SNO publie aussi des résultats favorisant les oscillations de neutrinos indépendamment du modèle solaire. Cette expérience mesure le taux d'événements d'interaction de neutrinos par courants neutres (impliquant les trois saveurs de neutrinos) sur le taux d'événements de neutrinos par courants chargés (impliquant seulement les neutrinos de type électroniques). Le flux de total de neutrinos et le flux de neutrinos électroniques sont donc mesurés indépendamment. Aujourd'hui le déficit observé est interprété par une disparition des neutrinos solaires dû à leurs oscillations en une autre saveur.
L'expérience LSND a publié des résultats favorisant l'oscillation d'anti-neutrinos muonique en anti-neutrinos

électroniques. L'expérience KARMEN, qui explore le même domaine de différence de masse et d'angle de mélange des neutrinos n'a pas confirmé les résultats de LSND. Ces derniers sont inconsistants avec les résultats obtenus pour les neutrinos atmosphériques et solaires: avec trois neutrinos actifs on ne peut avoir que deux différences de masses carrées indépendantes. Quelques solutions ont été proposées comme l'introduction d'un neutrino stérile (non sensible aux interactions faibles) dans le Modèle Standard ou la violation de l'invariance CPT (charge-parité-inversion du temps). L'expérience MiniBooNE devrait, avec une statistique bien plus grande, permettre d'offrir des résultats qui pourront être confrontés à ceux de LSND et aider à résoudre le puzzle des neutrinos.

La nécessité de mener une expérience de production hadronique a resurgit récemment pour trois raisons principales. Premièrement, il est important de connaître les angles et les énergies de production des pions avec précision, afin de décider du meilleur concept pour les usines à neutrinos. Deuxièmement, les calculs de flux de neutrinos atmosphériques doivent être améliorés et les erreurs réduites pour pouvoir interpréter les résultats obtenus par les expériences de neutrinos atmosphériques de manière satisfaisante. Troisièmement, l'étude de l'interaction des hadrons sur différents types de matériaux et pour différentes énergies de faisceau fournit des renseignements utiles pour la simulation ou l'analyse d'expériences en physique des particules à venir ou en cours. Les études menées précédemment n'ont pu explorer qu'une petite fraction de l'espace de phase et ce avec une précision insuffisante. Enfin pour mesurer avec précision les paramètres d'oscillation des neutrinos, il faut construire des machines capables de fournir des faisceaux de neutrinos de haute intensité, avec un spectre et une composition parfaitement connus. En attendant la construction de ce type de machine appelée usine à neutrinos, il faut essayer de comprendre et optimiser les faisceaux de neutrinos dits conventionnels et qui sont largement utilisés dans les expériences d'oscillations de neutrinos. Ces faisceaux utilisent les neutrinos produits lors de la désintégration de particules comme les pions et les kaons chargés, eux mêmes provenant de l'interaction d'un faisceau de protons sur une cible. Ce type de faisceau contient donc différentes saveurs de neutrinos avec des spectres différents. Dans les faisceaux de ν_μ il est donc important de connaître précisément le bruit de fond de production de neutrinos électroniques provenant de mésons chargés ou neutres comme dans les canaux K^+_{e3} ou K^0_{e3}. L'étude de la production de kaons neutres K^0_S à partir de l'interaction d'un faisceau de protons sur une cible fixe peut nous renseigner sur la production des kaons chargés et neutres en général puisque que leur taux de production est directement lié à la composition de la mer en quarks étranges. De plus la recherche de K^0_S dans les données de HARP est un moyen de valider la reconstruction.

HARP a été conçue pour mesurer la production de hadrons provenant de l'interaction d'un faisceau de protons et de pions de quantité de mouvement comprise entre 1.5 GeV et 15 GeV sur différents types de cibles solides et liquides (cryogéniques). L'appareillage expérimental comprend trois parties, le faisceau avec des détecteurs servant à identifier les particules qui arrivent sur la cible, un spectromètre à grand angle d'ouverture qui contient la cible et un spectromètre à petit angle (cf. Figure 1). L'identification des particules du faisceau est fournie par deux détecteurs čerenkov à gaz (BC A et BC B) et une paire de compteurs de temps de vol (TOF A et TOF B). Quatre chambres à fils (MWPCs) fonctionnant en mode proportionnel mesurent la position et la direction des particules du faisceau avant la cible. Divers scintillateurs servent dans le déclenchement du système de prise de données en sélectionnant les particules du faisceau une bien orientées par rapport à la cible.

Le spectromètre à grand angle est inséré dans un aimant solénoidal. Il contient la cible et plusieurs couches de cylindriques de détecteurs installés à différents rayons. Au rayon minimal, la cible est entourée par six couches de fibres scintillantes servant de système de déclenchement pour l'interaction. La majorité de l'espace de l'aimant est occupé par la TPC qui fait 1.54 m de longueur pour un diamètre de 0.82 m. Cette dernière sert à la fois à mesurer la quantité de mouvement des particules chargées qui traversent le détecteur

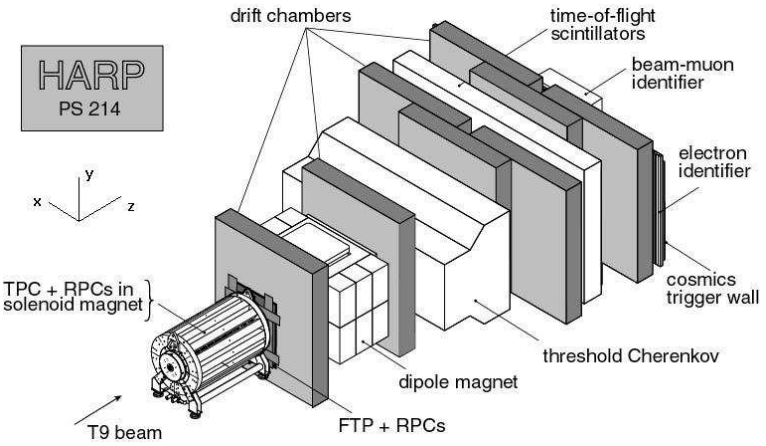

Figure 1: Schéma d'ensemble des détecteurs de HARP

dans tout l'angle solide mais aussi à identifier les pions, kaons et protons de petite quantité de mouvement. L'identification des particules est complétée grâce à un ensemble de chambres résistives qui entourent la TPC.

Les particules à petits angles et de grande quantité de mouvement sont mesurées par le spectromètre situé en aval. Un plan double de compteurs scintillateurs placé en aval de l'aimant solénoidal fournit le système de déclenchement vers l'avant. Le spectromètre aval comprend un groupe de quatre chambres à dérive (NDCs) placé avant un aimant dipolaire et un autre groupe de quatre chambres à dérive placé juste après. D'autres groupes de chambres à dérive placés en aval servent à suivre la trajectoire des particules qui traversent les détecteurs chargés de leur identification. La séparation des protons, pions et kaons voyageant vers l'avant est fournie par un détecteur čerenkov à seuil. Un plan de mesure du temps de vol permet de séparer les pions et les protons de petite quantité de mouvement. L'identification des photons et des électrons se fait grâce à un groupe de chambres à dérive jouant le rôle de pré'echantillonneur, suivi par un calorimètre électromagnétique. Un détecteur à muons (formé d'un bloc de fer) termine le spectromètre aval.

Au total près de 420 millions d'événements ont été enregistrés pour différentes énergies de faisceau et types de matériaux pour la cible. Les événements enregistrés pour les différents types de cible sont répertoriés dans le tableau 1.

La TPC de HARP enregistre les traces des particules secondaires émises à des angles compris entre 20° et 160°. Le détecteur comprend une cage de champ électrique cylindrique externe et une cage de champ interne; le disque aval est une membrane à haute tension et le disque amont le plan de lecture. Un schéma du détecteur avec quelques nombres utiles est montré en figure 2. Le volume actif de la TPC est un cylindre de rayon 41.6 cm et de longueur 154.1 cm définie par la cage de champ externe. La cible est installée dans un insert qui se trouve à l'intérieur de la cage de champ interne. Cette dernière à un rayon de 5.1 cm. Les particules secondaires chargées, produites dans les collisions faisceau sur la cible ionisent le mélange de gaz argon (91%)-méthane (9%) et produisent des électrons qui vont dériver en direction du plan de lecture à une vitesse de l'ordre de 5.17 cm/μs. Le plan de lecture est constitué de six secteurs composés de 662 pads de lecture chacun; les pads sont disposés en cercles concentriques á différents rayons. La dimension d'un pad de lecture est de 6.5 $\times$ 15 mm. Le signal de chaque pad est ensuite amplifié puis envoyé dans un convertisseur analogique-digital. A la digitisation, une coupure sur le bruit de fond de l'électronique (soustraction du 'piedestal') est appliquée, ainsi qu'une coupure à dix coups au dessus du piedestal avant d'envoyer les signaux de chaque pad au système de compression des données.

Plusieurs systèmes de calibration servent à vérifier la bonne marche du détecteur. En introduisant mo-

Cibles	Charge et quantité de mouv. du faisceau (GeV/c)	Longueur ou λ_{int}	Evénements (10^6)
Be	$\pm$3, $\pm$5, $\pm$8, $\pm$12, $\pm$15	2%, 5%, 100%	37.4
C	$\pm$3, $\pm$5, $\pm$8, $\pm$12, $\pm$15	2%, 5%, 100%	30.7
Al	$\pm$3, $\pm$5, $\pm$8, $\pm$12, $\pm$15	2%, 5%, 100%	34.5
Cu	$\pm$3, $\pm$5, $\pm$8, $\pm$12, $\pm$15	2%, 5%, 100%	36.6
Sn	$\pm$3, $\pm$5, $\pm$8, $\pm$12, $\pm$15	2%, 5%	23.7
Ta	$\pm$3, $\pm$5, $\pm$8, $\pm$12, $\pm$15	2%, 5%, 100%	38.2
Pb	$\pm$3, $\pm$5, $\pm$8, $\pm$12, $\pm$15	2%, 5%, 100%	44.9
K2K	+12.9	5%, 50%, 100%	15.3
MiniBooNE	+8.9	5%, 50%,100%	22.6
N	$\pm$3, $\pm$5, $\pm$8, $\pm$12, $\pm$15	6 cm	13.0
O	$\pm$3, $\pm$5, $\pm$8, $\pm$12, $\pm$15	6 cm	15.5
H	$\pm$3, $\pm$5, $\pm$8, $\pm$12, $\pm$15	6, 18 cm	32.0
D	$\pm$3, $\pm$5, $\pm$8, $\pm$12, $\pm$15	6 cm	21.0
Eau	+1.5	10%, 100%	6.4
Pb, Ta, Cu	+1.5	5%	3.2

Table 1: Données de HARP

mentanément un gaz radioactif (de l'isotope ^{83m}Kr) mélangé au gaz de la TPC, on reconstruit le signal provenant de la conversion des photons au pic d'énergie de 41 keV : l'idée était de pouvoir mesurer la réponse relative de chaque pad. Malheureusement, la présence d'une diaphonie inattendue dans l'électronique du plan de lecture de la TPC, empêche de mesurer la linéarité de la réponse de chaque pad. Une calibration à l'aide d'une source radioactive (Fe) a été menée en fin de prise de données, afin de mesurer la réponse des pads et leur linéarité.

Afin de mesurer la vitesse de dérive des électrons et de pouvoir enregistrer tout changement dû à des différences de températures ou de pression, un système de calibration laser à été installé sur la face opposée au plan de lecture de la TPC. Une série de 192 fibres placées selon un arrangement circulaire à différents rayons transmet la lumière émise par un laser (KrF) à une longueur d'onde de 248 nm. Les photons vont exciter la surface d'aluminium déposée sur l'extrémité des fibres et permettre l'éjection d'électrons à une position bien précise dans l'espace et dans le temps. En mesurant le temps entre le moment où le laser a illuminé le plan où sont fixées les fibres et l'arrivée des électrons sur le plan de lecture il est possible de mesurer la vitesse de dérive. Ces données dévénements laser, en mesurant la position du signal reconstruit par rapport à la position des fibres permettent aussi de mesurer de possibles effets de champ $\vec{E} \times \vec{B}$ pouvant être dus à un mauvais alignement du champ électrique.

Le phénomène de diaphonie entre les pads est dû à la conception du plan de lecture qui est constitué d'un circuit imprimé à six couches dont la première contient le plan de pads et la dernière l'électronique de préamplification. Si une ligne de transport du signal à la sortie du préamplificateur passe trop près de l'entrée d'un autre préamplificateur elle va créer un bruit parasite dégradant le signal de ce préamplificateur. Une campagne de mesures systématiques, pad à pad, a été menée à la fin de la prise de données afin de pouvoir construire un modèle simulant cet effet de diaphonie et de construire les matrices de déconvolution du signal de diaphonie dans les données de physique.

Les étapes de la reconstruction du signal provenant de la TPC sont les suivantes: le temps d'arrivée du signal mesuré par l'électronique de la TPC est d'abord corrigé de la longueur des câbles, des délais intro-

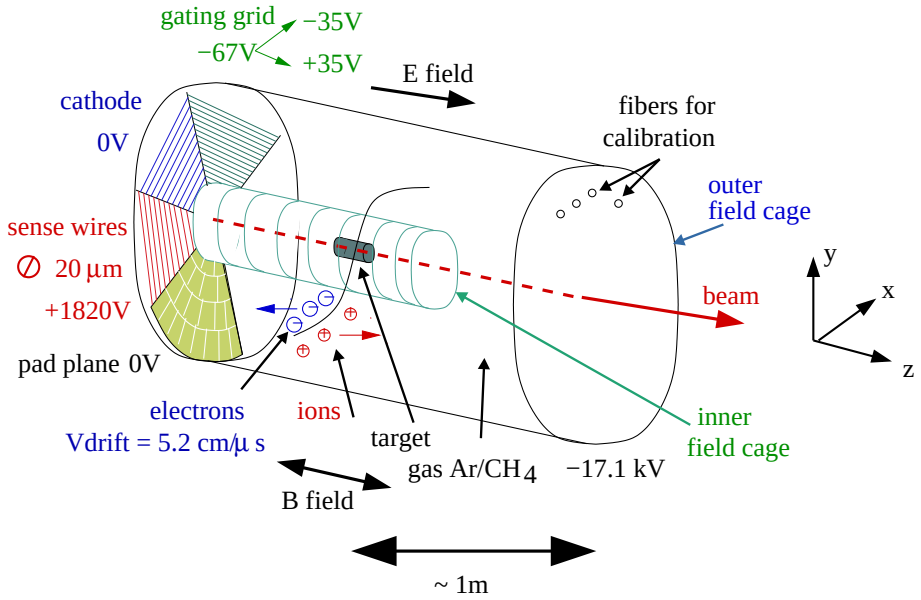

Figure 2: Représentation schématique de la TPC

duits par les divers modules électroniques et rapporté à une valeur proche du temps zéro du système de déclenchement et donc du temps réel de passage de la particule du faisceau. Au début de chaque run trois événements de piedestaux ont été enregistrés. La moyenne sur ces trois événements et la déviation standard sont calculées pour chaque pad. Ensuite pour les données physiques de ce même run, à chaque pad on soustrait la moyenne correspondante coupant ainsi le signal de bruit de fond de l'électronique. La déviation standard sert à repérer les pads qui se comportent de manière marginale du fait d'une voie d'électronique endommagée ou bruyante. Certains canaux ont été masqués sur la base de ces données (ils ne représentent pas plus de 1% du nombre total de canaux). Après soustraction du piedestal un seuil fixe de 10 coups d' ADC est encore soustrait aux données avant que celles-ci ne soient envoyées au code de reconstruction. L'électronique de la TPC enregistre les signaux à une fréquence de 10 MHz. Des groupes de signaux voisin en temps pour chaque pad, puis dans une même région (pads voisins) sont définis et leur barycentre calculé afin de construire des points dans l'espace et dans le temps. Ensuite un programme essaie de relier entre eux les points pouvant provenir d'une même trace. Enfin un programme calcule les paramètres de l'hélice passant par ces points. En tout dernier lieu, un programme recalcule les paramètres de l'hélice en tenant compte des effets de diffusion à l'aide d'un outil Kalman.

A la fin de la reconstruction des données de HARP, un programme de calcul de vertex doit fournir la position du point d'interaction ainsi qu'une estimation de la quantité de mouvement des particules à ce point. Il a été décidé de calculer ce vertex à l'aide d'un outil Kalman qui a l'avantage d'être rapide et de prendre en compte les phénomènes de diffusion. Pour un système de n traces, une première estimation de la position du vertex et de la quantité de mouvement de chaque trace peut-être fournie en extrapolant les traces à une surface de référence que nous avons définie au préalable. Le vecteur des paramètres position-quantité de mouvement de la particule à la surface de référence est une fonction de la véritable position du vertex et de la quantité de mouvement de cette particule en ce point là, plus de l'erreur sur la mesure à la surface de référence. Si on linéarise cette fonction par un développement de Taylor autour d'un point d'expansion, les équations du système permettant d'obtenir la position du vertex et la quantité de mouvement de la partic-

ule en ce point, se présentent sous forme matricielle pour le système de n traces. Une linéarisation par la méthode des moindres-carrés permet d'obtenir le résultat attendu. La méthode Kalman utilise le fait que la matrice du système est diagonale par bloc et l'on n'effectue que les opérations nécessaires à la connaissance des quantités position-quantité de mouvement. Les équations peuvent être réécrites de manière itérative où, à chaque étape, une nouvelle trace est ajoutée. Une première estimation de la position du vertex et de la quantité de mouvement de chaque trace au vertex est faite en partant d'un système à une trace pour arriver à un système à n traces et en calculant à chaque étape la position du vertex, la quantité de mouvement de la trace au vertex et la matrice de covariance des erreurs sur la position et la quantité de mouvement. Ensuite en partant du système à n traces avec les mesures obtenues, la position et la quantité de mouvement sont recalculées à chaque étape afin d'introduire la connaissance des traces ajoutées au système a posteriori et de redéfinir un système final qui ne doit plus dépendre de l'ordre dans lequel les traces ont été ajoutées. Le calcul du χ^2 pour le fit et à chaque étape, doit servir dans un second temps à rejeter les traces qui ne font pas partie du vertex et à recalculer le vertex pour un sous-ensemble du système.
Les performances du programme de calcul de vertex ont été évaluées à partir de données simulées et sur des événements de données de physique de HARP. Nous sommes partis d'un système d'équations mathématiques simple, en définissant un modèle linéaire pour la propagation des traces entre le point de vertex et le point mesuré à la surface de référence. A l'aide d'un outil très simple simulant des points dans l'espace nous avons pu évaluer les performances de l'algorithme pour un système de deux et quatre traces. En comparant les données simulées avec les résultats fournis pour le vertex nous avons pu évaluer les défauts de cet outil comme la sensibilité aux paramètres d'entrée du système tels que le point d'expansion. Dans un second temps, cet outil a été testé dans l'environnement de HARP avec des traces reconstruites dans la TPC uniquement, dans les NDCs uniquement, et avec ou sans le champ de l'aimant solénoidal pour les traces reconstruites dans les NDCs. Cela nous a permis de noter quelques défauts de la reconstruction pour la version de code que nous avons utilisée et de confirmer la tendance déjà observée avec le petit outil de simulation. Les progrès en cours en ce qui concerne la reconstruction devraient permettre de mener une étude systématique des paramètres d'entrée et d'y rendre insensible le programme de vertex. La distribution de la position du vertex en z pour une cible de beryllium mince (longueur 2.03 cm) et épaisse (longueur 40.6 cm) est montrée dans la figure 3 pour les données de physiques prises dans HARP.
Une étude préliminaire de recherche de K^0_S à partir de données simulées a été menée afin de déterminer la capacité de reconstruction de la masse invariante du K^0_S et d'estimer le bruit de fond combinatoire provenant des traces de l'interaction.
La masse invariante est reconstruite à partir de toutes les combinaisons possibles de paires de pions de charges opposées reconstruites dans les NDCs.
A l'aide d'un générateur pouvant produire des pions à des angles et des quantités de mouvement déterminés nous avons mesuré une résolution sur la masse invariante de l'ordre de 20-30 MeV/c^2 comme le montre la figure 4 pour des paires de pions envoyés à 150 mrad par rapport à l'axe z et provenant d'un K^0_S de 3 GeV/c. La résolution sur la masse invariante peut être considérée suffisante en l'absence de bruit de fond.
Dans un second temps nous avons mené une étude des performances de la reconstruction de la masse invariante à l'aide d'un générateur hadronique produisant des K^0_S. Certains problèmes provenant du générateur ont été identifiés comme pouvant mener à une mauvaise estimation du bruit de fond et une étude détaillée du générateur sera nécessaire afin de comprendre certaines de ses particularités comme un comportement non exponentiel dans la région 475-500 MeV/c^2 (cf. figure 5).

A partir d'un échantillon de données simulées de près d'un million d'événements pour un faisceau de 12 GeV/c sur une cible de beryllium de 5% de longueur d'interaction et de la même quantité sélectionnée parmi les données de physique de HARP, nous avons calculé le nombre d'événements de K^0_S de la manière suivante. On soustrait aux événements situés dans la région de masse entre 460 et 540 MeV/c^2 le nombre

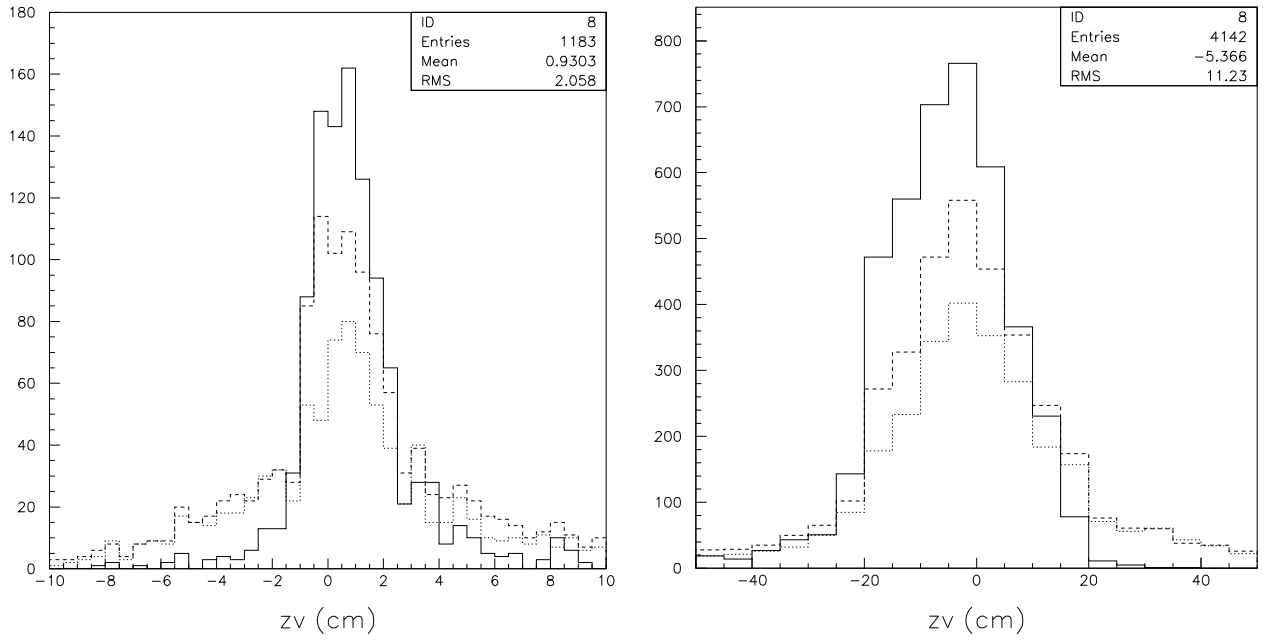

Figure 3: Position du vertex (cm) en z pour la cible Be mince (à gauche) et épaisse (à droite) et un faisceau de 12 GeV/c, trait plein TPC, tirets MWPCs, pointillés NDCs

d'événements bruit de fond obtenus à partir d'un fit exponentiel où la région 400-600 MeV/c^2 a été exclue. Ce nombre est renormalisé par le nombre d'événements d'interaction et par l'efficacité de reconstruction du K^0_S comme suit :

$$N_{K^0_S} = \frac{1}{\varepsilon} \times \frac{N - f_{bkg}}{N_p^{inc}}$$

où ϵ est notre efficacité de reconstruction des K^0_S.
Elle vaut :

$$\varepsilon = \frac{N^{rec}_{K^0_S}}{N^{tot}_{K^0_S}}$$

$N^{rec}_{K^0_S}$ est le nombre de K^0_S reconstruits dans cette région.
$N^{tot}_{K^0_S}$ le nombre total de K^0_S générés.
Elle a été estimée à 12.1% à partir de l'échantillon de données simulées.
N est le nombre d'événements sélectionnés dans cette région.
f_{bkg} est le nombre d'événements bruit de fond dans la région sélectionnée. Il est obtenu à partir du fit exponentiel.
N_p^{inc} est le nombre de protons incidents sur la cible. Il peut être estimé à partir du nombre d'événements reconstruits.
Le nombre d'événements de K^0_S dans l'echantillon de données sur la cible Be 5% est de :

$$N_{K^0_S} = (-5.82 \pm 0.52) \cdot 10^{-4}$$

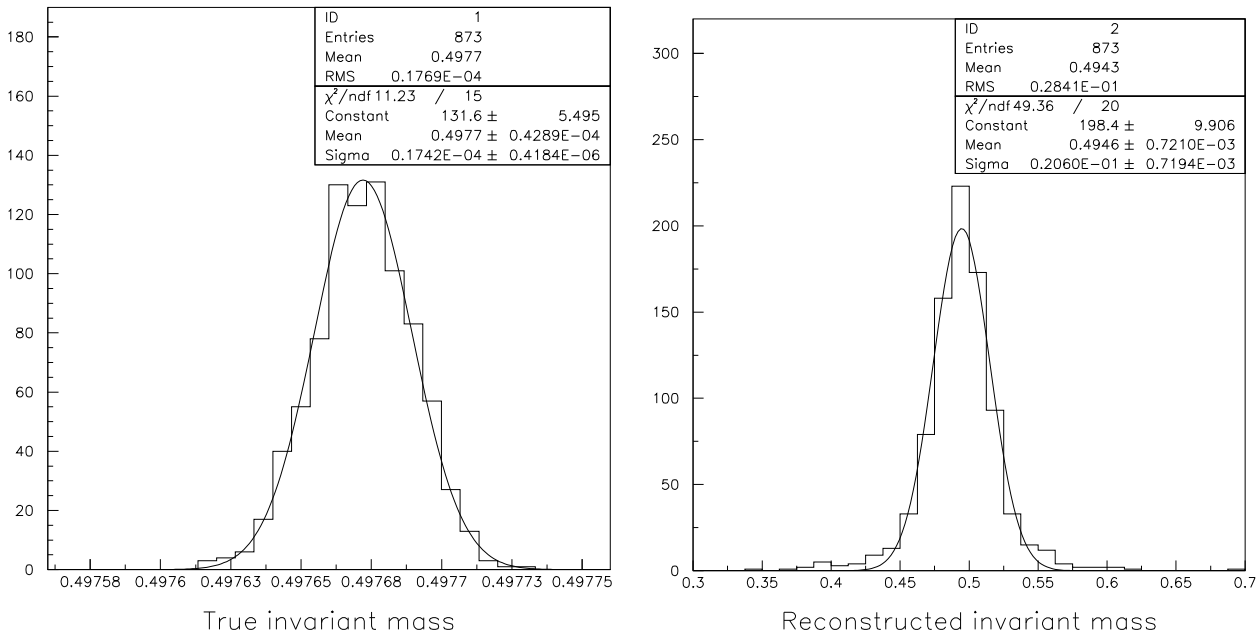

Figure 4: Masse invariante (GeV/c^2) vraie (à gauche) et reconstruite (à droite) pour des paires de pions de charge opposée dans les NDCs

Dans l'échantillon Monte Carlo il s'élève à :

$$N_{K^0_S} = (-3.69 \pm 1.00) \cdot 10^{-3}$$

Ces deux nombres sont compatibles entre eux et compatibles avec zéro.

En conclusion, il a été démontré que l'état de la reconstruction ne permet pas pour le moment d'obtenir un signal de désintégration de K^0_S.
Cependant, en parallèle avec les efforts continus menés pour améliorer la reconstruction, une étude détaillée des générateurs hadroniques mis à disposition et une éventuelle correction de certains de leur problèmes permettrait une meilleure estimation du bruit de fond combinatoire des pions et de, sans doute, augmenter la résolution afin d'obtenir, avec de futures versions de la reconstruction, un signal de K^0_S.

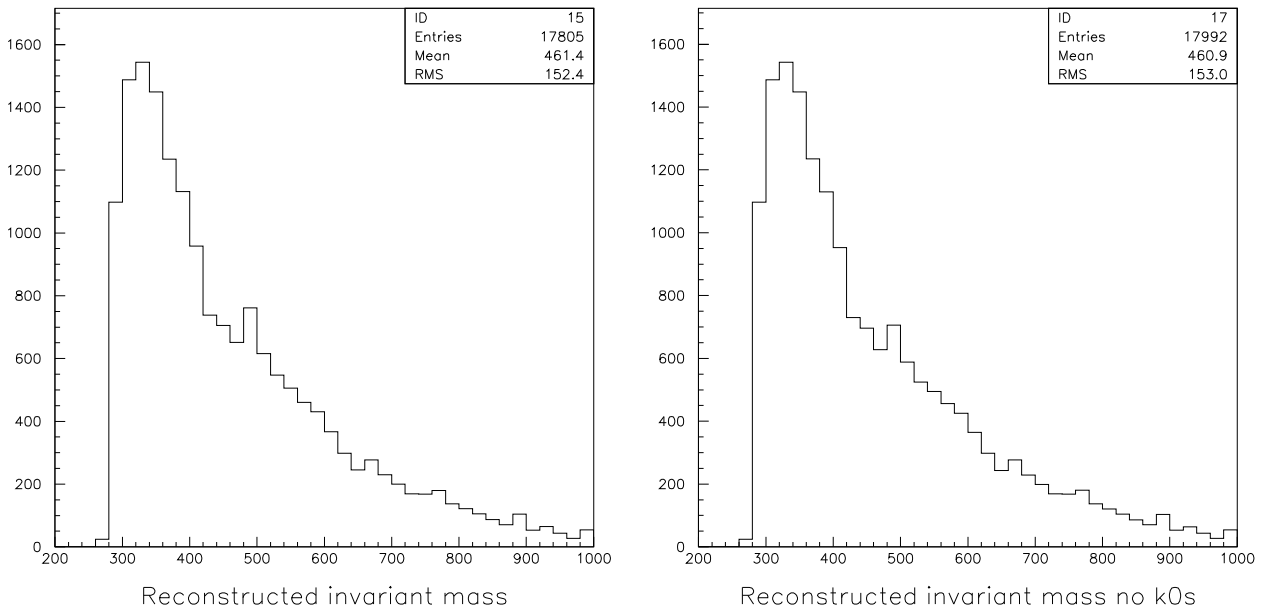

Figure 5: Masse invariante (MeV/c^2) pour toutes les paires de pions de charge opposée (à gauche) et pour celles qui ne proviennent pas d'un parent K_S^0 (à droite), générateur Monte Carlo

Contents

List of Figures

List of Tables

Chapter 1

Introduction

The hadron production experiment HARP (PS214) carried out a programme of measurements of secondary hadrons at the European Organization for Nuclear Research (CERN) proton synchrotron (PS) during the years 2001 and 2002. It serves several purposes. On one side there is a need to acquire knowledge of pion yields for an optimal design of the proposed neutrino factories and superbeams. On the other one, we have to improve substantially the calculation of the atmospheric neutrino flux, used by past and forthcoming experiments designed to measure neutrino oscillations. HARP data will also provide a general input for simulation of particles traversing matter, as well as neutrino beam predictions for the K2K and MiniBooNE experiments.
The subject of this thesis is to provide strange particle production, K^0_S, measurements, from HARP data. This study is of interest because, for neutrino beams, the charged kaon contamination induces an electron-neutrino type background in the muon-neutrino beam. The knowledge of such a background, in the HARP momentum range, and for different target materials, is essential in order to optimize the parent proton beam momentum, the target material as well as the focusing system.
The written report is divided in five parts. In the first part we describe the physics motivation through a review of the Standard Model theory and its limits. The second part is devoted to a detailed description of performance requirements for the HARP experiment and the kind of data HARP should provide. We also explain why K^0_S study is of interest. The third part will be devoted to a more detailed description of the HARP time projection chamber, a detector which construction I was deeply involved in. The fourth part contains the description of the software that was written to find the primary vertex and that I have developed and tested against simulated and physics data. In the last part we finally give preliminary results on the invariant mass search for the K^0_S produced in the target.

Part I

Neutrino physics

Chapter 2

The Standard Model

At the microscopic level, our universe is beautifully described by the Standard Model. With two types of elementary particles (the leptons and the quarks), one type of particles mediating the interactions, and quantum field theory formalism, it describes in an extremely satisfactory way most of the phenomena of particle physics. In the Standard Model, neutrinos are massless.
Recent neutrino results in particular published by the Sudbury neutrino observatory (SNO) [2] and Super-Kamiokande [3] experiments showed evidence for neutrino oscillations and neutrino masses, not described by the Standard Model. We give here a brief introduction to the Standard Model and the description of the neutrino in its framework.

2.1 The particles and their interactions

In the Standard Model, all particles that undergo interactions are either half-integer spin (called fermions) or integer spin (called bosons) particles. The particles can be classified as follows:

- The leptons (fermions), comprising the electron e^-, the muon μ^-, the tau τ^- and three types of neutrinos ν_e, ν_μ and ν_τ. The six associated anti-particles are the positron e^+, the muon μ^+ and the tau τ^+ with three anti-neutrinos $\overline{\nu}_e$, $\overline{\nu}_\mu$ and $\overline{\nu}_\tau$.

- The hadrons, containing particles made of fundamental constituents called quarks. The quarks are present in six different flavours, ordered in three doublets, the u (up) and d (down), the c (charm) and s (strange), and the t (top) and b (bottom or beauty). Six anti-quarks are complementing the list of hadron constituents. The hadrons themselves are ordered in two subgroups: the meson group (boson particles), made of a quark-anti-quark doublet, and the baryon group (fermion particles), made of a quark triplet.

- The gauge boson family, with the well-known photon γ acting as intermediate vector of the electromagnetic interaction, three vector bosons of the weak interaction called the Z^0, the W^+ and the W^- and finally the gluon which is the mediator of the strong interaction.

Neutral leptons are only sensitive to the weak interaction while charged leptons couple to the weak and the electromagnetic interaction. The hadrons participate in the strong interaction, the electromagnetic interaction for the charged one and can (for some of them) decay via the weak interaction. The elementary particles are summarized in Table 2.1.
The description of the phenomena is made in the quantum field theory formalism, a re-normalizable theory

Leptons	e^-, μ^-, τ^- ν_e, ν_μ, ν_τ
Quarks	(u d) (c s) (t b)
Gauge Bosons	γ, Z^0, $W^\pm$, g

Table 2.1: The elementary particles family

based on local gauge invariance principles and using special unitary transformation groups [1] to represent the different interactions.
The theory of electromagnetic interaction, extended to quantum electro-dynamics (QED), an abelian gauge theory using the U(1) transformation group, has been incorporated to the weak interaction theory, a non-abelian gauge theory using the SU(2) transformation group, to form a unique electroweak interaction theory represented by the U(1)×SU(2) group product. The strong interaction theory is described by quantum chromodynamics (QCD), a non-abelian gauge theory using the SU(3) transformation group.
Leptons and hadrons interact by a gauge boson exchange. Since the coupling constant (which represents the strength of the interaction) due to the gravitation is very small, compared to the QED or QCD coupling constants, the graviton is not taken into account in the description of the interactions.
For the electroweak interaction, to keep the theory locally invariant, particles should be massless and in particular the intermediate gauge bosons $W^\pm$ and Z^0. By means of a spontaneous symmetry breaking mechanism (called Higgs mechanism), gauge bosons and elementary fermions get a mass. This mechanism is giving also birth to a new intermediate gauge boson called the Higgs boson. Distinction between mass eigenstates and weak eigenstates becomes possible then. If the particles are not mass-degenerated, we can assign a different base to the interaction and to the mass. This is what we call mixing. It is determined by the Cabibbo-Kobayashi-Maskawa (CKM) matrix in the quark sector. For the leptonic sector the analogue to the CKM matrix is called the Maki-Nakagawa-Sakata-Pontecorvo (MNSP) matrix. After symmetry breaking the neutrinos remain massless and the MNSP matrix plays no role since mass eigenstates are degenerate.

2.2 Neutrinos in the Standard Model

For massless neutrinos the solution of the Dirac equations (Weyl spinors) is giving two types of two-component states decoupled from each other, which are:

- a left-handed neutrino (ν_L) and a right-handed anti-neutrino ($\overline{\nu}_R$)
- a right-handed neutrino (ν_R) and a left-handed anti-neutrino ($\overline{\nu}_L$)

The weak interactions of the type V-A couple only to the left-handed neutrino and the right-handed anti-neutrino. So, these are the only one we can detect. To encounter both helicity states we have to go beyond the V-A theory or assume that the neutrinos have non-vanishing rest mass.

[1] U(n) being the unitary group of matrix M with U(n) = {M ∈ Mat $_{n\times n}(\mathbb{C})$ | $\overline{M}^T M = I_n$} and SU(n) the special unitary group SU(n) = {M ∈ Mat $_{n\times n}(\mathbb{C})$ | $\overline{M}^T M = I_n$, det(M)=1}

Chapter 3

Neutrino oscillations

In the past sevent years, results coming from experiments probing the neutrino sector have shown striking evidence for neutrino flavour oscillation. After a short definition of the neutrino mixing parameters and through a review of the so-called atmospheric neutrino problem, the solar neutrino problem and the unconfirmed liquid scintillator neutrino detector (LSND) results we will give the status of knowledge concerning neutrino oscillations and try to give hints about missing items in neutrino physics that would help to complete the neutrino puzzle.

3.1 Neutrino masses and neutrino mixing

If neutrinos are massive, as we have seen in Section 2.1 for the quark sector, there are two bases (see Figure 3.1) in which they can be represented, the flavour eigenstates in which neutrinos are produced by weak processes (ν_e, ν_μ, ν_τ,...) and the mass eigenstates (ν_1,ν_2, ν_3,...). Each flavour eigenstate can be written as

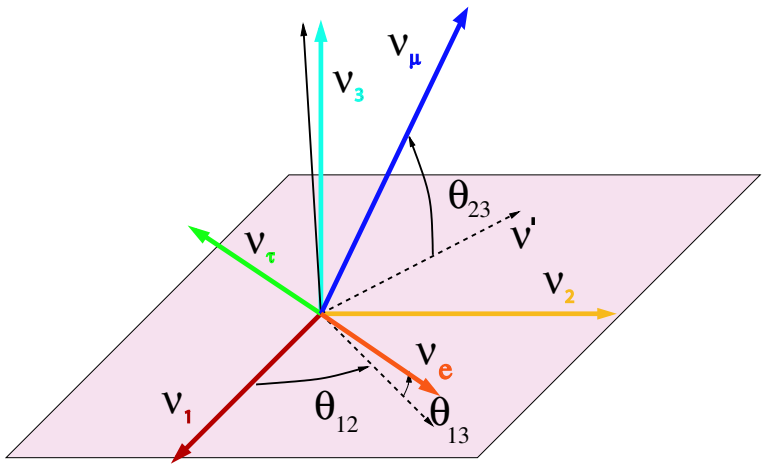

Figure 3.1: Mixing angles and relations between the two bases of the mass and flavour eigenstates

a linear combination of mass eigenstates:

$$\mid \nu_\alpha \rangle = \sum_{i=1}^{n} U^*_{\alpha i} \mid \nu_i \rangle$$

with n being the number of light neutrino species and $U^*_{\alpha i}$ the corresponding element of the MNSP matrix. Assuming three generations of neutrinos (as it was measured precisely at LEP to be 2.984 $\pm$0.008) the MNSP matrix can be parametrised as follows:

$$U = \begin{pmatrix} c_{12} \cdot c_{13} & s_{12} \cdot c_{13} & s_{13} \cdot e^{-i\delta} \\ -s_{12} \cdot c_{23} - c_{12} \cdot s_{23} \cdot s_{13} \cdot e^{i\delta} & c_{12} \cdot c_{23} - s_{12} \cdot s_{23} \cdot s_{13} \cdot e^{i\delta} & s_{23} \cdot c_{13} \\ s_{12} \cdot s_{23} - c_{12} \cdot c_{23} \cdot s_{13} \cdot e^{i\delta} & -c_{12} \cdot s_{23} - s_{12} \cdot c_{23} \cdot s_{13} \cdot e^{i\delta} & c_{23} \cdot c_{13} \end{pmatrix}$$

where $c_{ij} = \cos(\theta_{ij})$ and $s_{ij} = \sin(\theta_{ij})$, θ_{ij} being the mixing angle between the neutrino mass eigenstates i and j. δ is the CP violation[1] phase term.
Lets consider the simple case of oscillation in a vacuum to identify the relevant numbers for neutrino experiments. For a neutrino created via the weak interaction, its weak eigenstate $\mid \nu_\alpha \rangle$ is a superposition of mass eigenstates. It will evolve over time according to Schrödinger equations so that once it has traveled a distance L its state vector will be:

$$\mid \nu_\alpha(L) \rangle = \sum_{i=1}^{n} U^*_{\alpha i} \cdot e^{(\frac{-i \cdot m_i^2 \cdot L}{2 \cdot E})} \mid \nu_i(0) \rangle = \sum_{\alpha} \sum_{i} U^*_{\alpha i} e^{(\frac{-i \cdot m_i^2 \cdot L}{2 \cdot E})} U_{\beta i} \mid \nu_\beta(0) \rangle$$

assuming that the mass of the neutrino is small with respect to its momentum.
The probability that after a distance L the eigenstate α has evolved to a state β can be calculated as:

$$P(\nu_\alpha \to \nu_\beta) = \mid \langle \nu_\beta \mid \nu_\alpha \rangle \mid^2 = \delta_{\alpha\beta} - 4 \sum_{i>j} U^*_{\alpha i} \cdot U_{\beta i} \cdot U_{\alpha j} \cdot U^*_{\beta j} sin^2(\frac{\Delta m^2_{ij} \cdot L}{4 \cdot E})$$

with $\Delta m^2_{ij} = m(\nu_i)^2 - m(\nu_j)^2$ and E being the energy of the neutrino.
So, the sensitivity of experiments to neutrino oscillations is directly depending on the travel distance L, the neutrino energy E and the squared mass difference in the simplest case.
In the case of oscillation in matter, due to electron content of the matter, the transition probability for ν_e type neutrinos to other flavours is modified. This is known as the Mikheyev-Smirnov-Wolfenstein (MSW) effect and accounts for the enhanced oscillation for neutrinos coming from the core of the sun as well as a possible day-night variation of the solar neutrino rate due to the earth matter traversed during the night.

3.2 Atmospheric neutrinos

Primary cosmic rays (composed in majority of protons but also of a certain amount of heavier stable nuclei such as He, C or Fe) continuously bombard the earth's upper atmosphere and produce hadronic showers. Among them is large fraction of pions and kaons. Due to the low density of the atmosphere, most of the hadrons decay before interacting and a large fraction of the muons produced by the secondary particles decay as well before reaching the ground. As a result of these processes we observe at the earth surface a continuous flux of muons as well as neutrinos.

[1] violation of the symmetry conservation under charge (C) and parity (P) transformations

Experiments studying atmospheric neutrinos have up to now observed electrons and muons produced in charged-current interactions and compared their observed numbers with the expected rates.
The absolute estimate of the rates is not an easy task and still suffers from quite large systematic uncertainties of $\sim 20\%$. This is due to the poor knowledge of the primary cosmic ray flux and from uncertainties in the modelling of the hadronic interactions in the atmosphere.
Experiments generally measure the flux ratio between ν_μ and ν_e and results are given as double ratio:

$$RR = \frac{(\nu_\mu/\nu_e)_{DATA}}{(\nu_\mu/\nu_e)_{MC}}$$

If the simulation describes the data one would expect RR=1.
Observation of anomalous effects in RR ratio have been found in the IMB [4] experiment sub-GeV sample and in the Super-Kamiokande sub-GeV and multi-GeV samples [5]. The too low double ratio value has been confirmed by the Soudan-2 [6] results. A priori the double ratio does not give enough information to conclude if we have too many ν_e or a ν_μ deficit.
On the other hand, for high energy neutrinos ($E > 500$ MeV) the direction of the produced charged lepton is strongly correlated with that of the incoming neutrino. Therefore the zenith angle of the incoming neutrino is a direct measure of the flight path between the source and the detector and a zenith-angle dependent suppression which follows a L/E behaviour can be interpreted as a strong indication in favour of neutrino oscillation. The Kamiokande [7] experiment was the first to publish a zenith-angle distribution of RR in disagreement with the expected shape.
The high statistics provided by Super-Kamiokande allows for the selection of upward-going events U (-1 $< \cos\theta <$ 0.2) and downward-going events D (0.2 $< \cos\theta <$ 1). The atmospheric flux should be up-down symmetric if we neglect the geomagnetic effects. The up-down double ratio is given by:

$$AA = \frac{(U/D)_{DATA}}{(U/D)_{MC}}$$

Super-Kamiokande observed in the computation of the AA ratio, a deficit of ν_μ in the muon-like multi-GeV sample interpreted as a flavour oscillation from ν_μ to another species.
The MACRO [8] experiment also found results favouring neutrino oscillations but with a structure of the zenith-angle dependence distribution that could not be understood completely.
Results from Super-Kamiokande presented at the Neutrino 2004 conference [9] are giving for a three flavour analysis (best fit) a $\Delta m^2_{23} = 2.7 \cdot 10^{-3}$ eV^2, $\sin^2\theta_{23} = 0.5$ and $\sin^2\theta_{13} = 0.0$. These results have been confirmed by the K2K experiment.

3.3 Solar neutrino oscillation

The Standard Solar Model (SSM) describes in detail the different reaction chains involved in the production of stellar energy. For a low-mass star like the sun, the main chain is a hydrogen burning cycle called the pp chain and leading to neutrino production through six different reactions as follows. For the first part of the cycle we have:

$$\begin{array}{rcll} p + p & \rightarrow & D + e^+ + \nu_e & (99.6\%)\ \text{pp} \\ p + e^- + p & \rightarrow & D + \nu_e & (0.4\%)\ \text{pep} \\ p + D & \rightarrow & {}^3He + \gamma & \end{array}$$

In almost 85% of the cases, the cycle then proceeds through:

$${}^3He + {}^3He \rightarrow {}^4He + p + p$$

Very rarely (about $2\times10^{-5}\%$ of the cases), the so-called hep reaction occurs:

$$^3He + p \rightarrow {}^4He + e^+ + \nu_e$$

In the remaining 15% of the cases the following reactions take place most of the time (99.83%):

$$\begin{aligned} ^3He +^4 He &\rightarrow \gamma +^7 Be \\ ^7Be + e^- &\rightarrow {}^7Li + \nu_e \\ ^7Li + p &\rightarrow {}^4He +^4 He \end{aligned}$$

In the remaining 0.17%, the branch is:

$$\begin{aligned} ^7Be + p &\rightarrow {}^8B + \gamma \\ ^8B &\rightarrow {}^8B^* + e^+ + \nu_e \\ ^8B^* &\rightarrow {}^4He +^4 He \end{aligned}$$

Solar neutrinos have been detected experimentally with fluxes and energies that are qualitatively consistent with the SSM but quantitatively not agreement with it.
Radiochemical experiments such as Homestake [10] were the pioneering ones who observed solar neutrinos. The experimental method consists in measuring the production rate of a radioactive isotope (^{37}Ar) from the neutrino capture reaction on another isotope (^{37}Cl) after exposure of the target to solar neutrinos of order of few months. The results of Homestake, already in 1968, indicated that only about 1/3 of the expected solar neutrino flux was observed on earth.
Kamiokande and Super-Kamiokande experiments are using water as target to look for electron scattering from solar neutrinos in:

$$\nu_x + e^- \rightarrow \nu_x + e^-$$

Kamiokande experiment confirmed the solar neutrino deficit observed by Homestake and indicated a value of the neutrino flux being about 50% of what was predicted. Preliminary (2002) results from the Super-Kamiokande experiment, taking into account seasonal variation of the solar flux, measured a ratio for the observed flux over the expected one of 0.465 ± 0.005 (stat)$^{+0.016}_{-0.015}$ (sys).
GALLEX [11] and SAGE [12] radiochemical experiments are using the neutrino capture on ^{71}Ga to measure the ^{71}Ge production rate. They both have observed a significant deficit. These results are complementary to ^{37}Cl and Super-Kamiokande experiments (sensitive to ^{8}B neutrinos) since ^{71}Ga experiments can detect neutrinos coming from the *pp* reaction.
The question whether the solar model was correct or not was still pending until recent model independent SNO [13] results were presented. By measuring the ratio of neutral-current interactions (involving the three active neutrino flavours) over charged-current interactions (implying only the electron type neutrinos) it provided a measurement of the total neutrino flux as well as independent measurement of the solar ν_e flux. Now the observed deficit is interpreted as the disappearance of solar electron neutrinos by neutrino flavour oscillations.
The KamLAND [14] experiment which studies reactor $\overline{\nu}_e$ that typically travel $\sim$ 180 km to reach the detector, find that, indeed, the $\overline{\nu}_e$ flux at the detector is smaller compared to what it would be if no $\overline{\nu}_e$ were vanishing.
Combined solar neutrino results and KamLAND two-flavour oscillations analysis which were presented at Neutrino 2004 conference give a $\Delta m^2_{12} = 8.2^{+0.6}_{-0.5} \cdot 10^{-5}$ (eV)^2 and $\tan^2(\theta_{12}) = 0.4^{+0.09}_{-0.07}$.

3.4 LSND results

In 1995, the LSND experiment published data [15] showing candidate events that were consistent with $\overline{\nu}_\mu \to \overline{\nu}_e$ oscillations. In the data collected by the KARMEN [16] experiment no potential oscillation event was observed. However due to uncertainties associated to small statistics the LSND claim cannot be excluded despite the fact that, in the allowed region of oscillation parameter space that is compatible with the LSND result, only a small fraction is not excluded by other experiments as shown on Fig 3.2.

If LSND results were leading to so much controversial interpretation in the past years, it is because in a two

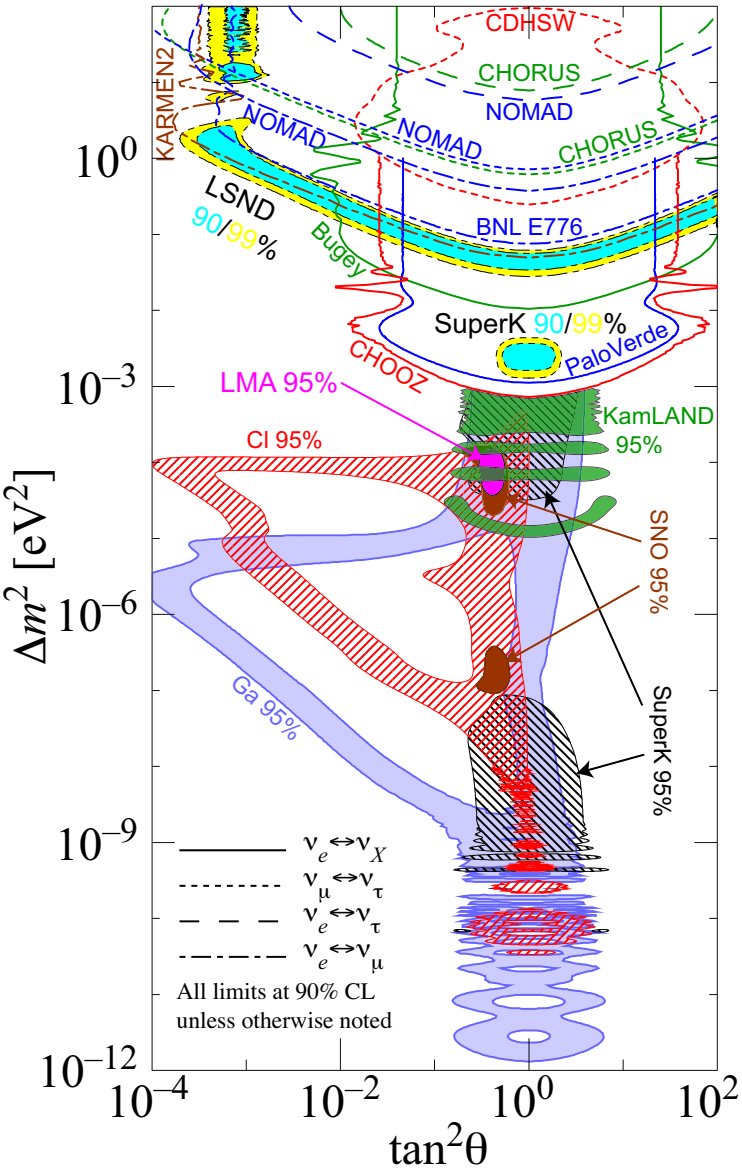

Figure 3.2: Region of squared-mass splitting and mixing angle favoured or excluded by various experiments [1]

flavour analysis the Δm^2 would be above 0.1 (eV)^2. Unfortunately this rather high mass difference is not

accommodating solar and atmospheric evidences in the framework of the Standard Model and three neutrino flavours with non-zero neutrino masses. Proposed solutions to this model include the incorporation of a so-called sterile neutrino state (not sensitive to weak interactions), super-symmetry or CPT violation, thus requiring a independent test of the $\overline{\nu}_\mu \rightarrow \overline{\nu}_e$ evidence of LSND. High statistics coming from the MiniBooNE [17] experiment will help to solve the LSND puzzle.

Part II

The HARP experiment and motivations for K^0_S search

Chapter 4

Motivations for a hadron production experiment

In recent years, a reviving interest in obtaining precise data from a hadron production experiment arose for three reasons. A quantitative design of the pion production, target and subsequent collection system is needed for superbeams and neutrino factory studies. A reliable calculation of the atmospheric neutrino flux is necessary for a refined interpretation of the recent evidence for neutrino oscillations in atmospheric neutrino data. The knowledge of the interaction of hadrons with various types of matter is of interest at the design, simulation or analysis stages of particle physics experiments. Former studies (done about 30 years ago) have explored only small fractions of the phase space and with insufficient precision. Furthermore they were typically restricted to hydrogen and beryllium targets.
While the data from these experiments provide an interesting and welcome overlap, HARP [18] has been designed to cover a much wider range. It carried out a programme of measurements of secondary hadron production, over the full solid angle, produced on thin and thick nuclear targets by beams of protons and pions with momenta between 1.5 and 15 GeV/c. A range of solid nuclear targets across the periodic system, from beryllium to lead, was complemented by cryogenic targets of liquid nitrogen and oxygen, and of hydrogen and deuterium. While N_2 and 0_2 are aimed at a better determination of the atmospheric neutrino flux, H_2 and D_2 serve as connection to the results of earlier experiments. The elastic scattering reaction on free protons from H_2 is a precious independent benchmark.
The HARP measurement requirements are reviewed through the description of the different purposes mentioned above.

4.1 The neutrino factory challenge

Recently, an intense neutrino source based on decays of muons in a storage ring has been proposed [19].
The generic layout of such a neutrino factory (see Figure 4.1) consists of a proton accelerator, a target and a muon storage ring. A high power (4 MW) proton beam impinges on a target producing pions which are collected with a high magnetic field. In a drift space, they decay into a muon and a muon neutrino as follows:

$$\begin{aligned} \pi^+ &\rightarrow \mu^+ + \nu_\mu \\ \pi^- &\rightarrow \mu^- + \overline{\nu}_\mu \end{aligned}$$

After this, the muon phase space is reduced with ionization cooling. This complicated process involves the capture of muons with high transverse momentum and reduction of the ($\overrightarrow{p_T}$,$\overrightarrow{p_L}$) phase-space through

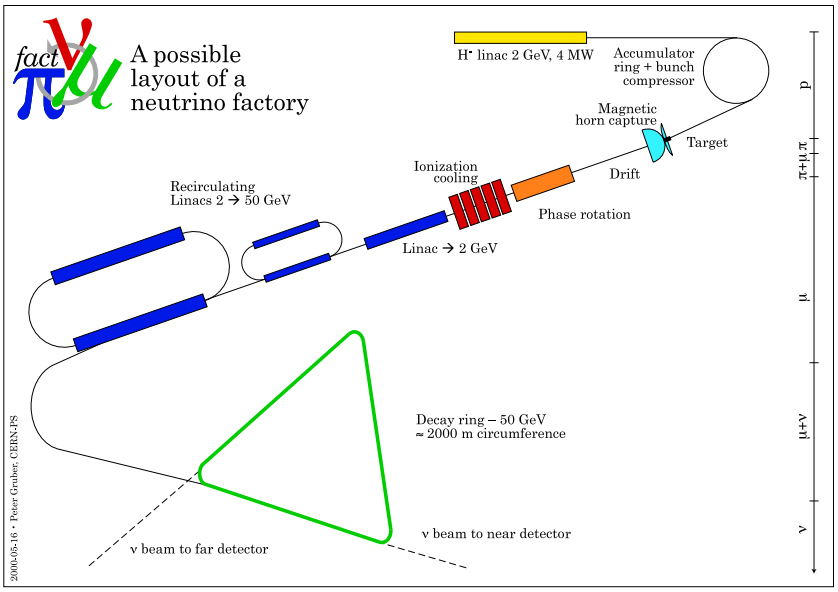

Figure 4.1: Possible layout of a neutrino factory

rotational transformation. The muons are accelerated to energies up to 50 GeV and fed into a decay ring. The muons decaying in the straight sections of this ring produce a high intensity neutrino beam. A combination of 'near' and 'far' neutrino detectors allow precise neutrino oscillation experiments. Decay products are the following:

$$\begin{aligned} \mu^+ &\rightarrow e^- + \nu_e + \overline{\nu}_\mu \\ \mu^- &\rightarrow e^+ + \overline{\nu}_e + \nu_\mu \end{aligned}$$

Such a scenario requires an adequate knowledge of the overall pion yield after capture and phase rotation which can be achieved for different incident proton momenta, thus permitting to get the desired neutrino fluxes and to design a cost-effective machine. Existing data together with current Monte Carlo generators predict the yield with typically 50% uncertainty. One of the feature of neutrino factories is the fact that, in order to increase the phase-space density of particles and to increase π^- production, one tends to choose heavy metal, neutron rich targets (mercury, tantalum) [20] for which very little data is available.
Current simulations of the pion yield from Monte Carlo generators like FLUKA and MARS show a 30-100% discrepancy in the pion production [21] rates for neutrino factories. The reason for this uncertainty is the small amount of underlying experimental data for the simulation programs. The variables affecting the pion production are proton energy, target material and target geometry (diameter and length).
Several target materials have been proposed, starting from low atomic number materials such as beryllium, lithium and carbon to high atomic number materials such as nickel, copper, liquid mercury, or tungsten. In addition, deuterium has been proposed as target material for a recirculating proton scheme [22]. Apart from efficient pion production, cooling the target is a major concern in choosing the right material. Estimates show that, depending on the proton energy, up to 30% of the proton power is dissipated in the target. Even though the proposed experiment is a low-intensity one, hints on the energy deposition in the target can give valuable information to design the target-cooling subsystem.
The data taken in the HARP experiment will be used to validate the design of the neutrino factory downstream the target. The transverse capture and the first phase rotation are strongly dependent on the pion production data. The transverse momentum distribution of the pions must be known to a high precision as it

affects the efficiency of transverse capture. A high precision on the longitudinal momentum is also necessary for the first phase rotation. The overall pion yield per incident proton will be a scaling parameter for the figure of merit of the neutrino factory. A precision of 5% aimed by HARP would be sufficient. The same accuracy is required for the ratio of π^+ to π^-, as the particle with the lower production yield determines the proton power needed. This in turn requires a 2% measurement precision of the integrated flux of pions produced by protons together with a good mapping of the differential production cross-sections. As in the case of a 2 GeV/c proton linac, the largest pion yield is expected for pions with momentum $\sim$ 200 MeV/c, HARP aims at the identification and measurement of pions down to momenta well below 100 MeV/c.

4.2 Needs for the calculation of the atmospheric neutrino flux

Calculations of atmospheric neutrino flux require both the knowledge of the primary cosmic ray flux and the yield of neutrinos per incoming particles. Calculations that have been published in the past years quote large errors and differ significantly in their results [23]. The dominant source of discrepancy was found in the assumed energy spectrum and the chemical composition of the primary cosmic rays. The representation of hadron production in collisions of the primaries with nitrogen and oxygen nuclei is also not complete.
Data on the cosmic spectrum seem to converge and with the results of AMS [24] and BESS [25] the errors under control. This leaves the major source of uncertainty in the calculation of atmospheric neutrino flux as the representation of hadron production (discussed in details in [26]).
HARP data will cover a fraction of the momentum range (1 to 100 GeV/c) of incident cosmic rays and provide usefull measurements from nitrogen and oxygen targets.

4.3 Input for particle physics experiments

Inputs for Monte Carlo generators like GEANT4 [27] for instance, for experiments at the large hadron collider (LHC) or space applications will be provided by the HARP experiment.
Additional motivations came out from the interest in having a better precision in the flux measurements from conventional neutrino beams such as at the KEK (Japan) 12.9 GeV/c proton synchrotron, important for the K2K [28] experiment, and at the low-energy (8.9 GeV/c) booster at FNAL (United States), used for the MiniBooNE experiment. Therefore additional data were taken at 12.9 GeV/c with aluminum targets and at 8.9 GeV/c with beryllium targets.
In order to probe the same Δm^2 region as that explored with atmospheric neutrinos and support Super-Kamiokande results, the K2K experiment uses a neutrino beam produced by an accelerator. The neutrino flux at the Super-Kamiokande detector situated at 250 km distance from the accelerator, is predicted using the flux in the 'near' detector (comprising a 1 kton water Cherenkov detector) and the 'far' to 'near' detector flux ratio R. The ratio is estimated from the beam Monte Carlo simulation and measurements obtained by a pion monitor confirm the Monte Carlo for beam momentum above 1 GeV/c. However, one must rely on hadron production models with large uncertainties in the Monte Carlo simulation below this momentum. Fortunately, neutrinos of this energy range are produced by pions of momentum between 1 GeV/c and 8 GeV/c and at small polar angle. This is a region of the phase space that HARP can probe, increasing thus the interest in HARP data for K2K experiment.
A water target has also been built in 2002 and data have been taken with a 1.5 GeV/c proton beam for a cross-check of the LSND experiment secondary π^-/π^+ ratio of 1:8.

4.4 Physics motivations for a search of K^0_S

In order to better measure the parameters of neutrino oscillations, intense neutrino sources are needed. If nature is providing different sources for neutrino studies such as neutrinos coming from the sun or atmospheric neutrinos as we discussed before, they are not coming with the intensity we would require for high statistics experiments nor at a precise definite energy. Moreover the sensitivity to neutrino oscillation signals is affected by uncertainties on the neutrino flux models we rely on, and an unclear understanding of all the phenomena we have to take into account to understand the neutrino puzzle. An intense single-flavour neutrino source with well defined energy can be provided by the neutrino factory as discussed in Section 4.1.

Conventional neutrino beams, like the existing K2K or MiniBooNE beams or the CNGS [29] project, use the neutrinos produced by the decays of secondaries ($\pi^{\pm}$,$K^{\pm}$...) from the interaction of a proton beam on a fixed target. Such a conventional beam contains neutrinos with different flavours which are not mono-energetic. This is due mainly to the background contamination from charged and neutral kaon decays. If one wants to study $\nu_\mu \rightarrow \nu_e$ oscillations using these conventional beams (as foreseen by the T2K experiment), one has to know precisely the ν_e background contamination in the incoming neutrino flux, originating mainly from kaons. For instance the branching fraction of the decay modes is of order of 5% for the K^+_{e3} channel from K^+ ($K^+ \rightarrow \pi^0 e^+ \nu_e$) and $\sim$ 39% for the K^0_{e3} channel from K^0_L ($K^0_L \rightarrow \pi^{\pm} e^{\pm} \nu_e / \overline{\nu}_e$). A knowledge of the charged and neutral kaon production for different types of target materials and proton beam energies is mandatory for the conventional neutrino beam projects under study in order to optimize the neutrino beam. It would also help to validate the hadronic models used to calculate the neutrino flux in existing conventional neutrino beams. A study of the K^0_S production from the interaction of a proton beam on a fixed target will give hints on the charged and neutral kaon production since their yields are directly related to the strange quark content of the quark sea. Moreover, it can serve as a benchmark to validate the HARP reconstruction algorithms by providing a known mass peak. In particular it is extremely interesting to know the K^0_S production as a function of proton momentum, since kaons are determinant for the ν_e background. HARP, with data taken at 3, 5, 8, 12 and 15 GeV/c is ideally placed to answer these questions.

Chapter 5

The experimental layout

HARP was located in the East Hall of the CERN proton synchrotron, and used the charged particle beam of the T9 beam line. It is a large-acceptance charged-particle magnetic spectrometer of conventional design. It re-used existing equipment as much as possible, notably from the NOMAD [30] and CHORUS [31] experiments and it has been proposed in 1999, mounted in 2000 and took successfully data during years 2001 and 2002. Now the setup has been dismantled and part of the detector allocated to a gas electron multiplier (GEM) time projection chamber R&D [32] for the MICE [33] experiment.

5.1 Overall layout

The experimental layout comprises three main functional parts:

- the beam line, with detectors providing the identification of the incoming particles
- the large-angle spectrometer housing the target
- the forward spectrometer

The HARP coordinate system is defined with the z-axis pointing in the direction of the beam, the y-axis vertically pointing upward and the x- axis horizontally pointing to the left when looking downstream. The center of the coordinate system is, for thin targets, at the upstream face of the target and for thick targets at the middle of the target. The beam line selects secondary particles with positive or negative charges emerging from a primary target in the extracted proton beam from the PS accelerator. Particle identification in the beam line is provided by two gas Cherenkov detectors and a pair of time-of-flight counters. A set of four multi wire chambers measures the position and direction of the beam particles in the experimental target region. Several scintillation counters serve to trigger on single incoming beam particles.

5.1.1 Detector

The global layout of the large-angle and forward spectrometers is depicted in Figure 5.1. It covers a total length of 13.5 m along the beam direction. The large-angle spectrometer is housed in a solenoid magnet. It comprises the target and several concentric layers of cylindrical detectors. At the most inner radius the target is surrounded by six layers of scintillating fibers serving as an interaction trigger. Most of the radial space of the solenoid magnet is occupied by a 1.54 m long and 0.82 m diameter time projection chamber (TPC) which has a double role. It is used to determine the momentum of tracks generated by charged

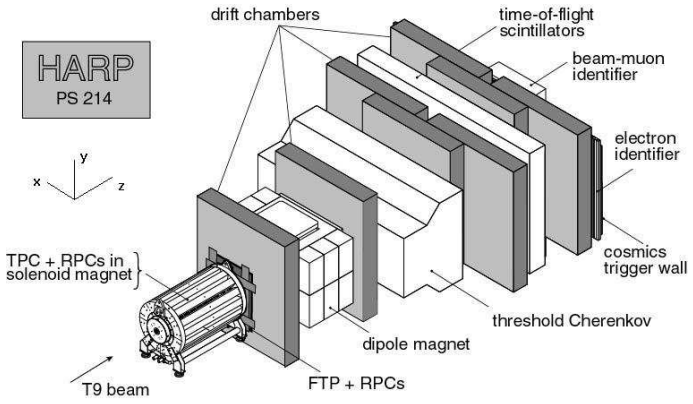

Figure 5.1: Overall layout of the HARP detector

particles over nearly the full solid angle, with emphasis on large-angle (including backward-going) tracks. It serves also to identify pions, kaons and protons at low momenta. The particle identification capabilities of the TPC detector are complemented by a set of multi-gap resistive plate chambers (RPC barrel) surrounding the TPC.
The track momentum measurement in the TPC of the outgoing particles is complemented by the measurement in the downstream spectrometer. While the TPC magnet is mainly devoted to low-momentum and large-angle tracks, the downstream spectrometer measures high-momentum small-angle tracks.
A double plane of scintillation counters placed downstream of the solenoid magnet provides the forward interaction trigger. The downstream spectrometer comprises a quadruplet of NOMAD drift chamber before and another quadruplet after a large-aperture spectrometer magnet. Several additional sets of drift chambers are placed at more downstream positions to follow the particle tracks in between the various particle identification detectors. Separation of forward going protons, pions and kaons is provided by a threshold Cherenkov counter filled with C_4F_{10} gas. A time-of-flight wall provides proton and pion separation at the lower part of the momentum range. The identification of photons is achieved through an iron absorber slab followed by a set of drift chambers and an electro-magnetic calorimeter comprising Pb-scintillating fibre modules recuperated for the CHORUS experiment. The calorimeter is also allowing for the rejection of electrons. A muon identifier is terminating the set of detectors at the most downstream part of the HARP experiment.
The outgoing beam passes through the forward spectrometer. The TPC detector, a plane of resistive plate chambers (RPC forward) and the forward trigger plane contain inactive areas for the outgoing beam. In the case of all other detectors, the outgoing beam passes through active detectors areas.

5.1.2 Targets

The target itself is placed inside the TPC, in an insert, 50 cm downstream of the read-out chamber.
The majority of targets are pure solids of different thickness, covering a large range of nuclei from low atomic number to high one. Data were also taken with replica targets from neutrino beam experiments K2K and MiniBooNE, to help reducing the systematic uncertainties in their calculated neutrino fluxes. They are composed of a single element and have a very high purity ranging from 99.95% to 99.999% except the K2K targets that are made of an alloy containing 98% aluminium. Details about the composition of the small amount contaminants is also known with precision.
The K2K targets have a diameter of 29.9 mm and a length of 650.0 mm and 200.0 mm respectively. They

Material	Thin target (cm)	Thick target (cm)
Solid		
Be	0.81 and 2.03	40.6
C	0.76 and 1.91	38.10
Al	0.79 and 1.97	39.44
Cu	0.30 and 0.75	15.00
Sn	0.45 and 1.11	-
W	0.22 and 0.56	11.14
Pb	0.34	17.05
Liquid (cryogenic)		
H_2	6	18
D_2	6	-
N_2	6	-
O_2	6	-
Liquid		
H_20	6	60

Table 5.1: Set of HARP targets with their thickness

were mounted on fixed aluminum target arms with an inner diameter of 56 mm and wall thickness of 2 mm. The MiniBooNE targets are made of beryllium and have a 3-wing shape (like the Mercedes logo) with 29 mm diameter. Two different targets have been used, one of 406 mm length and one of 163 mm length.
Cryogenic liquid targets have also been exposed to the beam, as well as water liquid targets for LSND background correction to the observed $\overline{\nu}_\mu \rightarrow \overline{\nu}_e$ oscillation signal.
The water targets were 60 mm and 600 mm length and 30 mm diameter mounted in Plexiglas tubes of 2 mm thickness.
The value of 2% of an interaction length (λ_{int}) has been chosen to minimise re-interaction in the target itself, while keeping a reasonable interaction rate. Unfortunately during data taking in 2001 it appeared that the trigger rate was higher than foreseen due to material in the beam line and targets with 5% λ_{int} have been built for 2002 data taking.
The thin targets have the shape of a disc with a diameter of 30 mm.
A number of thick targets were used with the primary aim of checking the simulation of re-interactions. The thickness of these targets is of 100% λ_{int}. They have a rod shape.
The cryogenic target envelope is made of a 125 μm mylar sheet of 35 mm diameter with an entrance window of 20 mm diameter.
A list of target materials is given in Table 5.1. In addition to the normal 'physics targets', specialized targets were used for calibration and alignment.

5.1.3 Magnets

The HARP experiment comprises two magnets. The solenoid magnet houses the target, the inner trigger cylinder (ITC), the TPC detector and the barrel RPC detector. The spectrometer magnet is placed 406 cm downstream of the target.

The solenoid magnet

The solenoid magnet was previously used for a TPC prototype of the ALEPH experiment [34]. It has been extended by 50 cm by adding 20 copper coils and is operated at a field of 0.7 T.
Its magnetic volume has a diameter of 0.9 m and a length of 2.25 m. It comprises 88 copper coils, 74 coils with 16 windings each and 14 coils with 20 windings each. It is operated at a nominal current of 889.4 A. The coils are surrounded by 16 iron beams of 20 × 20 cm size running parallel to the field axis. The magnet is closed by a 15 cm thick cap on the upstream end, leaving a 15 cm diameter hole for the incoming beam and detector supports. The cylindrical volume is left open at the downstream end for the passage of secondary particles to the forward spectrometer. The TPC detector is positioned in the most homogeneous part of the field volume, from 25 cm (z = -500 mm) to 181 cm (z = 1060 mm) into the magnetic volume. Within the volume of the TPC, field measurements have been done by means of a Hall probe and the field along the z-axis is known accurately and differs by at most 3% from the nominal value (downstream and at large radii). The radial component of the field is typically less than 0.5% excepted at large radii where it locally represents up to 1% of the main field. There is no azimuthal field component. Field measurements and Opera 3D [35] field calculations agree with each other within 0.5%. The Opera field values are used in the track reconstruction programs.

The spectrometer magnet

The HARP spectrometer magnet was built about 30 years ago at the Orsay laboratory and was previously used in PS and super proton synchrotron (SPS) hyperon experiments. It has a large aperture of 241 (horizontal) × 88 (vertical) × 172 (depth) cm^3. Large copper coils, two above and two below the 140 (hor.) × 90 (dept.) cm^2 pole piece are operated at a current of 2910 A. Its field is non-homogeneous, its vertical component B_y amounts to 0.5 T in the central region and rapidly approaches zero outside of its aperture. Secondary particles leaving the HARP TPC pass an integral field of $\int B_y dL = 0.66$ T·m. The field of the spectrometer has been mapped with a set of Hall Probes and the results of these measurements were fitted using the procedure described in [36]. The agreement between the measured and fitted values of field is approximately 1% with a total of 183 coefficients found. These coefficients are used to parametrize the field in the reconstruction programs.
The polarity of both magnets has been adapted to the polarity of the incoming beam. Through-going beam particles were systematically bent to the left (+x direction) to fit the acceptance of the downstream muon identifier. For positive polarity beam setting, the magnetic field of the solenoid points in the beam direction (+z direction) and the spectrometer field points vertically downward (-y direction). For negative polarity we get the inverse with a solenoid field pointing in -z direction and the spectrometer field in the +y direction.

5.2 Beam line and beam instrumentation

A resonant beam extracted from the PS machine is sent towards a splitter which allows beams to be alternately sent to the north and south branches of the East Hall. HARP was using the North beam line which puts 400 ms spills of 24 GeV/c protons onto a target, usually made of aluminum. The secondary beam produced is separated into three beam lines T9, T10 and T11, working simultaneously, each with a different maximum momentum of 15, 10 and 3.5 GeV/c.

5.2.1 Beam line

The T9 beam line, which was originally built for test beams, was not optimized for a precision experiment. Its momentum limitation is due to the dipole bending power in horizontal magnets. Particle separation is not provided and there is a very low-energy kaon flux due to decays along this beam line. In general the T9 beam performed well, except at times of very high external temperatures, when there were several dipole magnet trips when running at 15.0 GeV/c. Because of this some of the 15 GeV/c data were in fact taken at a slightly reduced momentum (typically 14.5 GeV/c). The beam length from the primary target to the reference focus (focus B) in the HARP area is 55.81 m. It can provide a maximum of 3 $\times 10^5$ particles per spill of 2×10^{11} protons on the primary target. The spill structure of the beam contains one, two or three bursts per 14.4 s PS cycle. The horizontal dispersion of the beam is corrected. The vertical dispersion is not corrected and will give some increased size to the beam spot in the target. The spot size at our target is of the order of 5×5 mm^2. The beam on the target of the experiment is focused to contain at least 90% of the intensity within a spot size of 10 mm diameter.
When taking data with thick targets the total particle flux had to be kept very low, less than 2000 particles per spill, in order to avoid overlays in the TPC detector. During normal running with thin targets the particle flux was kept below 10000 to 13000 particles per spill for the same reason. An effective way to reduce the flux at momenta below 8.0 GeV/c, was to reduce the current in the dispersion correction quadrupole, this could be done without modifying the normal beam optics. At higher energies the focus on the primary target was increased in size to reduce the overall secondary flux.
During the first data taking period in 2001, there were considerable problems with the beam size because of the large amount of material in the end of the beam line; trigger scintillators, veto and Cherenkov counters, multi-wire proportional chamber (MWPC) causing a significant problem of multiple scattering. This was considerably reduced in 2002 by a strict removal of all materials in the detectors before the HARP target. The other problem found in the 2001 data taking was due to the halo of scattered beam particles close to the beam axis, especially in the vertical plane. This effect was greatly improved in 2002 by installing a vertical collimator upstream of the last quadrupole in the beam line.

5.2.2 Beam instrumentation and trigger detectors

The beam detectors have a double role: they should provide detection, tracking and identification of incoming beam particles and also generate primary signals for trigger decision.
For the trigger logic, the counters can be separated in two groups. On one hand we have the counters in the secondary beam line upstream of the target which are used for beam particle detection and identification (acting as pre-trigger). On the second hand there are the detectors surrounding the target and the one situated downstream of the target which are aimed for detection of secondaries particles emerging from the target itself (acting as confirmation for interaction events).
The beam instrumentation, upstream of the target is composed of:

- a pair of gas threshold Cherenkov counters (BC A and BC B)
- two scintillation halo counters (HALO A and HALO B)
- a time-of-flight system (TOF A and TOF B)
- a set of four multi-wire proportional chambers (MWPC 1 to 4)
- two special scintillation counters a beam scintillator (BS) and a target defining scintillator (TDS)

Beam momentum	BC A	BC B
$\leq$ 3 GeV/c	0.0 (-)	1.05 (e^-/e^+)
5 GeV/c	0.60 (e^-/e^+)	2.50 (π^+/π^-, e^-/e^+)
$\geq$ 8 GeV/c	1.25 (π/π^-)	1.50 (π/π^-)
$\geq$ 12 GeV/c (optional for K-tagging)	3-3.5 (π^+/π^-, K^+/K^-)	3.5 (π^+/π^-, K^+/K^-)

Table 5.2: Basic N_2 pressure setting (in bar) for the beam Cherenkov counters

Nearby and downstream of the target the beam instrumentation is complemented by:

- the ITC
- the forward trigger plane (FTP)

A schematic view of the relative position of the beam and trigger detectors is shown in Figure 5.2. The

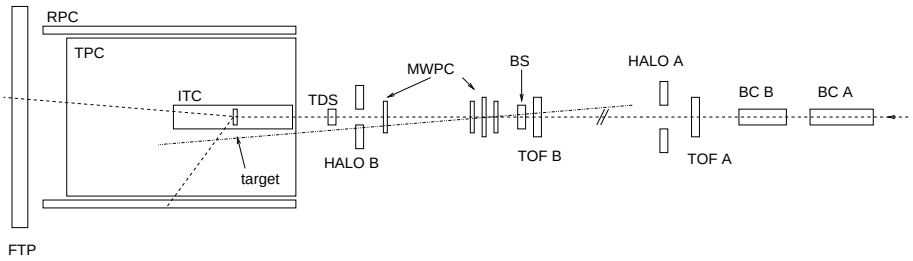

Figure 5.2: Arrangement of beam and trigger equipments, the beam enters from the right

task of beam particle identification is shared between the beam Cherenkov counters and the beam time-of-flight system. Below 3 GeV/c the beam Cherenkovs are used to tag e^-/e^+ with the time-of-flight detectors capable of resolving all other kind of beam particles from pions to tritons. At 5 GeV/c the $\pi^{\pm}$/p separation is done jointly by the beam time-of-flight system and one of the beam Cherenkovs (usually BC B), while the other Cherenkov (BC A) is used to tag e^-/e^+. At higher momenta the e^-/e^+ contamination drops below 1% and at the same time the beam time-of-flight system does not distinguish clearly between pions and protons. The task of $\pi^{\pm}$(K$^{\pm}$)/p separation passes to the beam Cherenkovs.
The tracking of beam particles is performed by the MWPCs which are aligned with respect to the solenoid magnet and therefore with the nominal HARP coordinate system. In practice, all other HARP detectors, primarily the drift chambers, are aligned by reconstructing non-interacting beam particles whose tracks are extrapolated from MWPC measurements.

Beam Cherenkov detectors

The beam Cherenkov counters BC A (5 m length) and BC B (3 m length), belong to the standard equipment of the PS T9 beam line and are located upstream of the T9 focus A. BC A is inserted into two quadrupoles of the T9 beam line. Each counter has a sensitive diameter of about 18 cm. The emitted Cherenkov light is collected with a mirror system to a single photo-multiplier tube. The counters are filled with nitrogen and the pressure is adjusted depending on the beam energy and the type of particle to be tagged as shown on Table 5.2. This was done, in order to meet different requirements for the trigger and to react on major variations of the beam composition. At 3 GeV/c, BC A is evacuated to reduce multiple scattering of the

beam. The measured tagging efficiency of both counters for pions and e^-/e^+ is close to 100%. The limited K-tagging capability at $\geq$ 12 GeV/c, illustrated by Figure 5.3 is adequate given a relatively small fraction of kaons in the beam ($<$ 1%). This option was used mainly during exposure with K2K replica targets at

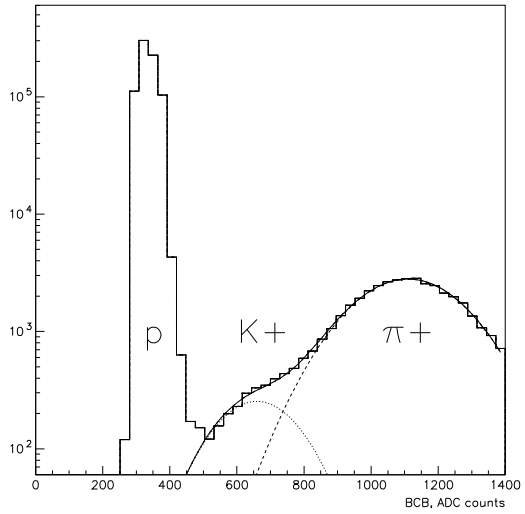

Figure 5.3: Pulse height spectrum from the BC B for a positive 15 GeV/c beam

12.8 GeV/c, for which a very pure proton beam was requested.

HALO counters

The two halo counters serve to veto events which are accompanied by a second particle in the halo of the beam. They are read-out at both sides with photo-multiplier tubes. HALO A located near the reference focus in the T9 beam line area (focus A) has a hole diameter of 9 cm. The final cleanup of the beam is done by HALO B (see Figure 5.4) situated as near to the target as possible (at 1.51 m from it). It has a hole diameter of 3 cm. To convert photons, a 11 mm ($\sim$ 2 X_0) thick lead plate is sandwiched between the two scintillators slabs. The counters are mounted with a rotation of 45° around the beam axis. The size of a single scintillator slab is 200 $\times$ 200 $\times$ 5 mm^3. To achieve a maximum veto-efficiency, each halo counter enters the trigger with a logic OR of its channels.

Beam time-of-flight system

The beam time-of-flight system comprises two counters TOF A and TOF B, recuperated from the NA52 experiment. It is used for beam particle identification up to 5 GeV/c. In addition, the beam momentum can be accurately determined by comparing the measured velocities of pions, protons and deuterons of the same beam, as illustrated by Figure 5.5. The purity of the beam particle identification is better than 99%. The counters are made of a plane of Bicron BC-404 scintillators 10 $\times$ 10 cm^2 surface and 5 mm thickness. The scintillator is divided into eight strips of width growing from 0.8 cm to 2.0 cm at the outer edge. Every scintillator strip is matched to a Plexiglas light guide and read at both ends by photo-multipliers (see Figure 5.6). The average time-of-flight resolution is of $\sim$ 150 ps over a 21.4 m distance between the two counters.

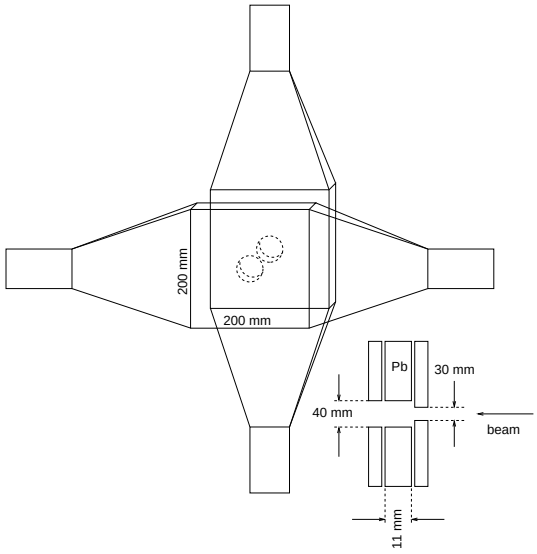

Figure 5.4: Layout of the HALO B, the beam direction indicated is valid for 2001 only. In 2002, the two planes were swapped.

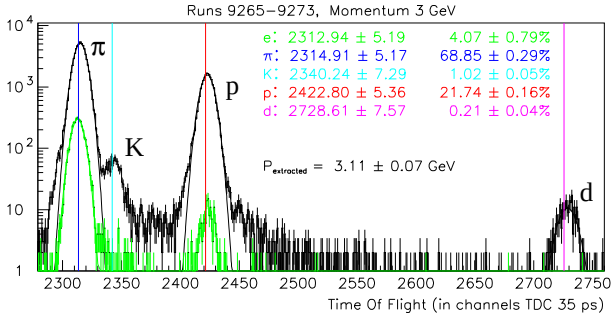

Figure 5.5: Beam particle identification with the beam time-of-flight system for a 3 GeV/c beam momentum. Electrons are tagged with both Cherenkovs.

Beam multi-wire proportional chambers

The beam MWPCs (see Figure 5.7) are used for the off-line reconstruction of the beam particles, as well as for real-time beam tuning and beam quality monitoring. They provide measurements of the beam particle position and angle extrapolated at the target with an accuracy of < 1 mm and < 0.2 mrad, respectively by using the coordinates in the 8 different planes. They are located not too far (between ~ 1.263 m and ~ 3.93 m) from the target in order to reduce multiple scattering effects between the track measurement and its extrapolation at the target. They are standard refurbished CERN beam chambers, of type XWCA (chambers 1 to 3) or XWCM (chamber 4). Each chamber is made of two adjacent 10-mm wide detection gaps with an anode sense wire plane in the middle of each gap. The wire planes are perpendicular to each other. The cathode planes (the middle one being in common for the two gaps) are made of 20 μm thick aluminized Mylar foil. MWPC1, MWPC2 and MWPC3 are used for particle tracking. They have a wire pitch of 1 mm with the sense wires parallel to the x and y axis of the HARP coordinate system. The larger chamber, MWPC4, is rotated by 45° and has a 4 mm wire pitch. Its purpose it to resolve the tracking

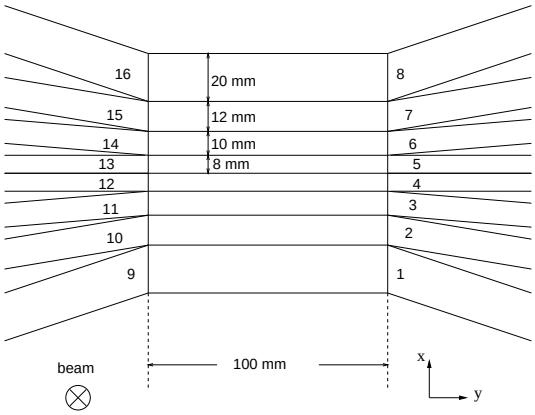

Figure 5.6: Layout of the TOF A and TOF B counters

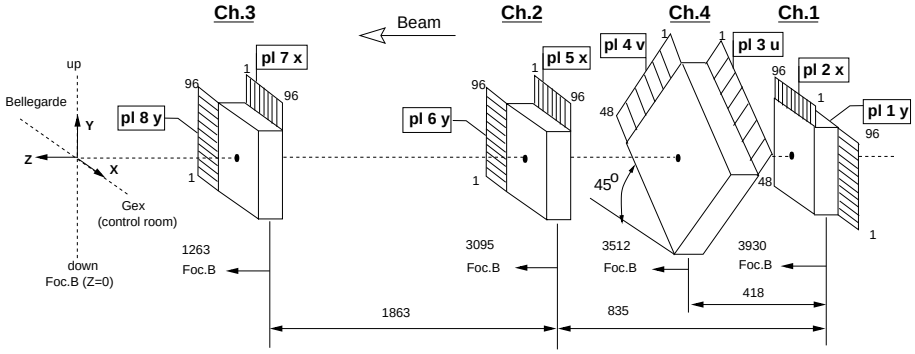

Figure 5.7: Layout of the HARP beam MWPCs

ambiguity in two-track events and to detect beam halo particles. The gas mixture is 50% Ar 50% CO_2 with an addition of 0.5% of water vapor to prevent high voltage trips on the wire planes. The high voltage settings have been chosen so as to maintain the efficiency between 99 and 100% for each chamber and at the same time to keep the average multiplicity to 1.1.

Beam scintillator

The BS is located a few centimenter downstream of TOF B. It starts the decision logic of the trigger system. In coincidence with the logical 'or' of all TOF B channels it represents the lowest-level trigger called STROBE which provides the timing reference for all other detectors. It is made of a single scintillator slab of 5 mm thickness and a sensitive area of 80 $\times$ 80 mm^2 centered on the nominal beam axis and is read out by a single photo-multiplier tube.

The target defining scintillator

The TDS is a scintillator disc of 20 mm diameter and 5 mm thickness viewed by four photo-multiplier tubes as shown on Figure 5.8. The photo-multipliers are located at a distance of approximatively 20 mm from the edge of the scintillator and optically connected via a tube made of reflecting mylar foil acting as an air light guide. The photo-multipliers are housed in iron blocks in order to shield them from the magnetic stray field of the solenoid. It is designed to have a very high efficiency with the task to define a subset of beam

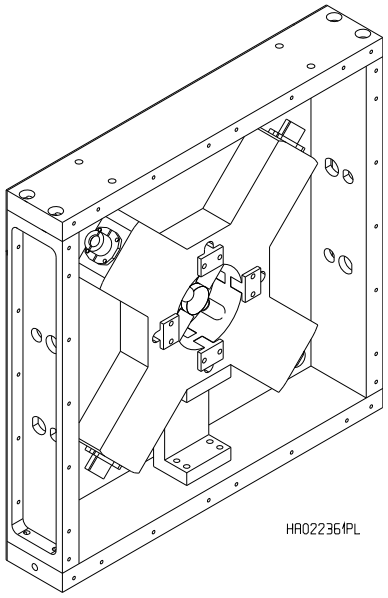

Figure 5.8: Design drawing of the target defining scintillator (TDS)

particles which are guaranteed to hit the target. Therefore it is located as near as possible to the entrance of the TPC. It will give a signal if at least one photo-multiplier was hit. An efficiency of well above 99.9% is assured. It has a sufficiently good time resolution and stability to be used as additional detector for the beam time-of-flight system.

The inner trigger cylinder

The ITC is mounted inside the inner-field cage of the TPC and consists of an aluminium/carbon tube 130 cm long, with a inner diameter of 76 mm and a outer diameter of 92 mm. Six layers of scintillating fibers (each of diameter 1 mm) are glued on the tube. The readout is performed by 24 photo-multipliers contained in an iron magnetic shield on the upstream end cap of the solenoid magnet. They are connected to 24 fibre bunches as shown on Figure 5.9. The fibres of layers 1 to 4 are organized in 8 bunches per layer parallel to the z axis and arranged at different ϕ angles. From one layer to the next the fibre bunches situated at a different radius are superimposed. They are read out by photo-multiplier 1 to 16, a given photo-multiplier reading at the same time two superimposed fibres bunches. The fibre bunches of layers 5 and 6 are wound around the cylinder with an angle of $\sim 24^\circ$ compared to the z -axis and in opposite sense with 8 bunches per layer. They are connected to photo-multipliers 17 to 24, the same photo-multiplier reading two bunches situated at two different layers at the same time. The ITC provides a trigger for large-angle secondaries emerging from the target. Triggering on a logical 'or' condition of all 24 channels provides a combined efficiency for a single track detection well above 99%.

The forward trigger plane

Located downstream of the solenoid, the forward trigger plane covers the small forward angle region and is complementary to the ITC in detecting interactions. It is made of two planes of Bicron BC-408 scintillator slabs as shown in Figure 5.10. Each plane consists of seven scintillators, 1240 (length) $\times$ 200 (width) $\times$ 5 (thickness) mm^3. Each slab is read out on both sides by fine-mesh photo-multipliers that were previously

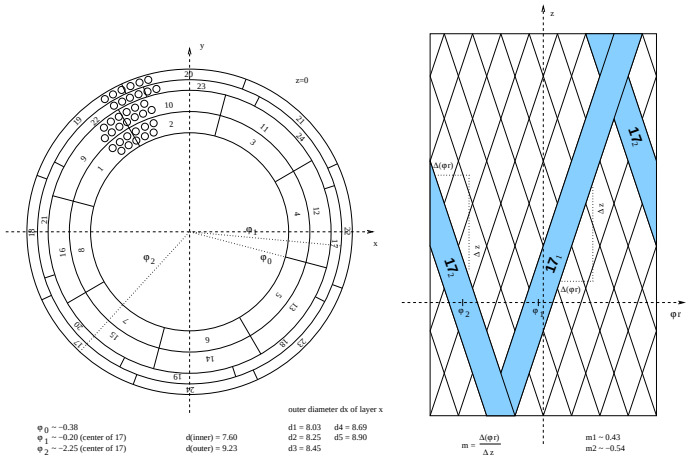

Figure 5.9: Layer and photo-multiplier arrangement of the ITC

used in the trigger system of the NOMAD experiment. The planes are rotated by 90° with respect to each other in order to minimize the insensitive areas due to the spacing between the scintillators.

5.3 The HARP sub-detectors

5.3.1 The Resistive Plate Chambers

Resistive plate chambers have been chosen as the time-of-flight system in the large and medium angle acceptance region. They were designed for high detection efficiency and a time resolution of 200 ps, sufficient to separate low-momentum electrons and pions even at short flight distances of 0.5-2 m between the target and the RPCs. They are intended to provide particle identification for momenta in which the $\mathrm{d}E/\mathrm{d}x$ measurement in the TPC cannot distinguish between electrons and pions (100-250 MeV/c), electrons and kaons (500 MeV/c) or electrons and protons ($\sim$ 1 GeV/c). The RPCs system consists of 46 identical chambers, 10 mm thick, 150 mm wide and 2 m long. Thirty of them are arranged in a barrel in the 25 mm radial space left between the TPC outer field cage and the solenoid coil. The remaining 16 constitute a wall perpendicular to the beam and placed downstream of the TPC. The latter cover a medium-angle range which is not covered by the forward spectrometer. The barrel RPCs [37] are arranged in two overlapping layers. The forward RPCs are arranged in four groups of four overlapping RPCs each as shown on Figure 5.11. The RPCs were operated in avalanche mode with a 90% $C_2F_4H_2$ - 5% SF_6 - 5% iC_4H_{10} gas mixture. Their performance has been described in detail in [38].

5.3.2 The Drift Chambers

The NDCs [39] have served as the active target of the NOMAD experiment and as such were more 'massive' than ordinary drift chambers. Each chamber consists of three gas gaps of 8 mm each, separated by four 1.5 cm thick honeycomb structured panels, in total representing 2% of a radiation length for a complete chamber. The wire directions are vertical and +5° and -5° from the vertical. This small stereo angle allows for 3-D reconstruction with full precision in the horizontal plane, useful for momentum measurement. The sense wires are equally spaced and provide drift cells of ± 3.2 cm around each sense wire, the cells being separated by potential wires. The sense wires are held at +1300 V and the potential wires at -2900 V. The

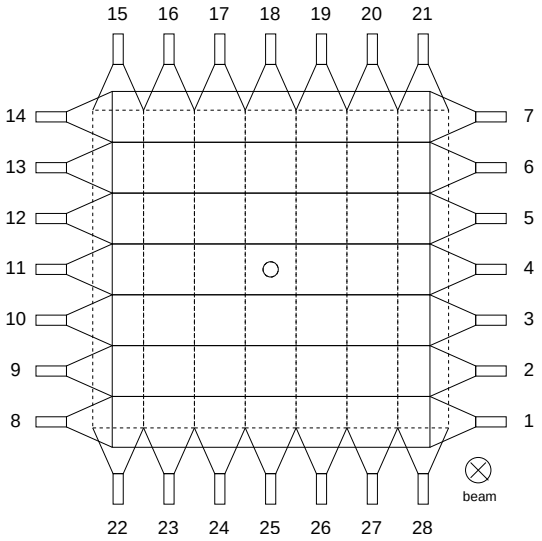

Figure 5.10: Layout of the forward trigger plane

field shaping is obtained through aluminium strips glued onto the panels and held at decreasing potential between -2900 V and 0 V, providing a drift field of $\sim$ 900 V/cm. The chambers are grouped into five modules of four chambers each. Each module covers a 3 $\times$ 3 m^2 surface in the X-Y plane. Two modules placed upstream and downstream of the spectrometer magnet act as tracking device for the forward going particles. Then a group of three modules is arranged to cover the full acceptance for particles deflected by the spectrometer magnet. Finally a group of three modules containing a single chamber each, is placed in front of the electromagnetic calorimeter and acts as pre-shower. For fully equiped modules, a charged particle can leave up to 12 hits in each traversed module allowing a fairly accurate segment reconstruction. Because of safety reasons it was not possible to re-use the same gas mixture as in the NOMAD experiment and a Ar(90%) - $C0_2$(9%) - CH_4(1%) gas mixture has been chosen as a compromise decreasing the overall hit efficiency down to 80%. There is also a loss of efficiency due to the spacers that maintain the 3 m long wires at the centre of the gas gap. The average space resolution obtained from an alignment procedure using cosmics events reaches 340 μm. This value is about two times worse than what has been measured in NOMAD. The gas mixture can be invoked here, the longitudinal dispersion of the drifting electrons and the much reduced size of the plateau in the drift velocity distribution as a function of the electric field, both contribute in degrading the resolution. Furthermore the chambers have a low efficiency around the beam especially for the first module where at the beginning of the spill the chamber is saturated. The resulting efficiency for forward tracks reconstruction amounts to $\sim$ 80% in the region of interest for physics analysis (see figures in Appendix D).

5.3.3 The Cherenkov detector

At large incident proton energy, the secondary meson and proton momenta increase, and the particle identification capabilities of the TOF in the forward direction has to be supplemented by another technique. In addition to the proton/pion separation issue, the strange-particle contamination of the pion sample also increases. By simulation, the kaon contamination is more severe at large momenta of the secondaries, i.e in the forward region, where the ratio K^+/π^+ is estimated to be about 5%. Approximately 95% of the pions above 3 GeV/c are concentrated in the polar angle region $\theta < 200$ mrad, and therefore the 'high momentum'

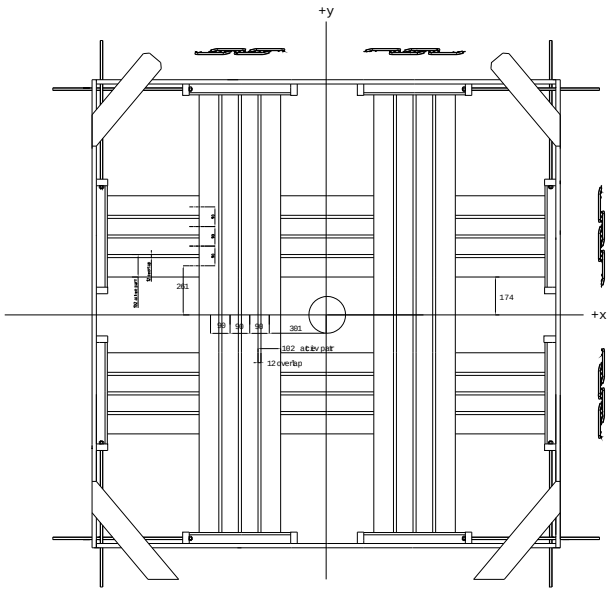

Figure 5.11: Arrangement of the forward RPCs

particle identification can be restricted to this domain. To this aim a gas Cherenkov detector (CHE) was positioned downstream of the spectrometer magnet. The horizontal width has to cope with the defocussing of the magnet for secondary particles. The vertical acceptance is limited by the aperture of the spectrometer magnet. Perfluorobutane C_4F_{10} gas has been used for the radiator which was operated at atmospheric pressure and in threshold mode. The structure of the Cherenkov detector is made of a large steel frame with an opening 6 m wide and 3 m high. This frame supports two horizontal rows of 19 photo-multipliers (PMT) each, one row on the top and one on the bottom. On the frame are also fixed the suspensions of the two sets of mirrors. Two large boxes made of thin walled stainless steel on an aluminium structure forms a vessel of volume 31 m^3. The boxes are welded directly on the steel frame. They are equipped with large honeycomb panels on the entrance and exit path of the particles. The particles traverse about 2 m of the radiating medium and generate photons that are deflected by about 135° upward or downward by two large cylindrical mirrors 6 m long and with a radius of curvature of 2.4 m. The average reflectivity of the mirrors was about 90%.

5.3.4 The time-of-flight wall

Excellent timing resolution for particle identification and good transverse segmentation to avoid particle pile-up on single counters were required for the time-of-flight wall (TOF) system. Its specifications called for a time resolution of $\sigma \simeq 250$ ps to separate at 4σ pions from protons up to 3.5 GeV/c, on the basis of a 10 m flight path [40]. The mechanical structure is shown in Fig. 5.12. There are two types of counters: 13 slabs, 180 cm long placed horizontally and 26 slabs of 250 cm long placed vertically. In each wall the counters are partially overlapped by 2.5 cm to ensure hermetic coverage. Moreover the particles which pass through the overlapping areas can contribute to cross-calibrate the counters in a given wall. Two additional sets of scintillation counters ('calibration counters') are placed, respectively upstream and downstream the TOF wall to trigger on cosmic events. The intrinsic resolution of the scintillator counters is of $\sim$ 160 ps. The TOF A and TOF B signal together with the TDS is providing a reference time t_0 acting as a 'start' time. With the time measured in the time-of-flight wall t_W acting at a 'stop'time, the momentum of the

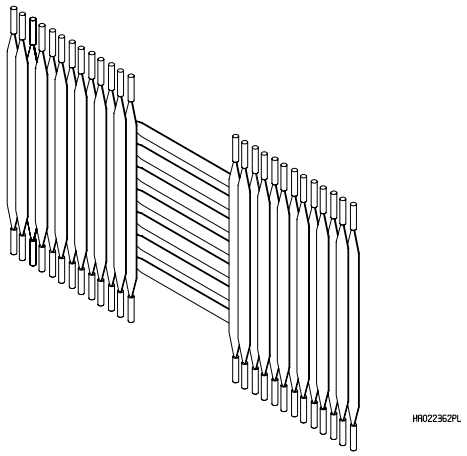

Figure 5.12: Layout of the time-of-flight wall system

particle as measured by the NDCs, pion-proton separation can be achieved at more than 3σ up to 4 GeV/c momentum with a time-of-flight resolution of $\sim$ 200 ps.

5.3.5 The electron identifier

The electron identifier was designed to provide electron-pion separation when charged pions, accompanied by knock-on electrons, are occasionally misidentified by the Cherenkov detector. It helps also in identifying photons, electrons and hadrons. The HARP electron identifier apparatus is composed of:

- an iron photon converter (2 cm thick)
- three NOMAD drift chambers (see Section 5.3.2)
- two planes of existing calorimeter modules EM1 and EM2 recuperated from the CHORUS experiment
- a plane of scintillators used as a trigger for cosmic muons

The photon converter detects a good fraction of photons coming from π^0 decays. The parent particle is identified through the two photon invariant mass reconstruction on the assumption that both γ particles originate from the target centre. The two calorimeter planes, consist of 62 and 80 modules respectively corresponding to 4.96 m and 6.4 m active width. The modules are placed vertically in a support frame. EM1-type modules are 2.62 m long 8 cm wide and and 4 cm deep, corresponding to 5.37 X_0 and 0.19 $\lambda_{\rm int}$. EM2-type modules are 3.35 m long 8 cm wide and 8 cm deep corresponding to 11 X_0 and 0.4 $\lambda_{\rm int}$. Figure 5.13 gives the particle yield as a function of the momentum of the particle p, the energy deposited in the first plane E_1 and the sum E of the energies $E_1 + E_2$ deposited in both planes for a 3 GeV/c beam and no target, showing that electron and hadrons are well separated.

5.3.6 The beam muon identifier

The muon identifier (represented together with the electron identifier in Figure 5.14) is the most downstream part of the HARP setup. It serves to identify muons that come from decays in flight of pions and kaons. It measures also the muon content of the beam. The detector consists of a 40 cm iron block followed by five scintillator planes. Each plane consists of six horizontal scintillator slabs of 200 mm $\times$ 6 $\times$ mm $\times$ 2500 mm. Each of these planes of scintillator is separated by three or four 5 cm iron plates.

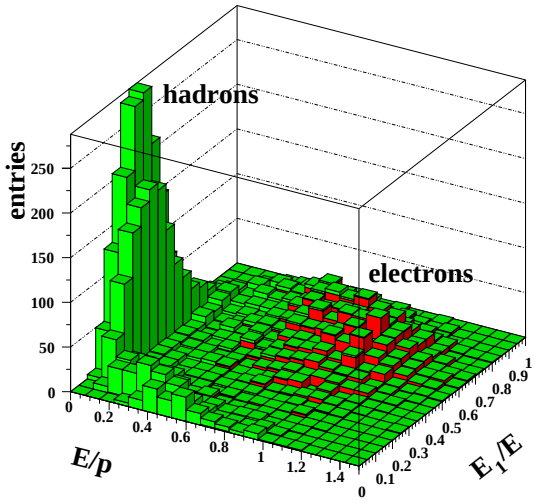

Figure 5.13: Particle yield in the electron identifier for 3 GeV/c beam and no target.

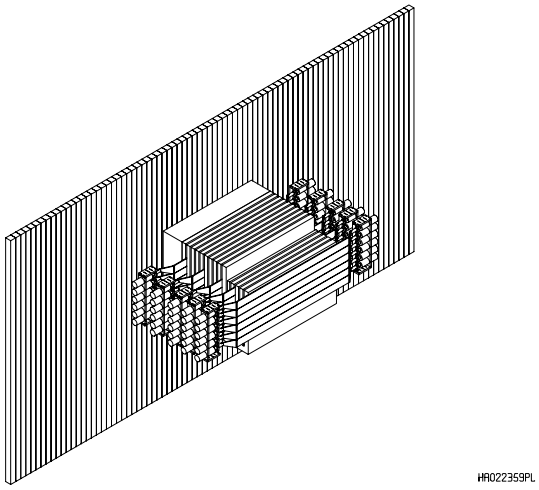

Figure 5.14: Schematic view of the electron and muon identifiers

Chapter 6

Detector operation

6.1 The Trigger system

The design of the trigger system is driven by the capabilities of the data-acquisition system (DAQ), the performances of the beam, the main features of the interactions to be studied and the required precision of the measurement envisaged. The characteristics of the interactions vary greatly over the energy range of the experiment. At high energy, pion and proton production rates are roughly equal. Since both measurements are required, no selection on particle type will be needed in the trigger.

6.1.1 Central Trigger

The central trigger system handles the distribution of physics trigger signals, veto/busy logic and spill/gate signals to the Versa Module Europa (VME) crates. Each sub detector has a dedicated VME-PCI interface used as crate controller and called local data concentrator (LDC), with the exception of the NDCs and the RPCs each controlled by two LDCs. The TPC has one master LDC and six slaves LDCs as shown on Fig. 6.1. The Cherenkov is read out by the trigger subsystem, due to its small number of channels. The

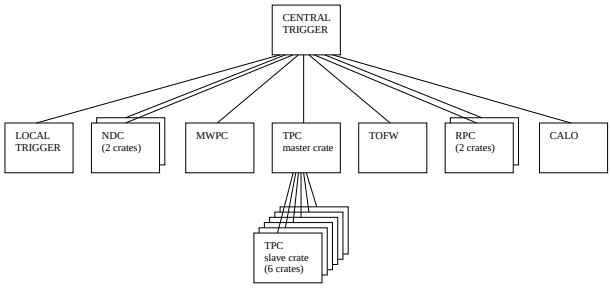

Figure 6.1: The central trigger logic

central trigger (LDC 16) performs the global trigger decision and distributes the information to the interrupt modules called CIRQs [41] of the LDC of the second level (LDCs 1-9). The TPC master crate serves the six slaves crates (LDCs 10-15) with trigger signals and communicates their 'busy' back to the central trigger. Between spills calibration triggers can also be taken by each system.

HALO	HALO A + HALO B
BEAM	STROBE × TOF A × TDS × !(HALO)
BEAMPION	BEAM × BC B
INTERACTION	BEAM × (FTP + ITC)
PION	BEAM × CHE × !(BEAMPION)

Table 6.1: Some of the standard physics trigger conditions

6.1.2 Spill synchronization

The central trigger generates several gates in order to assure that the spill and the inter spill period are clearly separated. The minimum delay between the beginning of two consecutive spills is about 2 s. The gate during which physics triggers are accepted is referred to as PS-GATE, whereas the inter spill gate for calibration triggers is called COSMIC-GATE. In addition, all LDCs are informed about the beginning of spill (B-SPL) and its end (E-SPL). B-SPL and E-SPL are stored as special events.

6.1.3 Physics triggers

The trigger logic defines a PHYSICS-TRIGGER to enrich the sample of beam particles having caused an interaction in the target. The central part of the PHYSICS-TRIGGER decision is a programmable logic unit (PLU). It has been designed for the trigger of the CHORUS experiment [42]. When a STROBE (coincidence of BS and TOF B) is received, 16 input bits are latched and according to a lookup table a pattern of 16 output bits is generated. Input signals are logic signals of all detectors which are of importance for the trigger: TOF A, TOF B, BS, TDS, HALO A, HALO B, BC A and BC B as beam detectors and FTP, ITC and CHE as interaction detectors. The PLU allows for a maximum flexibility for the trigger configuration: the lookup table is loaded at the beginning of each run and may therefore be adapted to different conditions like beam momentum, beam composition and target. To generate the lookup tables a program produces a text file with all 2^{16} possible input combinations and their corresponding output words. Each pattern has a unique name and version number which is written into the data as part of the START-OF-RUN event as well as the 16 output bits themselves. Some standard physics trigger condition used in the runs from which we retrieved data are given in Table6.1 A standard physics trigger condition for thin target is INTERACTION. For thick targets a signal in FTP or ITC is not required since most beam particles interact in the target. For beam configurations with extremely high electron content, one of the beam Cherenkov was used to veto these events at the trigger level. BS × TOF B coincidences can only strobe the PLU when the detector or PLU are not already occupied (BUSY logic). Care is taken that after the readout is finished or the event is rejected the BUSY is released. All STROBE signals also have to pass the spill gate.

6.1.4 Normalization trigger

For the precision requirements on the normalization in HARP it is mandatory that a down-scaled sample of minimum-biased data is recorded. Obviously, the least biased trigger condition is the STROBE. Thus a certain fraction of all STROBE reaching the PLU is read out, no matter whether they caused an interaction or not. The value of the down-scale factor (typical value being 32 and 64) is adjusted in such a way that the down-scaled STROBE events do not substantially reduce the number of PHYSICS triggers. At the same time sufficiently many have to be acquired in order to reduce the statistical error of the normalization. These events have a trigger pattern called DOWNSTROBE.

6.1.5 Calibration trigger

Apart from physics and normalization triggers provided by the PLU also calibration events have to be taken: pedestals events, pulser-related events and events induced by cosmic muons. Common to these events is that there are taken separately by a single subsystem or a set of subsystems. These triggers are acquired during an inter spill gate (except for the TPC laser events). Pedestal events are taken at the beginning of a run. These data are used to monitor the pedestals of all ADC channels as well as to calculate their values and feed them back into the modules for an on-line zero-suppression. Cosmic muon events are used for calibration and alignment. For those, the HARP detector is divided into subsystems which take data independently:

- TPC cosmics trigger (also referred as 'upstream' cosmics trigger) where TPC + RPCs are read out. The trigger signal is provided by a coincidence of signals in any pair of opposite RPC modules.
- NDC cosmics trigger ('downstream' cosmics trigger) where NDCs and calorimeter are read out. The trigger signal is a coincidence of the FTP, the TOF wall and the cosmic wall made of a large array of 29 scintillators each of 320 $\times$ 20 cm^2 $\times$ 0.6 cm, and installed downstream of the last NDC modules..

6.2 The software framework

The HARP software is based on Object Oriented design with a C++ language implementation for the data off-line analysis. Commercial software products supported by CERN were exploited where necessary. The software architecture is schematised in Figure 6.2. A short description of the functional mandates and names

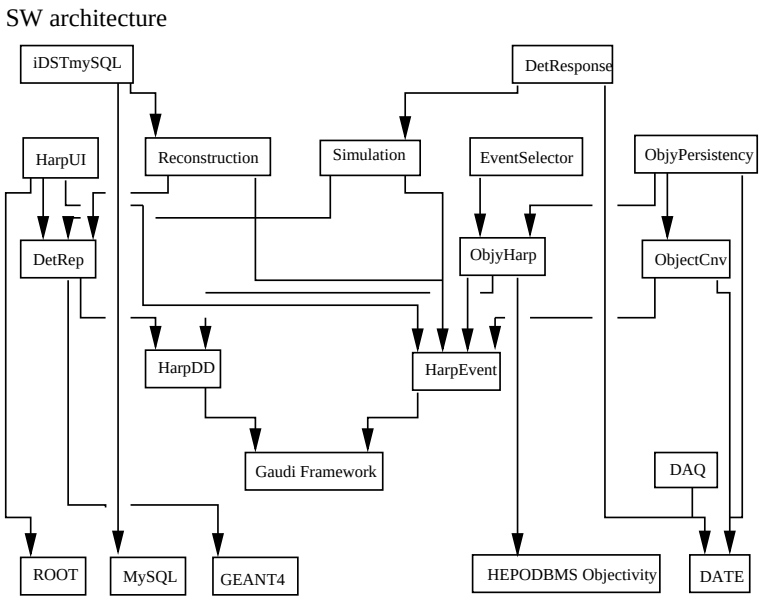

Figure 6.2: HARP software architecture of the second software cycle

of the main software components is given in the following lines:

- ROOT [43] is the C++ based statistical analysis and visualization tool contemporary to the old-known graphical interface PAW.

- MySQL [44] is an open source database written in Standard Query Language (SQL).
- GEANT4 is a simulation toolkit for high energy physics including models for the physics of particle traversing materials.
- HEPODBMS is the database for high energy physics using the commercial proprietary Objectivity/DB (Objectivity, Inc., U.S.) database.
- DATE [45] is the data acquisition prototype of the ALICE experiment at CERN.
- Gaudi Framework [46] is the service that provides storing, messages and histograms. It has been developed on by the LHCb experiment at CERN.
- DAQ (see Section 6.3) is the HARP data acquisition software based on the DATE package and written in C language.
- HarpDD is the component implementing the HARP detector geometry and materials data in a neutral representation format. It also contains the alignment and calibration data description.
- HarpEvent is the component implementing the HARP transient event model, including a structured description of settings, reconstruction objects, Monte Carlo information. It is based on the Gaudi Framework.
- DetRep is the component creating the various geometrical representations of the detector objects most suitable for use by the physics applications. It is based on GEANT4 solid modeling.
- ObjyHarp is the component implementing the HARP persistent event model. It is based on Objectivity/DB database, and mirrors the transient event model. In 2003 HARP migrated its data to the commercial proprietary database Oracle (Oracle Corporation, U.S.), thus an equivalent component implementing the HARP persistent model in Oracle exists.
- ObjectCnv is the component implementing the unpacking of the raw data and the construction of the transient C++ objects used by the physics applications. It can be used transparently both for on-line data and stored off-line data, as well as Monte Carlo output.
- HarpUI is the component implementing the event display. It is also used on line and based on ROOT.
- Reconstruction is the component implementing the computation of reconstructed objects at various levels. For instance it produces the clusters, tracks and particles for the TPC and RPC detectors, and it produces triplets, segments tracks and particles for the NDC and forward detectors.
- Simulation is the component of the HARP Monte Carlo. It is based on GEANT4. It has also been used for the T9 beam simulation, and for understanding and resolving the FTP and ITC fake trigger problem.
- EventSelector is the component implementing the event selection and data navigation facility.
- ObjyPersistency is the component implementing the adapter to use the Objectivity/DB database, while allowing the physics applications not to depend at compilation time from the I/O solution (equivalent functionality exists for Oracle).

- iDSTmySQL is the component implementing the intermediate data summary tape (iDST) concept for distribution in the collaboration. It contains the persistent capable physics objects (including reconstruction, simulation, geometry, and event model objects). It supports both a neutral file format and Linux mySQL.

- DetResponse is the component implementing the digitization and the detector response for simulation.

The entire software chain can be reprocessed on the data if they are stored in iDSTmySQL without any need to access the HARP mass storage system (CASTOR) and central databases (Objectivity/DB, Oracle). This allows full distribution of the analysis work in the HARP institutes. The different versions of the software are maintained and made available via the CMT (based on CVS) system.

6.3 The data acquisition system

The HARP data acquisition system is organized around two switched 100 MBit/s Ethernet networks, linking readout processors, event-builders, recording facilities, monitoring and control workstations. The decision to base the readout hardware on VME, the readout processing nodes on 32-bits Intel processors, and the operating system on Linux, has very much simplified the development and the deployment of the system. The core of the DAQ system (readout, recorder and event-builder) is written in the C language. Tcl/Tk [47] has been used to implement the run-control processes and graphical panels. Higher-level applications, like objectification, on-line monitoring and logging, are written in object-oriented language like C++ and Java. Depending on the beam momentum, the target configuration, and the running conditions, the actual event rate was between 200 Hz and 400 Hz. The DAQ was designed for a maximum event rate of 2.5 kHz, corresponding to 1000 events per spill. The TPC, due to its readout cycle of more than 30 μs and its data size, limited the maximum rate to about 500 events per spill. The total event rate strongly depended of the number of spills per PS cycle assigned to HARP. The maximum rate in normal data-taking mode has been about 6 MBit/s comfortably split in the two available recording pipelines. Special calibration runs, when the trigger was continuously active, were able to saturate the pipeline with a rate of about 20 MBit/s. The DAQ and recording system showed excellent stability, with an overall efficiency of 88% during the first year of data taking and about 95% during the second year.

6.4 The detector control system

The HARP experiment is controlled and monitored by the detector control system (DCS). The system consists of two independent sub-systems, one for the control and monitoring of the high voltage power supplies, called HVC, and the other for the monitoring of analog and discrete (boolean) signals, called ADSM. The high voltage control deploys the PVSS-2 software environment in the first supervisory PC computer and accesses data through the distributed information management (DIM) client-server application. The server is located into two front-end PCs for the high voltage power supplies which run Linux software and communicate with the first supervisory PC. The ADSM is based on the commercial National Instruments FieldPoint system running under the commercial LabView on the supervisory PC. The FieldPoint network PC runs the commercial Windows NT operating system and accesses the network via two server applications. The PC communicates with a client in the second supervisory computer, where LabView runs under the commercial Windows 2000 operating system. In total more than 1000 parameters were monitored at intervals of $\sim$ 10 s. All detector parameter data were written to a database at $\sim$ 2 min. intervals.

Target	Beam momentum (GeV/c)	Length or λ_{int}	Events (10^6)
Be	±3, ±5, ±8, ±12, ±15	2%, 5%, 100%	37.4
C	±3, ±5, ±8, ±12, ±15	2%, 5%, 100%	30.7
Al	±3, ±5, ±8, ±12, ±15	2%, 5%, 100%	34.5
Cu	±3, ±5, ±8, ±12, ±15	2%, 5%, 100%	36.6
Sn	±3, ±5, ±8, ±12, ±15	2%, 5%	23.7
Ta	±3, ±5, ±8, ±12, ±15	2%, 5%, 100%	38.2
Pb	±3, ±5, ±8, ±12, ±15	2%, 5%, 100%	44.9
K2K	+12.9	5%, 50%, 100%	15.3
MiniBooNE	+8.9	5%, 50%,100%	22.6
N	±3, ±5, ±8, ±12, ±15	6 cm	13.0
O	±3, ±5, ±8, ±12, ±15	6 cm	15.5
H	±3, ±5, ±8, ±12, ±15	6, 18 cm	32.0
D	±3, ±5, ±8, ±12, ±15	6 cm	21.0
Water	+1.5	10%, 100%	6.4
Pb, Ta, Cu	+1.5	5%	3.2

Table 6.2: HARP data summary

6.5 Summary of HARP data

In total about 420 millions of events have been recorded for different beam polarities and momenta and various target materials. The summary of HARP data is given in Table 6.2.

Part III

The HARP Time Projection Chamber

Chapter 7

The time projection chamber

The HARP time projection chamber provides tracking and particle identification for secondary particles in the large-angle region between 20° and 160°. It consists of a field cage comprising a cylindrical inner (IFC) and an outer (OFC) field cage with a high voltage membrane on one side, and a pad readout plane on the other side as shown on Figure (7.1). Some of the dimensions and characteristics of the HARP TPC are

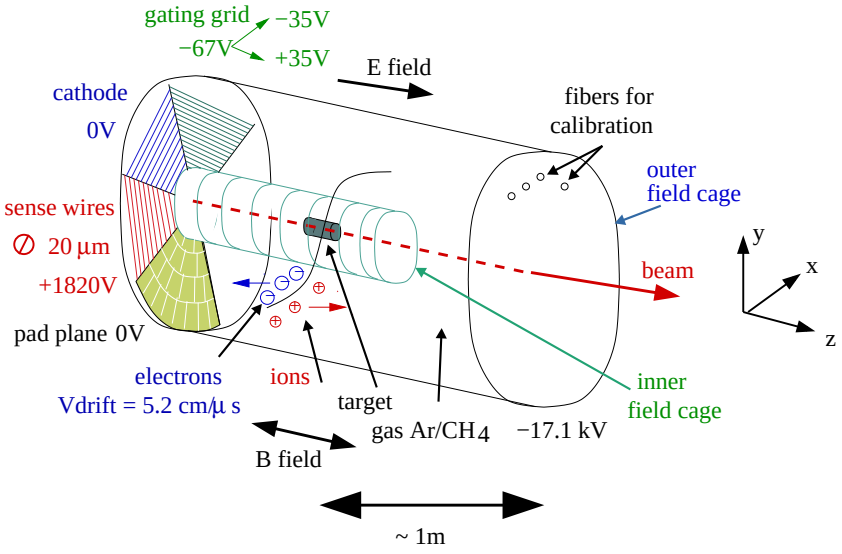

Figure 7.1: Schematic layout of the HARP time projection chamber

summarized in Table 7.1. The active volume is a cylinder of 41.6 cm radius and 154.1 cm length defined by the outer field cage. The insert which holds the target fits into the inner field cage which has a radius of 5.1 cm. Thus the TPC is blind to forward tracks segments inside a 5 cm radius. Beam particles entering in the TPC are focused at the target and produce secondaries that will ionize the 91% Argon and 9% methane gas mixture with an amount of $\sim$ 50 free electrons per cm for a minimum ionizing particle (primary ionization). The electrons then drift towards the anode wire plane in a homogeneous electric field of 111 V/cm with a velocity of approximately 5.17 cm/μs. The gas amplification at the anode wires is $\sim 2 \times 10^4$ inducing a signal onto the pad plane that will be recorded through the readout chain.

Item	Dimension/value
OFC inner diameter	816 mm
OFC outer diameter	832 mm
IFC inner diameter	102 mm
IFC outer diameter	106 mm
Anode wire (W + Au) diameter	20 μm
Anode wire pitch	4 mm
Distance between pad-plane and anode wires	5 mm
Cathode wire (Cu + Be) diameter	70 μm
Cathode wire pitch	2 mm
Distance between anode wires and cathode plane	5 mm
Gating grid wire (Cu + Be) diameter	70 μm
Gating grid wire pitch	4 mm wire pitch (each plane) effective pitch 2 mm
Distance between cathode plane and gating grid	6 mm

Table 7.1: Some dimensions and parameters of the HARP TPC

7.1 Field cages layout

The drift field is parallel to the cylinder axis, and extends from a thin membrane at the downstream end of the TPC, to the read-out chamber which operates at ground potential. The upstream drift direction is motivated by minimizing the material which is the way of secondary particles emanating from the target. Following the result of simulations [48] with the Maxwell software package for the electric field geometry and the Garfield package for the electron drift, the inner field cage (IFC) and the outer field cage (OFC) were both built with a double interleaved strip pattern. This pattern avoids electric field inhomogeneities and high field gradients, which would produce sparks or corona currents in the Ar-CH_4 mixture. A detailed description of the field cage layout is given in [49]. The OFC is closed at 1534 mm drift distance (from the gating-grid plane) by a 50 μm aluminised Mylar sheet held at a voltage of -17.1 kV. The IFC is closed at a 742 mm drift distance (from the gating-grid) by a 2 mm Stesalit® cap followed by a 50 μm aluminised Mylar sheet held at a voltage of -8.4 kV.

7.2 The readout planes

When the ionization electrons reach the readout chamber, they first encounter the gating grid consisting of two interleaved single-wire planes at a base voltage of -67 V and a sweep voltage of $\pm$ 35 V. The gate opens as soon it receives the trigger signal and remains opened during more than 30 μs for each event. The cathode plane is at 0 V potential and the anode plane at a voltage of +1820 V. They are each made of a single 150 m long wire strung onto an hexagonal frame. This provides equilibrium of wire-tension forces on both sides of the wire-support spokes which are of 6 mm width only, thus reducing considerably the dead space. The gas gain amplification at the anode wires induces a signal on the 6.5 mm $\times$ 15 mm pick-up pads. They are arranged in 20 circles of pads-rows distributed over six sectors of 662 pads each. In total the TPC has 3972 readout pads. Each sector is composed of a six-layer printed circuit board (PCB) with the pads on one side and the components on the other one. The pads are connected to quad pre-amplifiers/shapers. Kapton® flex connections, followed by buffer amplifiers and 6 m long picocoax cables drive the signal to

ADC cards.

7.3 The readout system

The ADC cards provide 10 MHz, 10-bit sampling and advanced sample selection (including a flexible number of pre- and post- samples). Three pedestals are taken at the beginning of each run and loaded into the ADC card memory. A threshold cut of 10 ADC counts above the pedestal is applied. Two pre- and post- samples below threshold are saved for each cluster-in-time. Data are saved in 10-bit words preceded by a 32-bit word header containing the pad information like its corresponding sector, row and number-in-row value. For physics events about 300 data samples are taken to cover the 30 μs total drift time of the TPC. The data size of an average physics event is approximately 45 kbytes of which 16 kbytes are occupied by header words. Each sector is read out by 14 ADC cards in one VME crate controlled by a single board computer compliant with VME-PCI transfers. The average readout time per sector amounts to 600 μs per physics event. Under normal running conditions, up to 500 events per spill could be collected.

7.4 TPC calibration systems

As the HARP TPC is used for particle identification purposes, it is important that the relative amplification factors for all pads are known. The design aim of the TPC was to achieve a $\Delta E/E$ resolution of about 10% for tracks using a truncated mean value for the pulse height measured in the 20 pads row. A Krypton calibration system was set up in order to measure the linearity of the analog pad readout. Unfortunately, due to a unexpected cross-talk feature inside the motherboard, the pad linearity could not be checked and a further Fe calibration was performed. The laser calibration system is aimed to provide drift velocity measurements as well as the reconstructed position in x-y of the laser fibres as cross-check of possible $\vec{E} \times \vec{B}$ effects.

7.4.1 Kr calibration system

The relative pulse height calibration of the pads is obtained by adding ^{83m}Kr gas to the TPC gas mixture during special calibration runs. By placing a ^{83}Rb source in the gas line entering the TPC we obtain ^{83m}Kr gas. The ^{83m}Kr isotope mainly decays in γ rays with a lifetime of 1.86 hours. Due to a high probability of internal conversion and Auger emission, most of the γ energy is transferred to electrons. Among the resulting clusters on the pad plane, those corresponding to the highest energy peak at 41 keV (see Figure 7.2) are selected by cutting on pad multiplicity, cluster shape and total cluster energy. The pad with the largest signal within a cluster is selected and a histogram per pad containing this value is filled over many events. The mean value of each of these histograms is used as multiplicative constant to equalize the pad response.

7.4.2 Laser calibration system

To measure the drift velocity and to allow for a systematic study of the electron drift in the TPC volume a laser calibration system was installed. A KrF laser produces 248 nm wave-length light that excites the Al end-face of 192, 200 μm diameter optical glass fibres, distributed over the surface of the high voltage end-plate. As a result, electrons are released in the TPC in well-defined positions in space and time. By measuring the time between the laser pulse and the arrival of the electron near the pad-plane, one can

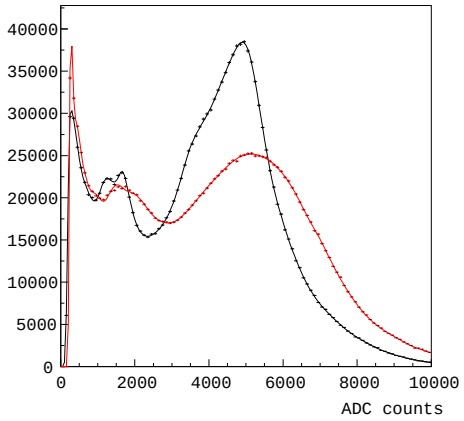

Figure 7.2: ^{83m}Kr spectrum before (red curve) and after (black curve) pad equalization

monitor the drift velocity permanently [50]. The laser is fired two-three times per run. The laser data also provide input for other systematic studies, like possible $\vec{E} \times \vec{B}$ effects, of the TPC performance.

7.5 Systematic effects

7.5.1 Electric field non uniformity

The positive potential of the anode wires causes the effective potential at the position of the cathode wires to be positive rather than equal to zero. Therefore, the 'virtual ground' is located several millimeters downstream of the cathode wire plane. This mismatch between the position of the virtual ground and the potential imposed by the potential rings creates small transverse electric field components which in turn lead to tracks distortions.
At the end of the data taking by performing a measurement of the voltage on the strips of the IFC, we discovered a discontinuity in the degrading of the electric field. The downstream end of the IFC was accidentally different by about 2% from the high voltage value on the OFC at the same z position. This effect causes also unwanted electric field components associated again with track distortions. An evaluation of the voltage misalignement has been performed at the end of the year 2003, reconstructing the two track segments of cosmics events crossing the TPC center for different values of the voltage applied on the IFC. It helped to build up an algorithm that will correct for the distortion effects.

7.5.2 Cross-talk

During 2001 data-taking period cross-talk between pads was discovered. The effect appears mainly to be due to pre-amplifier signal output lines passing in the proximity of other pads and creating noise signals into it. This is due to a capacitive coupling between the input of one pre-amplifier and the output of another pre-amplifier. Systematic checks on a spare PCB and on the six TPC sectors have been performed during a cross-talk measurement campaign in winter 2002-2003. By injecting a pulser signal into each individual pad different types of cross-talk (self-cross talk, and pad-to-pad relationship) [50] have been sorted out. The induced signal is generally less than 10% of the seed signal, amplitude-inverted and time-delayed. The cross-talk effect has been measured precisely by injecting signals with three different fixed amplitudes into each individual pad. The subsequent signals recorded in the excited pads as well as in the pads located in

its vicinity provide input for a deconvoluting correction matrix. Cross-talk model and deconvolution matrix as well as a full simulation of the TPC behaviour with and without cross-talk have been carried out and results have been reported in [26].

7.6 Track reconstruction

7.6.1 Calibration of the TPC raw data

In order to correct the TPC sampling time from the jitter, electronics modules and cable delay, for each event we save into a time to digital converter (TDC) module the value t_{IN} and t_{OUT}. t_{IN} is taken somewhere in the TPC readout modules chain and contains the time when the physics trigger is produced by the trigger electronics. t_{OUT} is measured at the output of the sector 5 clock card and contains the time value of the trigger after alignment on the clock signal. Given the cable length, module ordering and the fact that we introduced a physical delay of approximately 3 μs between the physics trigger and the signal sent to the TPC to eliminate unwanted record of pulses induced by the gating grid signal, the difference between t_{OUT} and t_{IN} (in ns) is equal to:

$$t_{OUT} - t_{IN} = t_{jitter} + t_D + 3419$$

where t_{jitter} is the jitter introduced by the clock-trigger alignment. It is comprised between 0 and 100 ns. The time t_D is the delay introduced by one of our discriminator, its nominal value is 7.5 ns. The sampling time for ADC cards, in order to be compared to physics trigger time should be corrected as follows (in ns):

$$t_{corrected} = t_{samples} - 1600 + t_1 + t_{OUT} - t_{IN} + t_D - 208$$

with t_1 being the signal output time from a known logic fan in/out module of our TPC readout chain. The 1600 ns correction comes from a fixed pre-sampling feature of our ADC cards which can record up to 16 samples before the trigger. Since these samples belong to the signal coming from the gating grid they are not recorded but the relative time recorded needs to be shifted back to the arrival time of the trigger. The remaining 208 ns correspond to some remaining cables and modules that we have to take into account for the exact time calibration. For the time being in the TPC algorithms that calibrate the time we only correct as follows:

$$t_{calib} = t_{samples} - 1600 + t_{OUT} - t_{IN}$$

This would shift upstream the calculated z position 1 μs order, but to apply a more refined correction, we have also to check the time found for an interaction at a known z position that can be for instance the Stesalit® membrane of the IFC.
Pedestal subtraction is done the following way. For each run, at the beginning of the run three pedestals events are taken with a threshold set at zero. Each pedestal event is then unpacked and for each pad the ADC value of each pad with the sampling time t comprised between 10 μs and 25 μs is saved. This cut on time has been chosen to compute the pedestals outside the gating grid signal and in the physics data window. The pedestal P_{ADC} and the standard deviation σ values are computed:

$$P_{ADC} = \frac{\sum_i ADC_i}{N}$$

with N being the total number of ADC counts comprised between 10 μs and 25 μs.

$$\sigma = \sqrt{\frac{\sum ADC_i^2}{N} - P_{ADC}^2}$$

Sector	Number of masked pads
1	6
2	0
3	1
4	12
5	5
6	8

Table 7.2: Number of channel masked per sector during 2002 data taking

The pedestal value is then loaded in a register of the front-end electronics and all events of the run following the last pedestal event have their pedestal values subtracted from the ADC amplitudes before the packing, as described above. The standard deviation has been used to tag noisy or dead pads. For 2001 data taking, pedestal events were not saved. For 2002 they are saved as CALIBRATION events. The last pedestal event contains also at the end of its trailer some information about the configuration of the ADC registers. For 2002 data taking it has been decided to mask some TPC pads which were considered as noisy or broken. The criteria to mask a channel was based on pedestal data. Once masked the TPC data from these channels are not saved anymore in the database and a mask value contained in the mapping files just specifies the type of problem of the given pads. Five different behaviours have been flagged during 2002 data taking, after the repair of some of the oscillating channels discovered in 2001. The corresponding mask values are :

1. 101 Oscillation
2. 102 large and flat value of the pedestal
3. 103 Noisy channel
4. 104 Full oscillation
5. 105 Daughter card problem (large pedestals)

A text file summarizes all TPC channels masked with the masking date. It helps to follow the masking progress and permits to treat clusters containing a masked pad differently since the cluster resolution will be different in this case. The number of pads masked per sector for 2002 data taking is given in Table 7.2. It represents less than 1% of the total number of pads. In addition, for each sector 10 channels are masked to mask value 1. They correspond to non-physical pads, therefore they don't need to be saved in our database.

7.6.2 Space clusters building

In order to reconstruct tracks, one looks for clusters in the individual pad-rows [51]. Clusters-in-time of individual pad hits are considered. These are given a reference time defined by the raising edge of the signal at the time when the pulse has reached 50% of its peak value. Hits in neighbouring pads (along the same row) with time stamps that differ less than 500 ns are attached to the cluster formed within the pad row. A weighted position in r-ϕ direction along the pad-row and in z direction is then assigned.

7.6.3 Pattern recognition

A pattern recognition algorithm loops over all the clusters found and will connect them in order to define a track candidate. The algorithm which does the computation is not assuming the helicoidal shape of the

tracks. It establishes first links between points. As the tracks are supposed to be less dense in the outer region of the TPC, the search for clusters to be added to these links starts using the links of the outer region as seeds. The line connecting the first two points is followed towards the detector axis. When a cluster is located in the volume of a truncated cone with the axis along this line, it is added to the track candidate. The parameters of the cone like the radius or the opening angle are driving the forward acceptance. Therefore they have been optimized to achieve a maximum track finding efficiency for particles with momenta above 100 MeV/c.

7.6.4 Helix tracks fit

For each track candidate a track fit is performed. Is has been computed from the code used for the ALEPH TPC track fit [52]. Cosmic rays were used, as a first check of the quality of the track reconstruction. The RPC barrel detector provides the trigger for cosmic rays that cross the TPC in the transverse direction. Such a cosmic ray will be identified by two tracks segments in opposite TPC sectors. By comparison of the parameters of the fit for the two track segments, information about the angular resolution of the tracks has been obtained. The track direction of the two segments matches in r-ϕ within $\sigma = 0.07$ rad. The dip angle with respect to the z axis coincides within $\sigma = 0.02$ rad. Track residuals have been measured and fitted to a double Gaussian distribution with $\sigma = 1.6$ mm in r-ϕ direction and $\sigma = 3$ mm in the z direction in absence of cross-talk correction.

7.6.5 Kalman track fit

The parameters of the helix computed by the helix track fit algorithm are used as seed parameters in a algorithm which will introduce (using the Kalman package) multiple-scattering and energy loss effects and will refit the helix parameters.

Part IV

Vertex finding in the HARP experiment

Chapter 8

Kalman filter for vertex fit

8.1 Introduction

The behaviour of a dynamic system can be described by the evolution of a set of variables called state variables. In practice, these state variables cannot be determined exactly by direct measurements. Instead, the measurements we make are functions of the state variables and they are affected by random noise. The Kalman filter is a set of mathematical equations that provides an efficient recursive computational solution of the least-square method. Filtering permits the estimation of a result at a given measurement point based on previous measurements. Smoothing will help to re-estimate a previous result from the results of measurements included after.

8.2 Vertex evaluation

A vertex fit serves mainly two purposes:

1. The estimation of the position of the interaction point and of the momentum vector of the tracks emerging from this point.

2. A check of the association of a track to a vertex and decision whether the track does indeed originate from this vertex.

In case of a possible secondary vertex (such as that of a K_S^0 or Λ^0), the exact position of the primary vertex is of some importance since it determines the direction of the possibly unseen track connecting the two vertices. In both cases, the momentum vector of all emerging tracks should be computed with the best possible precision, including their covariance matrix since they are the input to a subsequent kinematical fit. The advantages of the Kalman technique for a vertex fit are:

- It takes into account processes like multiple scattering and energy loss.

- The algorithm is fast.

- Filtering and smoothing allows to connect the result of a subsequent iteration with the previous result and correct it

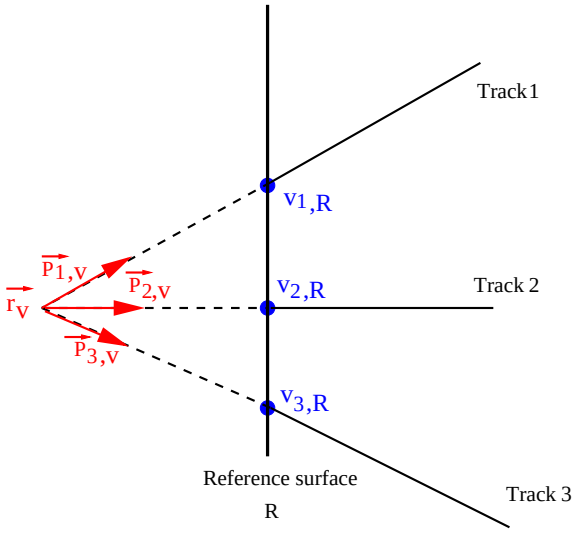

Figure 8.1: System of n tracks for a vertex fit

8.3 Description of a system of n tracks

Assuming that, at a reference surface R (see Fig. 8.1), we have n tracks with the fitted track parameters $\mathbf{v_{k,R}}$ and the corresponding weight matrices $\mathbf{G_k} = \mathbf{V_k^{-1}}$, $\mathbf{V_k} = \mathrm{cov}(\epsilon_k)$ with k running from 1 to n and ϵ_k being the measurement errors of the fitted track parameters. $\mathbf{v_{k,R}}$ and $\mathbf{G_k}$ are regarded as virtual measurements that can be used to find an estimate of the vertex position $\vec{r}_V$ and of the momentum vector $\vec{p}_{k,V}$ of track k at the vertex. Prior information about the vertex position can be included via a vector $\vec{r}^{\,0}_V$ and its covariance matrix $\mathbf{C_0} = \mathrm{cov}(\vec{r}^{\,0}_V)$. The measurement equation is normally non-linear and can be written as:

$$\mathbf{v_{k,R}} = \mathbf{h_k}(\vec{r}_{\mathbf{V}}, \vec{p}_{\mathbf{k,V}}) + \epsilon_{\mathbf{k}} \tag{8.1}$$

The system can be linearized at a given point $(\vec{r}_0, \vec{p}_{k,0})$ by a first order Taylor expansion as follows:

$$\begin{aligned} \mathbf{h_k}(\vec{r}_{\mathbf{V}}, \vec{p}_{\mathbf{k,V}}) &= \mathbf{h_k}(\vec{r}_{\mathbf{0}}, \vec{p}_{\mathbf{k,0}}) + \mathbf{A_k} \cdot (\vec{r}_{\mathbf{V}} - \vec{r}_{\mathbf{0}}) + \mathbf{B_k} \cdot (\vec{p}_{\mathbf{k,V}} - \vec{p}_{\mathbf{k,0}}) + \mathbf{R} & (8.2)\\ &= \mathbf{c_{k,0}} + \mathbf{A_k} \cdot \vec{r}_{\mathbf{V}} + \mathbf{B_k} \cdot \vec{p}_{\mathbf{k,V}} + \mathbf{R} & (8.3) \end{aligned}$$

with:

$$\begin{aligned} \mathbf{c_{k,0}} &= \mathbf{h_k}(\vec{r}_{\mathbf{0}}, \vec{p}_{\mathbf{k,0}}) - \mathbf{A_k} \cdot \vec{r}_{\mathbf{0}} - \mathbf{B_k} \cdot \vec{p}_{\mathbf{k,0}} \\ \mathbf{A_k} &= \left(\frac{\partial \mathbf{h_k}}{\partial \vec{r}_V}\right)_{(\vec{r}_0, \vec{p}_{k,0})} \\ \mathbf{B_k} &= \left(\frac{\partial \mathbf{h_k}}{\partial \vec{p}_{k,V}}\right)_{(\vec{r}_0, \vec{p}_{k,0})} \end{aligned}$$

A vector of dimension 5 is sufficient to describe all the necessary information about track position and momentum at the reference surface R, therefore $\mathbf{v_{k,R}}$ is in the general case of dimension 5. From (8.1) and

(8.3) we can write down the linear description of the system as follows:

$$\begin{pmatrix} \overrightarrow{r}^{\,0}_{V} \\ \mathbf{v_{1,R}} - \mathbf{c_{1,0}} \\ \cdots \\ \vdots \\ \mathbf{v_{n,R}} - \mathbf{c_{n,0}} \end{pmatrix} \simeq \begin{pmatrix} \mathbf{I} & 0 & \dots & \dots & 0 \\ \mathbf{A_1} & \mathbf{B_1} & 0 & \dots & 0 \\ \cdots & 0 & \mathbf{B_2} & \dots & 0 \\ \vdots & \vdots & \vdots & \ddots & \vdots \\ \mathbf{A_n} & 0 & 0 & \dots & \mathbf{B_n} \end{pmatrix} \cdot \begin{pmatrix} \overrightarrow{r}_{V} \\ \overrightarrow{p}_{1,V} \\ \cdots \\ \vdots \\ \overrightarrow{p}_{2,V} \end{pmatrix} + \begin{pmatrix} \epsilon_0 \\ \epsilon_1 \\ \cdots \\ \vdots \\ \epsilon_n \end{pmatrix} \tag{8.4}$$

The measurement errors ϵ_k can be assumed to be independent, their joint covariance matrix is therefore block diagonal. This system is equivalent to the following equation:

$$\mathbf{M} \cdot \mathbf{x} = \mathbf{b}$$

With $\mathbf{M}$ being the (5n+3)×(3n+3) matrix of equation (8.4), $\mathbf{x}$ the (3n+3) vector of estimate parameters $\overrightarrow{r}_V$ and $\overrightarrow{p}_{k,V}$ we would like to determine, and $\mathbf{b}$ the (5n+3) vector:

$$\mathbf{b} = \begin{pmatrix} \overrightarrow{r}^{\,0}_{V} - \epsilon_0 \\ \mathbf{v_{1,R}} - \mathbf{c_{1,0}} - \epsilon_1 \\ \vdots \\ \mathbf{v_{n,R}} - \mathbf{c_{n,0}} - \epsilon_n \end{pmatrix}$$

A solution to (8.4) can then be found with the least-squares method by solving the following equation:

$$\mathbf{M^T} \cdot \mathbf{M} \cdot \mathbf{x} \;=\; \mathbf{M^T} \cdot \mathbf{b}$$

Which leads to the following :

$$\mathbf{x} \;=\; \mathbf{N^{-1}} \cdot \mathbf{M^T} \cdot \mathbf{b}$$

With $\mathbf{N}$ being the (3n+3)×(3n+3) product $\mathbf{M^T} \cdot \mathbf{M}$ and $\mathbf{M^T}$ the (3n+3)×(5n+3) transposed $\mathbf{M}$ matrix. Both $\mathbf{N}$ and $\mathbf{M^T}$ contains $\mathbf{A_k}$ and $\mathbf{B_k}$ matrices. In fact the covariance matrix of the estimate is $\mathbf{N^{-1}}$ and the number of operations required for a straightforward inversion is proportional to n^3. Indeed $\mathbf{N}$ is a positive-defined symmetric matrix, therefore it can be decomposed into Cholesky matrices with $\mathbf{N} = \mathbf{L} \cdot \mathbf{L^T}$ which would require a number of operations equivalent to $(3n+3)^3$. Since we don't need to know the complete evaluation of $\mathbf{N}$ to calculate the fitted parameters $\overrightarrow{r}_V$ and $\overrightarrow{p}_{k,V}$, it has been demonstrated [53] that the computational cost to get the fitted vertex parameters and respective covariance matrices could be reduced to an order of n^2 by rewriting the matrix $\mathbf{N}$ in a simplest way. Nevertheless, even if this method is much faster than a conventional least-squares method it is still problematic as soon as one wants to use it on different subsets of tracks since one wants to remove or add a track during the fitting procedure. This would lead to a very low performance if one needs to compute repeated applications of the global fit. This is why an iterative procedure of track association to a vertex can be set up with a Kalman method for the vertex fit.

8.3.1 Equations of the Kalman filter for vertex fit

Thanks to the block structure of the model matrix of equation (8.4), the vertex fit using the global fit method can be considered as a special case of the extended Kalman filter with a variable dimension ($3n$+3) of the state vector ($\overrightarrow{r}_V, \overrightarrow{p}_{1,V}, \cdots, \overrightarrow{p}_{n,V}$). Initially the state vector consists only of the prior information about the vertex position $\overrightarrow{r}_V^0$ and its covariance matrix $\mathbf{C_0}$. The Kalman filter describes how to add a new track k with track parameter $\mathbf{v_{k,R}}$ to a vertex already fitted with k-1 tracks. At the same time it provides an estimate of the momentum vector $\overrightarrow{p}_{k,V}$ of track k at the vertex. The system equation of the filter is:

$$\overrightarrow{r}_{k,V} = \overrightarrow{r}_{k-1,V}$$

The measurement equation is given by:

$$\mathbf{v_{k,R}} = \mathbf{h_k}(\overrightarrow{r}_{\mathbf{k,V}}, \overrightarrow{p}_{\mathbf{k,V}}) + \epsilon_\mathbf{k}$$

A Taylor expansion at first order at the point $(\overrightarrow{r}_{k,0}, \overrightarrow{p}_{k,0})$ would then give:

$$\begin{aligned} \mathbf{h_k}(\overrightarrow{r}_{\mathbf{k,V}}, \overrightarrow{p}_{\mathbf{k,V}}) &\simeq \mathbf{h_k}(\overrightarrow{r}_{\mathbf{k,0}}, \overrightarrow{p}_{\mathbf{k,0}}) + \mathbf{A_k} \cdot (\overrightarrow{r}_{\mathbf{k,V}} - \overrightarrow{r}_{\mathbf{k,0}}) + \mathbf{B_k} \cdot (\overrightarrow{p}_{\mathbf{k,V}} - \overrightarrow{p}_{\mathbf{k,0}}) \\ &\simeq \mathbf{c_{k,0}} + \mathbf{A_k} \cdot \overrightarrow{r}_{\mathbf{k,V}} + \mathbf{B_k} \cdot \overrightarrow{p}_{\mathbf{k,V}} \end{aligned}$$

with:

$$\begin{aligned} \mathbf{c_{k,0}} &= \mathbf{h_k}(\overrightarrow{r}_{\mathbf{k,0}}, \overrightarrow{p}_{\mathbf{k,0}}) - \mathbf{A_k} \cdot \overrightarrow{r}_{\mathbf{k,0}} - \mathbf{B_k} \cdot \overrightarrow{p}_{\mathbf{k,0}} \\ \mathbf{A_k} &= \left(\frac{\partial \mathbf{h_k}}{\partial \overrightarrow{r}_{k,V}}\right)_{(\overrightarrow{r}_{k,0}, \overrightarrow{p}_{k,0})} \\ \mathbf{B_k} &= \left(\frac{\partial \mathbf{h_k}}{\partial \overrightarrow{p}_{k,V}}\right)_{(\overrightarrow{r}_{k,0}, \overrightarrow{p}_{k,0})} \end{aligned}$$

If we have a good knowledge of the vertex position the expansion point $\overrightarrow{r}_{k,0}$ can be the same for all tracks just as in the global fit method. The updated estimates for the filter part are [54]:

$$\begin{aligned} \overrightarrow{r}_{k,V} &= \mathbf{C_k} \cdot [\mathbf{C_{k-1}^{-1}} \cdot \overrightarrow{r}_{\mathbf{k-1,V}} + \mathbf{A_k^T} \cdot \mathbf{G_k^B} \cdot (\mathbf{v_{k,R}} - \mathbf{c_{k,0}})] \\ \overrightarrow{p}_{k,V} &= \mathbf{S_k} \cdot \mathbf{B_k^T} \cdot \mathbf{G_k} \cdot (\mathbf{v_{k,R}} - \mathbf{c_{k,0}} - \mathbf{A_k} \cdot \overrightarrow{r}_{\mathbf{k,V}}) \\ \mathbf{C_k} &= cov(\overrightarrow{r}_{k,V}) = (\mathbf{C_{k-1}^{-1}} + \mathbf{A_k^T} \cdot \mathbf{G_k^B} \cdot \mathbf{A_k})^{-1} \\ \mathbf{D_k} &= cov(\overrightarrow{p}_{k,V}) = \mathbf{S_k} + \mathbf{E_k^T} \cdot \mathbf{C_k^{-1}} \cdot \mathbf{E_k} \\ \mathbf{E_k^T} &= cov(\overrightarrow{r}_{k,V}, \overrightarrow{p}_{k,V}) = -\mathbf{S_k} \cdot \mathbf{B_k^T} \cdot \mathbf{G_k} \cdot \mathbf{A_k} \cdot \mathbf{C_k} \end{aligned} \tag{8.5}$$

With

$$\begin{aligned} \mathbf{S_k} &= (\mathbf{B_k^T} \cdot \mathbf{G_k} \cdot \mathbf{B_k})^{-1} \\ \mathbf{G_k^B} &= \mathbf{G_k} - \mathbf{G_k} \cdot \mathbf{B_k} \cdot \mathbf{S_k} \cdot \mathbf{B_k^T} \cdot \mathbf{G_k} \end{aligned}$$

The χ^2 of the filter at step k has two degrees of freedom and is given by:

$$\begin{aligned} \chi^2_{k,F} &= (\overrightarrow{r}_{k,V} - \overrightarrow{r}_{k-1,V})^T \cdot \mathbf{C_{k-1}^{-1}} \cdot (\overrightarrow{r}_{\mathbf{k,V}} - \overrightarrow{r}_{\mathbf{k-1,V}}) + \mathbf{r_k^T} \cdot \mathbf{G_k} \cdot \mathbf{r_k} \\ \mathbf{r_k} &= \mathbf{v_{k,R}} - \mathbf{c_{k,0}} - \mathbf{A_k} \cdot \overrightarrow{r}_{\mathbf{k,V}} - \mathbf{B_k} \cdot \overrightarrow{p}_{\mathbf{k,V}} \end{aligned}$$

The total χ^2 of the filter part is a sum of independent random variables and defined as follows at step k:

$$\chi^2_k(filter) = \chi^2_{k-1}(filter) + \chi^2_{k,F} \tag{8.6}$$

Its value at the end of the filter part will help to estimate the goodness of the fit. A good fit at the end of the filter stage should provide a χ^2 distribution which mean value is set at the number of degrees of freedom and the variance σ should be equal to $2 \cdot n$. In our case n is equal to the number of tracks included in the fit. Also at filter stage outliers can be detected by looking at the intermediate $\chi^2_{k,F}$ but we have to be aware of the fact that this test is not symmetric since track k is tested against a vertex fitted from k-1 tracks. Therefore the resulting $\chi^2_{k,F}$ will be dependent of the order in which the tracks are attached to the vertex. It is possible to repeat the linear expansion in the new point:

$$\begin{aligned} \overrightarrow{r}_{k,0} &= \overrightarrow{r}_{k,V} \\ \overrightarrow{p}_{k,0} &= \overrightarrow{p}_{k,V} \end{aligned}$$

and recompute the filter until there is no significant change either in the χ^2 or in the estimate. The smoother part runs from track n to 1 in order to pass back the final information about vertex position and track momentum to all the previous estimates and update the corresponding filtered covariance matrix. The updated estimates for the smoother part are :

$$\begin{aligned} \overrightarrow{r}^{\,n}_{k,V} &= \overrightarrow{r}_{n,V} \\ \overrightarrow{p}^{\,n}_{k,V} &= \mathbf{S_k} \cdot \mathbf{B_k^T} \cdot \mathbf{G_k} \cdot (\mathbf{v_{k,R}} - \mathbf{c_{k,0}} - \mathbf{A_k} \cdot \overrightarrow{r}_{\mathbf{n,V}}) \\ \mathbf{C^n_k} &= \mathbf{C_n} \\ \mathbf{D^n_{ik}} &= \delta_{ik} \cdot \mathbf{S_k} + \mathbf{S_i} \cdot \mathbf{B_i^T} \cdot \mathbf{G_i} \cdot \mathbf{A_i} \cdot \mathbf{C_n} \cdot \mathbf{A_k^T} \cdot \mathbf{G_k} \cdot \mathbf{B_k} \cdot \mathbf{S_k} = \mathbf{cov}(\overrightarrow{p}^{\,\mathbf{n}}_{\mathbf{i,V}}, \overrightarrow{p}^{\,\mathbf{n}}_{\mathbf{k,V}}) \\ \mathbf{E^{nT}_k} &= cov(\overrightarrow{r}^{\,n}_{k,V}, \overrightarrow{p}^{\,n}_{k,V}) = \mathbf{-S_k} \cdot \mathbf{B_k^T} \cdot \mathbf{G_k} \cdot \mathbf{A_k} \cdot \mathbf{C_n} \end{aligned} \tag{8.7}$$

Where $\overrightarrow{r}^{\,n}_{k,V}$ means the estimate of $\overrightarrow{r}_{k,V}$ using measurements up to track n and i run from index k to n. The χ^2 of the smoother at step k has two degrees of freedom and is given by:

$$\chi^2_{k,S} = (\overrightarrow{r}^{\,n}_{k,V} - \overrightarrow{r}^{\,n*}_{k,V})^T \cdot (\mathbf{C^{n*}_k})^{-1} \cdot (\overrightarrow{r}^{\,\mathbf{n}}_{\mathbf{k,V}} - \overrightarrow{r}^{\,\mathbf{n*}}_{\mathbf{k,V}}) + \mathbf{r^{nT}_k} \cdot \mathbf{G_k} \cdot \mathbf{r^n_k} \tag{8.8}$$

$$\mathbf{r^n_k} = \mathbf{v_{k,R}} - \mathbf{c_{k,0}} - \mathbf{A_k} \cdot \overrightarrow{r}^{\,\mathbf{n}}_{\mathbf{k,V}} - \mathbf{B_k} \cdot \overrightarrow{p}^{\,\mathbf{n}}_{\mathbf{k,V}} \tag{8.9}$$

where $\overrightarrow{r}^{\,n*}_{k,V}$ is the smoothed estimate $\overrightarrow{r}^{\,n}_{k,V}$ with the track $\mathbf{v_{k,R}}$ removed. It is obtained by the inverse Kalman filter:

$$\begin{aligned} \mathbf{C^{n*}_k} &= (\mathbf{C_n^{-1}} - \mathbf{A_k^T} \cdot \mathbf{G_k^B} \cdot \mathbf{A_k})^{-1} \\ \overrightarrow{r}^{\,n*}_{k,V} &= \mathbf{C^{n*}_k} \cdot [\mathbf{C_n^{-1}} \cdot \overrightarrow{r}^{\,\mathbf{n}}_{\mathbf{k,V}} - \mathbf{A_k^T} \cdot \mathbf{G_k^B} \cdot (\mathbf{v_{k,R}} - \mathbf{c_{k,0}})] \end{aligned}$$

By identity with the definition given for the total χ^2 of the filter part, the total χ^2 of the smoother part is equal to:

$$\chi^2_k(smoother) = \chi^2_{k,S} + \chi^2_{k+1}(smoother) \tag{8.10}$$

If the final vertex position is significantly different from the original one, $\mathbf{A_k}$ and $\mathbf{B_k}$ need to be recomputed. The cost of computing the estimates and their respective marginal covariance matrices is proportional to n. The remaining elements of the full covariance matrix can be calculated with $\mathcal{O}(n^2)$ additional operations.

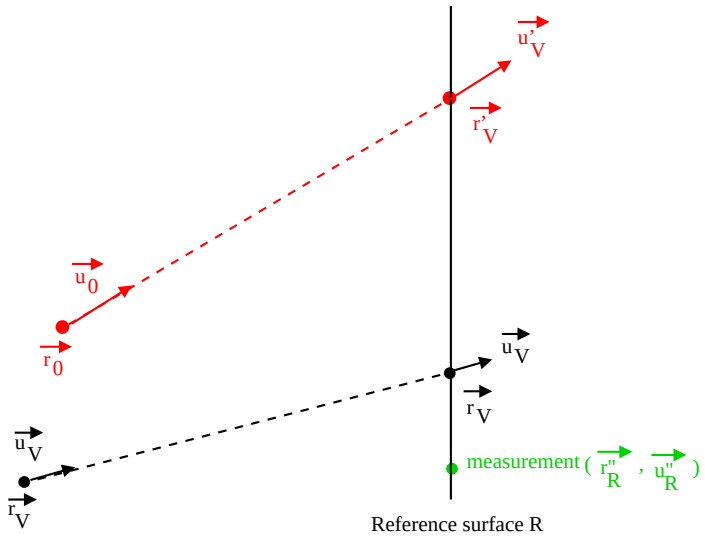

Figure 8.2: Straight line model

8.3.2 Straight line model

For simplicity and to test our algorithm performance we have chosen to describe the system using as track model a straight line. In the HARP Reconstruction framework this means simply that from the reference surface R, to the vertex point, tracks will be approximated as straight line to compute the vertex fit. We have chosen the $\mathbf{v_{k,R}}$ vector as a dimension 6 vector of the position $\overrightarrow{r}_{k,R}$ and the momentum $\overrightarrow{p}_{k,R}$ of track k calculated at the reference surface R. For a given track (see Fig. 8.2) we have the following parameters:

- the measurement of the track at the reference surface R given by its position $\overrightarrow{r}''_R$ and its normalized momentum $\overrightarrow{u}''_R$.
- the vertex position $\overrightarrow{r}_V$ and the normalized momentum at vertex $\overrightarrow{u}_V$.
- the extrapolation of the track from the vertex point to the reference surface given by the position $\overrightarrow{r}_R$ and the normalized momentum $\overrightarrow{u}_R$.
- the expansion point position $\overrightarrow{r}_0$ and normalized momentum $\overrightarrow{u}_0$.
- the extrapolation of the track from the expansion point to the reference surface given by the position $\overrightarrow{r}'_R$ and the normalized momentum $\overrightarrow{u}'_R$.

The following identities are straightforward:

$$\begin{aligned}
\overrightarrow{r}_R &= \overrightarrow{r}_V + S_{VR} \cdot \overrightarrow{u}_V \\
\overrightarrow{p}_R &= \overrightarrow{p}_V \\
S_{VR} &= \frac{(\overrightarrow{r}_R - \overrightarrow{r}_V) \cdot \overrightarrow{n}}{\overrightarrow{u}_V \cdot \overrightarrow{n}} \\
\overrightarrow{u}_V &= \frac{\overrightarrow{p}_V}{\|\overrightarrow{p}_V\|} \\
\overrightarrow{u}_R &= \frac{\overrightarrow{p}_R}{\|\overrightarrow{p}_R\|}
\end{aligned}$$

S_{VR} is the path length between the vertex position and $\overrightarrow{r}_R$ and $\overrightarrow{n}$ the normal vector to the reference surface at this position. The same for:

$$\begin{aligned}
\overrightarrow{r}'_R &= \overrightarrow{r}_0 + S_{0R} \cdot \overrightarrow{u}_0 \\
\overrightarrow{p}'_R &= \overrightarrow{p}_0 \\
S_{0R} &= \frac{(\overrightarrow{r}'_R - \overrightarrow{r}_0) \cdot \overrightarrow{n'}}{\overrightarrow{u}_0 \cdot \overrightarrow{n'}} \\
\overrightarrow{u}_0 &= \frac{\overrightarrow{p}_0}{\|\overrightarrow{p}_0\|} \\
\overrightarrow{u}'_R &= \frac{\overrightarrow{p}'_R}{\|\overrightarrow{p}'_R\|}
\end{aligned}$$

S_{0R} being the path length between the expansion point position and $\overrightarrow{r}'_R$ and $\overrightarrow{n'}$ the normal vector to the reference surface at this position. The two functions $\mathbf{h}$ are equal to:

$$\begin{aligned}
\mathbf{h}(\overrightarrow{r}_\mathbf{V}, \overrightarrow{p}_\mathbf{V}) &= \mathbf{v_R} - \epsilon = \begin{pmatrix} \overrightarrow{r}_R \\ \overrightarrow{p}_R \end{pmatrix} - \epsilon \\
\mathbf{h}(\overrightarrow{r}_\mathbf{0}, \overrightarrow{p}_\mathbf{0}) &= \mathbf{v'_R} - \epsilon' = \begin{pmatrix} \overrightarrow{r}'_R \\ \overrightarrow{p}'_R \end{pmatrix} - \epsilon'
\end{aligned}$$

where ϵ and ϵ' are the corresponding errors on the measurements. The matrix $\mathbf{A}$ and $\mathbf{B}$ can be separated in two (3×3) blocks as follows:

$$\mathbf{A} = \begin{pmatrix} \mathbf{A_1} \\ \mathbf{A_2} \end{pmatrix} = \begin{pmatrix} \frac{\partial \overrightarrow{r}_R}{\partial \overrightarrow{r}_V} \\ \frac{\partial \overrightarrow{p}_R}{\partial \overrightarrow{r}_V} \end{pmatrix} |_{(\overrightarrow{r}_0, \overrightarrow{p}_0)}$$

And

$$\mathbf{B} = \begin{pmatrix} \mathbf{B_1} \\ \mathbf{B_2} \end{pmatrix} = \begin{pmatrix} \frac{\partial \overrightarrow{r}_R}{\partial \overrightarrow{p}_V} \\ \frac{\partial \overrightarrow{p}_R}{\partial \overrightarrow{p}_V} \end{pmatrix} |_{(\overrightarrow{r}_0, \overrightarrow{p}_0)}$$

This gives for $\mathbf{A}$:

$$\begin{aligned} A_1^{ij} &= \frac{\partial}{\partial r_V^j}(r_V^i - S_{VR}\cdot u_V^i)\mid_{(\vec{r}_0,\vec{p}_0)} \\ &= \delta_{ij} + \frac{\partial S_{VR}}{\partial r_V^j}\cdot u_V^i + S_{VR}\cdot\frac{\partial u_V^i}{\partial r_V^j}\mid_{(\vec{r}_0,\vec{p}_0)} \\ &= \delta_{ij} - \frac{n^j\cdot u_V^i}{(\vec{u}_V\cdot\vec{n})}\mid_{(\vec{r}_0,\vec{p}_0)} \\ &= \delta_{ij} - \frac{n^j\cdot u_0^i}{(\vec{u}_0\cdot\vec{n})} \end{aligned}$$

and:

$$\begin{aligned} A_2^{ij} &= \frac{\partial}{\partial r_V^j}(p_V^i)\mid_{(\vec{r}_0,\vec{p}_0)} \\ &= 0 \end{aligned}$$

For the matrix $\mathbf{B}$ we get:

$$\begin{aligned} B_1^{ij} &= \frac{\partial}{\partial p_V^j}(r_V^i - S_{VR}\cdot u_V^i)\mid_{(\vec{r}_0,\vec{p}_0)} \\ &= \frac{\partial S_{VR}}{\partial p_V^j}\cdot u_V^i + S_{VR}\cdot\frac{\partial u_V^i}{\partial p_V^j}\mid_{(\vec{r}_0,\vec{p}_0)} \\ &= -\frac{S_{VR}\cdot n^j\cdot u_V^i}{(\vec{u}_V\cdot\vec{n})\cdot\|\vec{p}_V\|} + \frac{S_{VR}\cdot\delta_{ij}}{\|\vec{p}_V\|}\mid_{(\vec{r}_0,\vec{p}_0)} \\ &= \frac{S_{0R}}{\|\vec{p}_0\|}\Big(\delta_{ij} - \frac{n^j\cdot u_0^i}{(\vec{u}_0\cdot\vec{n})}\Big) \end{aligned}$$

and:

$$\begin{aligned} B_2^{ij} &= \frac{\partial}{\partial p_V^j}(p_V^i)\mid_{(\vec{r}_0,\vec{p}_0)} \\ &= \delta_{ij} \end{aligned}$$

For the $\mathbf{c_0}$ vector we can also split it into:

$$\mathbf{c_0} = \begin{pmatrix} \mathbf{c_{0,1}} \\ \mathbf{c_{0,2}} \end{pmatrix} = \begin{pmatrix} \vec{r}\,'_R - \mathbf{A_1}\cdot\vec{r}_\mathbf{0} - \mathbf{B_1}\cdot\vec{p}_\mathbf{0} \\ \vec{p}\,'_R - \mathbf{A_2}\cdot\vec{r}_\mathbf{0} - \mathbf{B_2}\cdot\vec{p}_\mathbf{0} \end{pmatrix}$$

This leads to:

$$\begin{aligned} c_{0,1}^i &= r_0^i + S_{0R}\cdot u_0^i - \sum_{j=1}^{3} A_1^{ij}\cdot r_0^j - \sum_{j=1}^{3} B_1^{ij}\cdot p_0^j \\ &= \Big(S_{0R} + \frac{\vec{n}\cdot\vec{r}_0}{(\vec{u}_0\cdot\vec{n})}\Big)\cdot u_0^i \end{aligned}$$

and:

$$\begin{aligned} c^i_{0,2} &= p^i_0 - \sum_{j=1}^{3} A^{ij}_2 \cdot r^j_0 - \sum_{j=1}^{3} B^{ij}_2 \cdot p^j_0 \\ &= 0 \end{aligned}$$

The quality of the fit will in turn depend on the choice of the expansion point. In order to choose a good expansion point let's look at Fig 8.2 and try to figure out for which values of $\overrightarrow{r}_0$ and $\overrightarrow{p}_0$ we have equality between the Taylor approximation and the the description of the state vector. Let's call:

$$\begin{aligned} \mathbf{a} &= \overrightarrow{r}'_R - \overrightarrow{r}_0 \\ \mathbf{b} &= \overrightarrow{r}_R - \overrightarrow{r}_V \\ \mathbf{c} &= \overrightarrow{r}_R - \overrightarrow{r}'_R \end{aligned}$$

We have though:

$$\mathbf{c} = \mathbf{b} - \mathbf{a} - \overrightarrow{r}_{\mathbf{0}} + \overrightarrow{r}_{\mathbf{V}}$$

with:

$$\begin{aligned} \mathbf{b} &= h^1(\overrightarrow{r}_V, \overrightarrow{p}_V) + \epsilon - \overrightarrow{r}_{\mathbf{V}} \\ &= S_{VR} \cdot \overrightarrow{u}_V + \epsilon \end{aligned}$$

and

$$\begin{aligned} \mathbf{a} &= h^1(\overrightarrow{r}_0, \overrightarrow{p}_0) + \epsilon' - \overrightarrow{r}_{\mathbf{0}} \\ &= S_{0R} \cdot \overrightarrow{u}_0 + \epsilon' \end{aligned}$$

We have then on one hand:

$$\begin{aligned} \mathbf{c} &= h^1(\overrightarrow{r}_V, \overrightarrow{p}_V) + \epsilon - \mathbf{h^1}(\overrightarrow{r}_{\mathbf{0}}, \overrightarrow{p}_{\mathbf{0}}) - \epsilon' \\ &= \mathbf{A_1} \cdot (\overrightarrow{r}_{\mathbf{V}} - \overrightarrow{r}_{\mathbf{0}}) + \mathbf{B_1} \cdot (\overrightarrow{p}_{\mathbf{V}} - \overrightarrow{p}_{\mathbf{0}}) + \mathbf{R_1} + \epsilon - \epsilon' \\ &= \overrightarrow{r}_V - \overrightarrow{r}_0 - \frac{\overrightarrow{n} \cdot (\overrightarrow{r}_V - \overrightarrow{r}_0)}{\overrightarrow{u}_0 \cdot \overrightarrow{n}} \cdot \overrightarrow{u}_0 + \frac{S_{0R}}{\| \overrightarrow{p}_0 \|} \cdot \left(\overrightarrow{p}_V - \overrightarrow{p}_0 - \frac{\overrightarrow{n} \cdot (\overrightarrow{p}_V - \overrightarrow{p}_0)}{\overrightarrow{u}_0 \cdot \overrightarrow{n}} \cdot \overrightarrow{u}_0 \right) + \mathbf{R_1} + \epsilon - \epsilon' \end{aligned}$$

and on the other one:

$$\mathbf{c} = S_{VR} \cdot \overrightarrow{u}_V + \epsilon - \mathbf{S_{0R}} \cdot \overrightarrow{u}_{\mathbf{0}} - \epsilon' - \overrightarrow{r}_{\mathbf{0}} + \overrightarrow{r}_{\mathbf{V}}$$

So the formula becomes exact when:

$$\begin{aligned} &(1) && \tfrac{\overrightarrow{n} \cdot (\overrightarrow{r}_V - \overrightarrow{r}_0)}{\overrightarrow{u}_0 \cdot \overrightarrow{n}} \cdot \overrightarrow{u}_0 && = 0 \\ &(2) && S_{0R} && = S_{VR} \\ &(3) && \| \overrightarrow{p}_0 \| && = \| \overrightarrow{p}_V \| \\ &(4) && \tfrac{\overrightarrow{n} \cdot (\overrightarrow{p}_V - \overrightarrow{p}_0)}{\overrightarrow{u}_0 \cdot \overrightarrow{n}} \overrightarrow{u}_0 && = 0 \\ &(5) && \mathbf{R_1} && = 0 \end{aligned} \tag{8.11}$$

Chapter 9

Study of the Algorithm performance

9.1 A simple toy Monte Carlo

For a very preliminary study of the Kalman vertex fit algorithm performance, a toy Monte Carlo was set up. It uses a simplified HARP environment made of simple volumes, surfaces and fields. We have chosen a model of straight tracks intersecting all in the same point. Starting from this intersection point, the normalized momentum vector and the distance between points, a set of points following a straight line is created. A random smearing is then added to the points following a Gaussian distribution of a given resolution. This corresponds to the measurement of the track. For each trajectory we compute a seed state necessary for the track fit. The track is then fitted. The magnetic field in the TPC is set to 0.7 T in z and 0 T in x and y. We have chosen as reference surface R, a disc perpendicular to the z axis, of radius 100 cm situated at -30 cm of the center of our toy TPC cylinder (corresponding to the HARP coordinate $z = 0$). The tracks are extrapolated to the surface R. The position vector $\overrightarrow{r}_R$, the matrix $\mathbf{C}$, the momentum vector $\overrightarrow{p}_R$ and the matrix $\mathbf{D}$ at the reference surface are computed. The position-momentum correlation matrix $\mathbf{E}$ is set equal to zero. These constitute the state vector:

$$\mathbf{v_R} = \begin{pmatrix} \overrightarrow{r}_R \\ \overrightarrow{p}_R \end{pmatrix}$$

and the state matrix $\mathbf{V}$:

$$\mathbf{V} = \begin{pmatrix} \mathbf{C} & \mathbf{E} \\ \mathbf{E^T} & \mathbf{D} \end{pmatrix}$$

The trajectory is then added to the vertex object. A seed state for the vertex is given by an a priori vertex position $\overrightarrow{r}^0_V$ and matrix $\mathbf{C_0}$. The latter is chosen to be diagonal with:

$$C_0^{11} = C_0^{22} = C_0^{33}$$

The vertex fit algorithm is called using the mathematics described previously. As seed state we give:

$$\mathbf{v_0} = \begin{pmatrix} \overrightarrow{r}^0_V \\ 0 \end{pmatrix}$$

and:

$$\mathbf{V_0} = \begin{pmatrix} \mathbf{C_0} & 0 \\ 0 & 0 \end{pmatrix}$$

Then we loop over the tracks from $k = 0$ to the total number of tracks. We compute the $\mathbf{c_0}$ vector, $\mathbf{A}$ and $\mathbf{B}$ matrices. We compute the filter part using the equations (8.5). At the last track n we give to the smoothed state the filtered state and we loop then from track $k = n$ to 0 (see equations (8.7)). The following parameters can be changed:

- the number of tracks we want to fit
- the intersection point of the tracks
- the momentum vector of each track
- the distance between track points
- the resolution of the smearing for the track fit
- the number of measurements for the track fit
- the first measurement of the track
- the seed state for the track fit
- the seed covariance matrix for the track fit
- the position of the expansion point
- the momentum of the track at the expansion point
- the seed vertex position $\overrightarrow{r}_V^0$
- the seed vertex covariance matrix coefficients of the vertex position C_0^{ii} (i = 1,3)

9.1.1 Pull study

One efficient way to study the algorithm performance is to compute the pull values of the fitted vertex position and momentum. The pull of a given variable x is equal to:

$$Pull(x) \quad = \quad \frac{x^{fit} - x^{true}}{\sigma_{x^{fit}}}$$

A typical good distribution of a pull variable while fitted by a Gaussian fit would be centered on zero and with a σ around one. The pull computation gives a first idea of the quality of the vertex fit. The parameters used for a pull computation over 100 events of two tracks of positive charge each are given in Table 9.1. The last component of the initial state vector of the track fit is not used. The last diagonal element of the initial state matrix for the track fit C_{44} is not used. The measurement error in z for the track fit is a parameter not influencing the pull results. Depending on the number of measurements, the pull results can change a lot, so we kept a constant value for test purposes. The momentum resolution influences also the pull values. Best pull values have been obtained for the value reported in the Table 9.1.
Different values of $\overrightarrow{r}_0$ and $\overrightarrow{p}_0$ have been chosen for the pull computation. The global results are summarized in Table (9.2) together with the five conditions of the equations (8.11) being fulfilled or not. At first look, we can conclude that it is very important to compute a $\overrightarrow{p}_0$ as close as possible to the true momentum at the vertex. This is why we have chosen to compute $\overrightarrow{p}_0$ at the reference surface R. If the reference surface

Vertex position (cm)	(0,0,-1)
Momentum track 1 (GeV/c)	(0,1,2)
Momentum track 2 (GeV/c)	(0,-1,2)
Seed vertex covariance matrix coefficients C_0^{ii}	100
Initial state vector of the track fit	(0, 0, 0.1, 0.1, 0)
Initial state matrix of the track fit	$C_{00} = C_{11} = 10$ and $C_{22} = C_{33} = C_{44} = 1$
z position of the first measurement (cm)	0
Distance between measurement points (cm)	1
Smearing in x (cm)	1
Smearing in y (cm)	1.1
Smearing in z (cm)	1
Measurement error in z for the track fit (cm)	0.1
Number of measurements	20
Momentum resolution (GeV/c)	0.01

Table 9.1: Parameters values entering in the vertex fit

$\overrightarrow{r}_0$	$\overrightarrow{p}_0$	Conditions not fulfilled	Vertex	Momentum	Pull $\overrightarrow{r}_V$	Pull $\overrightarrow{p}_V$	χ^2
$\overrightarrow{r}_V$	(0,0,1)	2 - 3 - 4 - 5	(0,0,-2)	OK	shifted in z	too small in y	bad
$\overrightarrow{r}_V$	$\overrightarrow{p}_V$	5	OK	OK	OK	too small in y	OK
(0,1,-1)	$\overrightarrow{p}_V$	2 - 5	OK	OK	OK	too small	OK
(0,1,-1)	(0,0,1)	2 - 3 - 4 - 5	(0,0,-2)	OK	shifted in z	too small in y	bad

Table 9.2: Pull study with two tracks

Track	$\overrightarrow{p}_V$	Pull x	Pull y	Pull z	Pull p_x	Pull p_y	Pull p_z
1	(0,1,2)	0.008921	-0.01451	0.1514	0.01018	0.002895	-0.03232
		1.064	1.049	1.001	0.9320	0.7445	1.008
2	(0,-1,2)	0.008921	-0.01451	0.1514	0.03152	-0.02269	-0.03218
		1.064	1.049	1.001	0.9768	0.8016	1.040
3	(1,0,2)	0.008921	-0.01451	0.1514	0.004411	0.006758	-0.02948
		1.064	1.049	1.001	0.9953	0.8970	0.9907
4	(-1,0,2)	0.008921	-0.01451	0.1514	-0.03997	0.02090	-0.007224
		1.064	1.049	1.001	0.9643	0.8449	0.9305

Table 9.3: Pull fit results, mean value in cm (top) and σ (bottom)

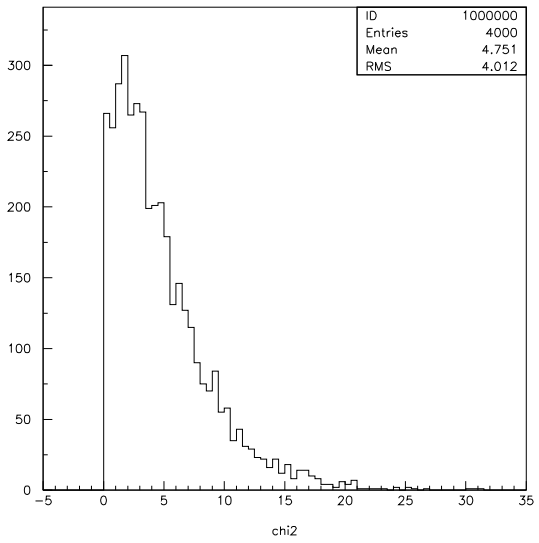

Figure 9.1: χ^2 distribution for a vertex fit with four tracks

is close enough to the true vertex position it is a good expansion point estimate. A good choice of $\overrightarrow{r}_0$ can also be helpful but it is not easy to find the best point for a given set of tracks and a robust estimate has to be computed using a separate algorithm (e.g. calculating the minimum distance point between tracks). The value of $\overrightarrow{r}_0$ does not seem to influence the vertex fit results. A point situated not on the reference surface nor at the vertex position (position (0,1,-1) cm) has been chosen.
Even while choosing the true vertex position and momentum for $\overrightarrow{r}_0$ and $\overrightarrow{p}_V$, the pulls for the momentum are too small in y.
Increasing the number of tracks to four and being in both y-z and x-z planes, we have computed the pulls for 1000 such events. The true vertex position is the same as for the study with two tracks. Two tracks of momentum (-1, 0, 2) GeV/c and (1, 0, 2) GeV/c have been added. The σ of the pull distribution is slightly too large for the position and slightly too small for the momentum. Pull results are given in Table (9.3). The χ^2 distribution of the vertex fit is given in Figure (9.1).

9.2 Vertex performance study with Monte Carlo data

9.2.1 Monte Carlo data production

In order to study the performance of the vertex fit algorithm we have produced Monte Carlo data using the version $v7r4$ (see Appendix A) of the HARP software. The HARP simulation environment contains a so-called 'exclusive' generator which produces, from a beam particle that annihilates in the target, secondaries that will travel in the HARP environment. The number, type, momentum direction, kinetic energy, time and position at generation, of the secondaries can be chosen by modifying the 'exclusive' generator. The HARP environment description, like material, gases and fields files, is used both by the simulation and the reconstruction software. A proton of 3 GeV energy created at (0,0,-450) cm before the target is used as beam particle. Two charged pions of 1 GeV/c momentum are created in the target where the beam particle interacts. They have as 3D polar angles $\varphi_{\pi^-} = \varphi_{\pi^+}$ and $\theta_{\pi^-} = -\theta_{\pi^+}$. The HARP 2002 geometry files have been used for this simulation. The target chosen was the Be target of 5% interaction length. It is possible to switch off the solenoid field at the simulation stage.

9.2.2 Monte Carlo data reconstruction

The Monte Carlo data can be saved in a file and reprocessed for reconstruction purposes. The matching between the Monte Carlo particle and the reconstructed particle is computed differently given the detector type. If the reconstructed particle has been seen by the MWPCs, the first reconstructed track belonging to this particle is identified as a MWPC type track. If the reconstructed particle has been seen by the TPC and not by the MWPCs, its first reconstructed track will be identified as a TPC type track. If the reconstructed particle has been seen by the NDCs and not by the TPC nor by the MWPCs, the first reconstructed track belonging to the reconstructed particle will be identified as NDC type track.
For a MWPC type track, it will assign as corresponding Monte Carlo particle, the Monte Carlo particle which created the maximum number of points in the track. The number of points can serve as cut on the quality of the matching.
For a TPC type track, the information on the Monte Carlo particles which created the signal is not conserved. The matching is done in a different way. For each Monte Carlo particle, we calculate the following number:

$$\sqrt{(\theta_{MC} - \theta_{TRK})^2 + (\varphi_{MC} - \varphi_{TRK})^2}$$

where θ and φ are the 3D polar angles of the momentum for the Monte Carlo particle (MC) and the TPC track reconstructed by the Kalman package (TRK). This value is reported in [55] to be the best matching parameter between a TPC track and a Monte Carlo particle. The Monte particle which correspond to the smallest value is attached to the reconstructed particle and the 'angular value' can be used later on as quality of the matching.
For a NDC type track the matching between the Monte Carlo particle and the reconstructed one is done in the same manner as for the MWPC type tracks. It will assign as matched Monte Carlo particle the one which contributed to the maximum number of points in the tracks. This number serves also for a cut on the quality of the matching.
The vertex fit has been extended for accepting TPC tracks from the Kalman fit. It assigns to each reconstructed particle a reference surface (refSurf) given the type of detector crossed. If the MWPC detector has seen the reconstructed particle the reference surface is a disc of 10 cm default radius situated at $z = 0$. If the TPC detector has seen the reconstructed particle and not the MWPCs, the reference surface is a cylinder of 50 cm default length and 10 cm default radius centered at $z = 0$. If the NDC detector has seen the reconstructed particle but not the TPC nor the MWPCs, the reference surface is a disc of 40 cm default

Detector	Number of reconstructed particles	particle type
MWPC	9428	proton
TPC	987	π^-
TPC	4623	π^+
TPC	10	μ^+
NDC	120	proton

Table 9.4: Detector and particle type of the reconstructed particle in the vertex fit (Be thin target, MC for TPC study)

radius situated at $z = 0$. If none of the three detectors has seen the reconstructed particle, its first track will not be used by the vertex fit. For a reconstructed particle belonging to the NDCs, if the first module of the NDCs detector has no hit, the particle is rejected. Each first track of the reconstructed particle is propagated (using the Kalman propagator) to its corresponding reference surface and rejected if it does not intersect it. For each track the expansion point position is the same and its default value is (0,0,0) cm. The momentum of the track at the expansion point is the momentum at the reference surface computed by the Kalman extrapolator. The seed position has for default value (0,0,0) cm and the default covariance matrix for the position is set at zero except for diagonal terms which are set to a value of 100. The vertex is computed using the vertex fitter described in chapter 8. The solenoid field can be switched off. In this way a track crossing the TPC will be described by the Kalman package as a straight line and not as an helix.

9.2.3 Pull results and vertex resolution

TPC reconstruction and vertex performances study

Results from the Monte Carlo data simulating pions with $\theta = \pm\pi/4$ rad and $\varphi = 0$ are already giving a first idea of the quality of the track reconstruction in the TPC and of the vertex fit performance. The number of accepted TPC tracks in the reconstruction was so low that we had to simulate ten times more events than in the NDC study case (presented in the following section). A fraction of 9738 Monte Carlo events over 10000 has been reconstructed with the vertex. Only 382 events have three reconstructed particles. The detector and particle type for the 15168 reconstructed particles is given in Table 9.4. The difference in number between reconstructed π^- and π^+ in the TPC is a sign of a problem in the treatment of the particle charge by the reconstruction. The reconstructed particles identified as NDC type are the beam particles. They have been identified as such either because they could not be reconstructed in the MWPCs or because a new reconstructed particle has been created from a track in the NDC if there is no matching between MWPC an NDC tracks. The reconstruction inefficiency fractions for the tracks entering the vertex fit are given in Table 9.5. Further investigation has to be done to understand why we compute negative matrix elements for some cases. The intermediate $\chi^2_k(filter)$ is given in Equation 8.6 and the $\chi^2_k(smoother)$ in Equation 8.10. We have the following identity:

$$\chi^2_n(smoother) = \chi^2_n(filter)$$

The χ^2_V (result of the vertex fit) is therefore defined as:

$$\chi^2_V = \chi^2_1(smoother)$$

It is quite clear that negative values of $\chi^2_k(filter)$, $\chi^2_k(smoother)$ or χ^2_V are coming from the tracks which have negative elements in the position-momentum covariance matrix. Tracks entering in the inefficiency

Type	Parameters	Fraction of the tracks (%)
TPC	Negative flag	2.14
TPC	Negative D_{00}, D_{11} and D_{22}	0.07
TPC	Negative χ^2_F	0.05
MWPC	Negative χ^2_S	0.02
TPC	Negative χ^2_S	0.05
MWPC	Negative χ^2_V	0.02
TPC	Negative χ^2_V	0.05

Table 9.5: Reconstruction inefficiency for TPC and MWPC tracks entering in the vertex (Be thin target, MC for TPC study)

table have been excluded from the pull and vertex resolution plots. Despite the fact that it seems that we reconstruct well the TPC tracks when looking at the χ^2/ndf (ndf being the number of degrees of freedom) of the track fit (see Figure 9.2) the pulls do not have a correct shape nor for the position nor for the momentum. For the pulls and vertex resolution plots a cut on χ^2/ndf <20 is applied. Figure 9.3 show the

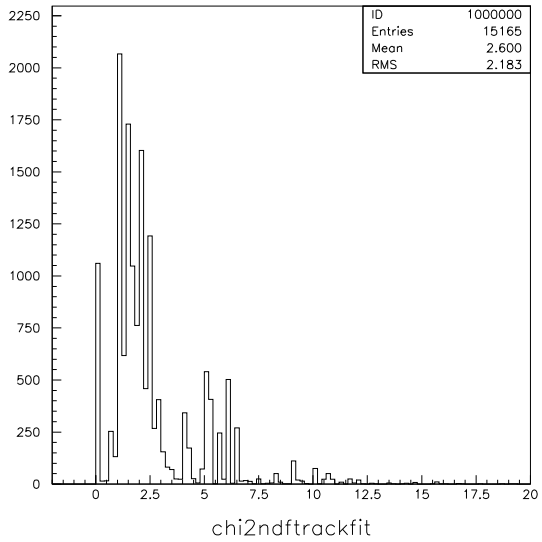

Figure 9.2: χ^2/ndf distribution of the track fit (Be thin target, MC for TPC study), $\chi^2/ndf < 20$

χ^2_F distribution of the vertex fit with a cut on its value below 20. It presents a very long tail and its shape is not understood. We conserved this cut for the pulls and vertex resolution plots.

Figures 9.4 to 9.6 give the Gaussian fit results for the pulls in x, y and z from the vertex fit for particles reconstructed as π^- and π^+ when three particles are reconstructed. The pulls in x present a σ which is too large compared to what is expected.

The pulls in y are shifted $\sim$ 1 and present also a too large σ.

The pulls in z are shifted $\sim$ -1 and present a too small value for σ. The shift in z could be the sign of a probable misalignement of the TPC geometry compared to the target position in the algorithm which defines the relative position of the HARP volumes. The pulls distribution for the momentum and for the two pions are shown in Figures 9.7 to 9.9 when three particles are reconstructed. Concerning the distribution in x

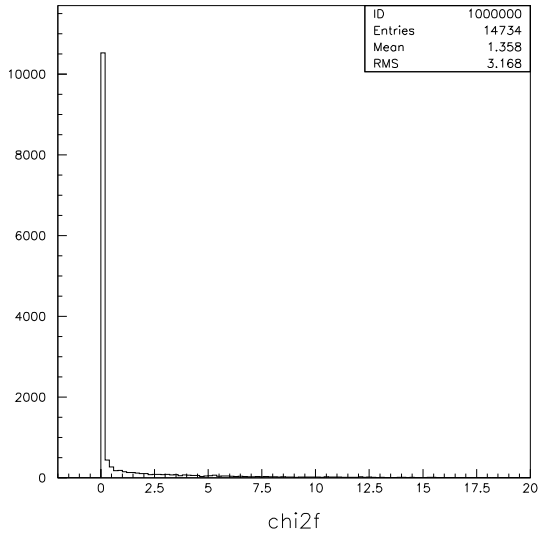

Figure 9.3: $\chi^2_k(filter)$ distribution of the vertex fit (Be thin target, MC for TPC study), $0 < \chi^2_k(filter) < 20$

for the momentum we expect a gaussian shape (since our particle is created in the x-z plane). Comparison between the shape for the π^- and the π^+ show that they present a quite different behaviour and non gaussian shape at all. Pull distributions for the momentum in y have also a non gaussian shape and a different shape for the π^- and the π^+. This is symptomatic of a momentum reconstruction problem in the TPC. The difference in shape for the π^+ and π^- is also the hint for a possible problem in the treatment by the reconstruction software of negatively charged particles where the reconstruction efficiency is about 4 times smaller than for positive particles. Pull distributions for the momentum in z are also different for π^- and π^+. A quick look at the reconstructed momentum for TPC tracks coming from the Kalman track fit shows that the momentum is not correctly estimated by the fit. Further investigation on output results coming from the TPC helix fit show that the TPC helix fit is computing correctly the momentum (see Appendix B) despite a slight behaviour difference between π^- and π^+ which is not explained. The wrong momentum assigment is done at the creation of the Kalman TPC track. Unfortunatly the reconstructed particle is created after the Kalman TPC fit and not after the TPC helix fit. The vertex resolution has also been computed for the two pions when three particles are reconstructed. The fit of the vertex resolution in x, y and z are shown in Figure 9.10 to 9.12. This gives a vertex resolution in x an y of 1 mm. The vertex resolution in z is ~ 2 mm and there is a non-neglible shift of ~ 0.75 mm in the vertex position. Improvement of the vertex fit for TPC tracks can be expected as soon as the reconstruction of the TPC tracks by the Kalman track fit will improve.

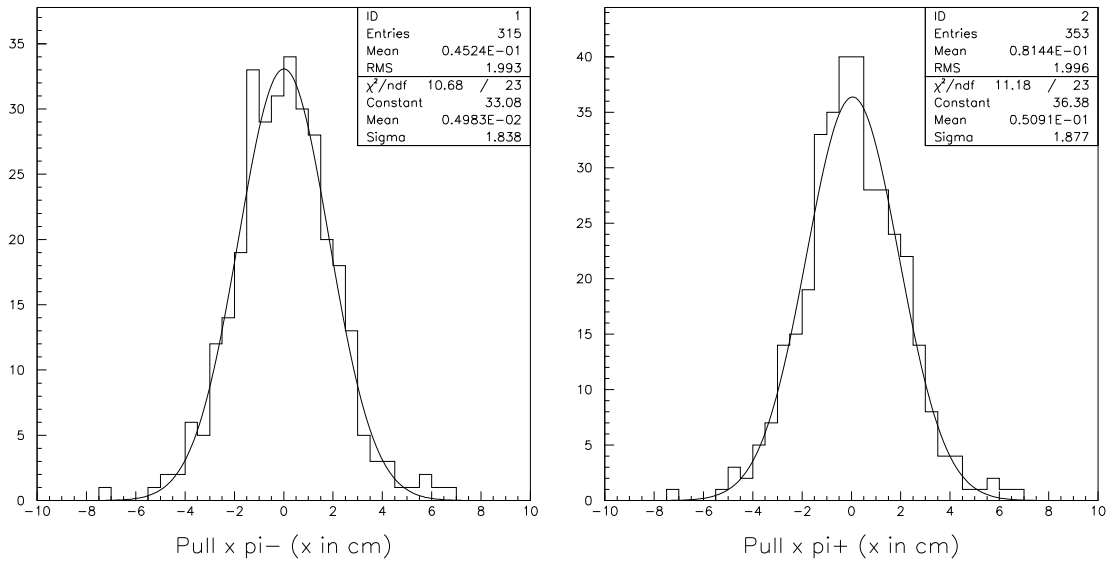

Figure 9.4: Fit of the pull distribution for the vertex position in x (Be thin target, MC for TPC study)

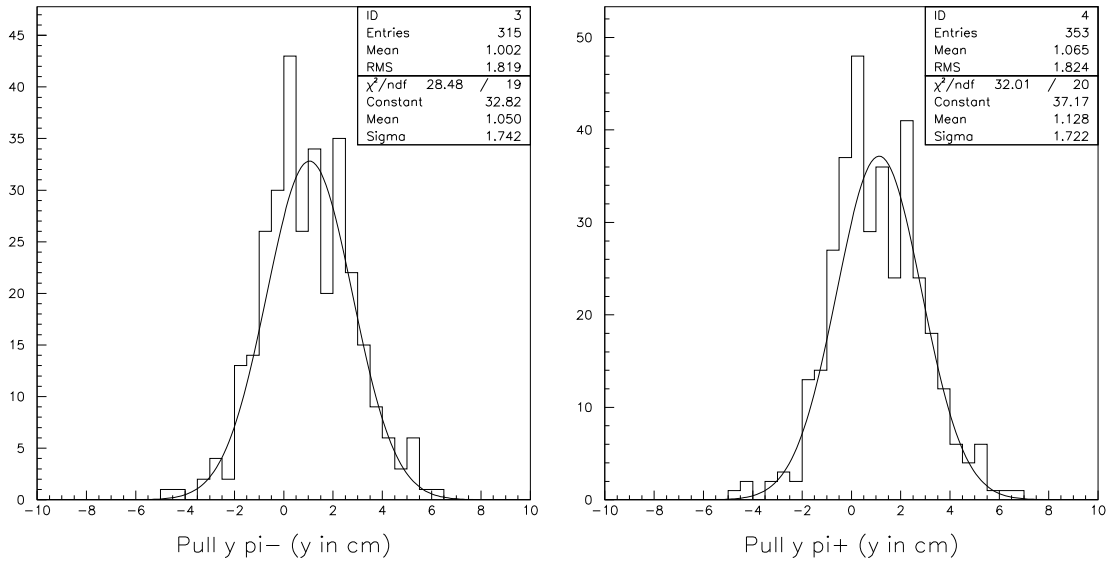

Figure 9.5: Fit of the pull distribution for the vertex position in y (Be thin target, MC for TPC study)

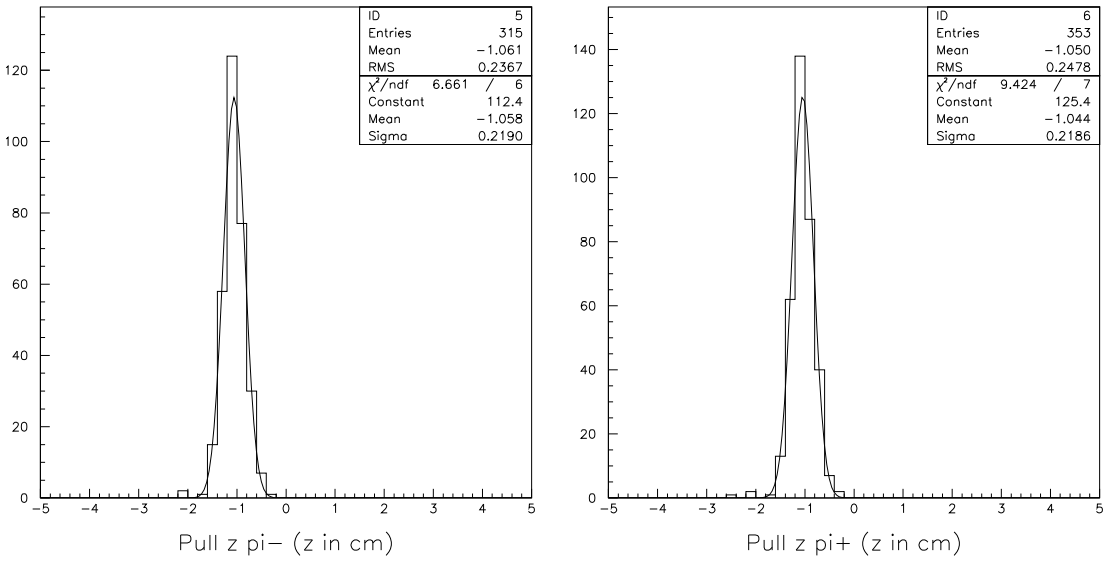

Figure 9.6: Fit of the pull distribution for the vertex position in z (Be thin target, MC for TPC study)

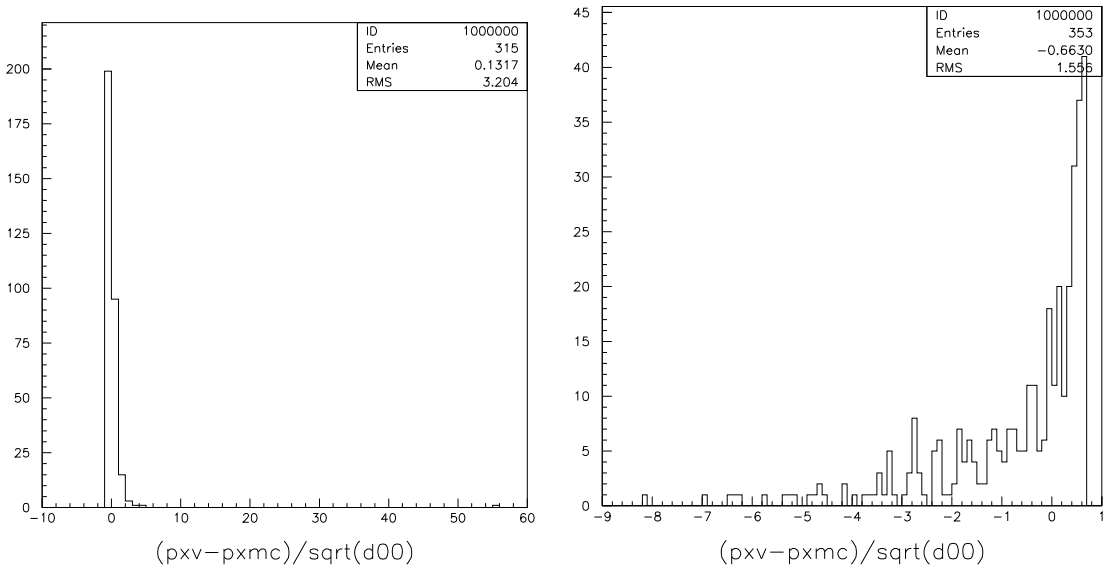

Figure 9.7: Pull distribution for the momentum in p_x (momentum in GeV/c) for the π^- (left) and the π^+ (right) (Be thin target, MC for TPC study)

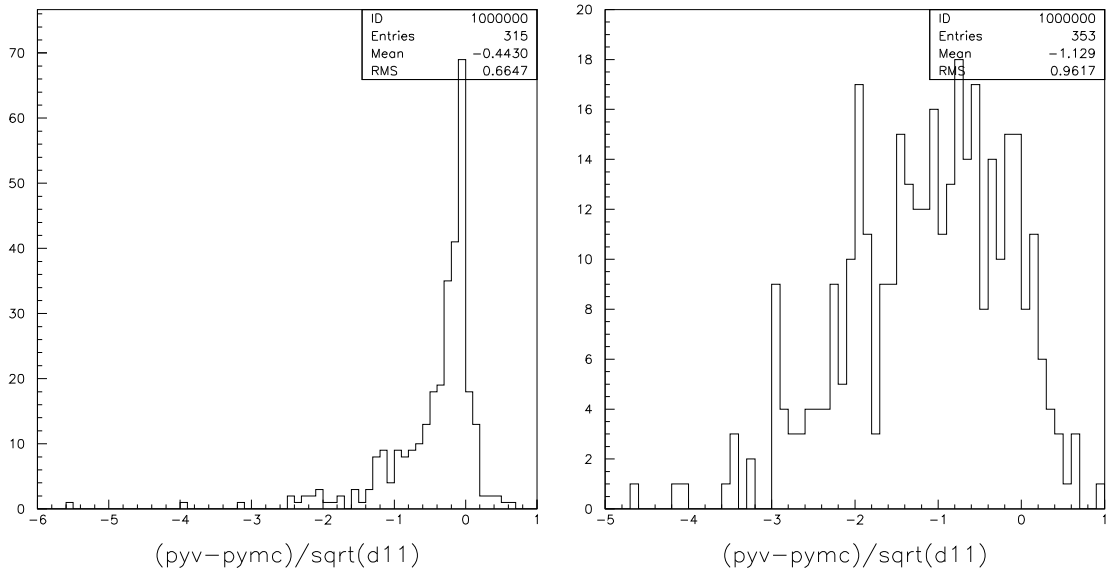

Figure 9.8: Pull distribution for the momentum in p_y (momentum in GeV/c) for the π^- (left) and the π^+ (right) (Be thin target, MC for TPC study)

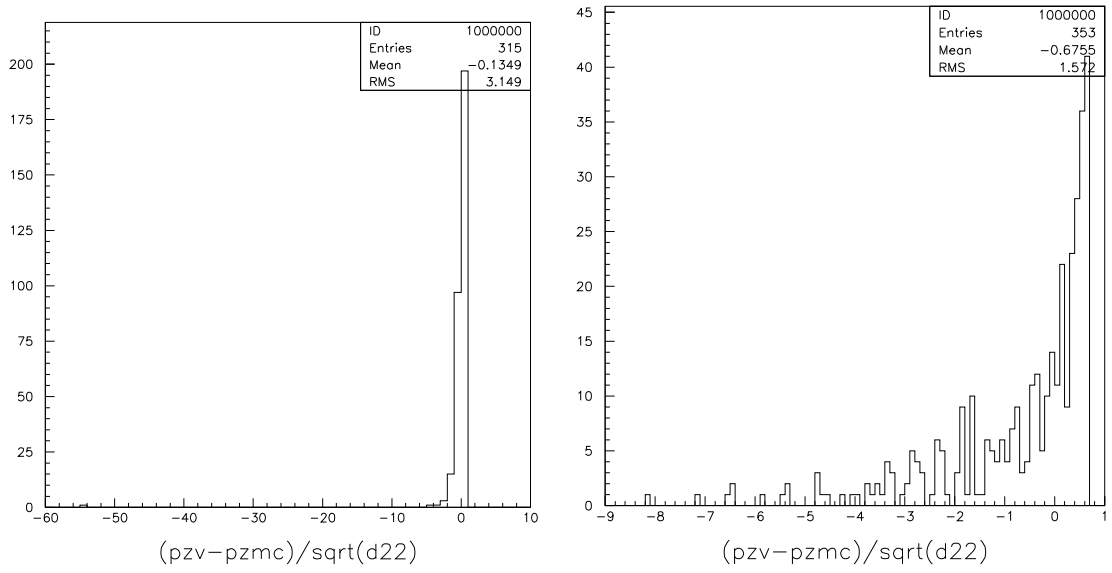

Figure 9.9: Pull distribution for the momentum in p_z (momentum in GeV/c) for the π^- (left) and the π^+ (right) (Be thin target, MC for TPC study)

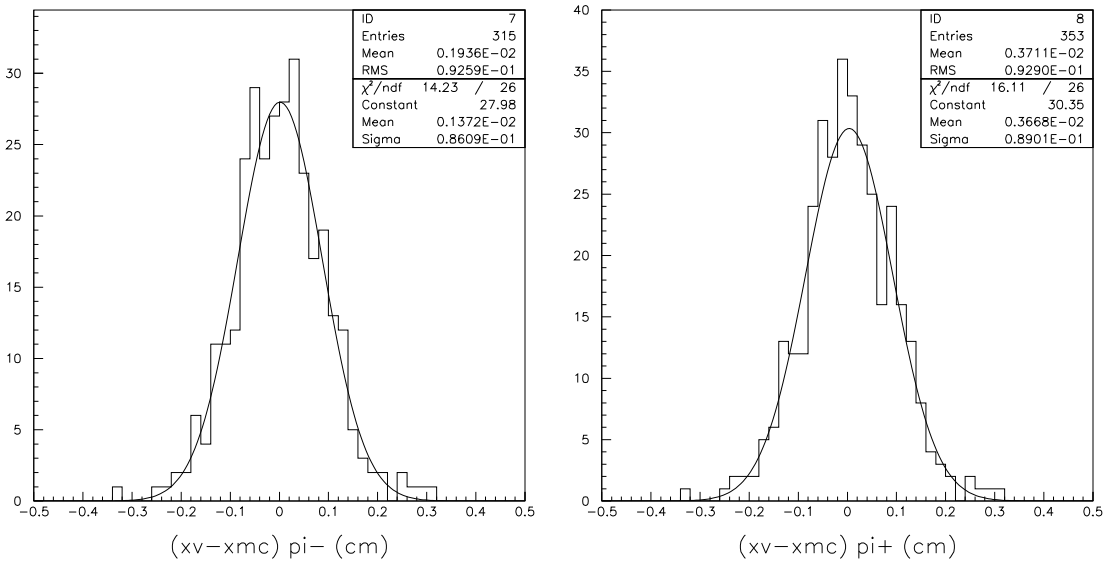

Figure 9.10: Fit of the vertex resolution in x (Be thin target, MC for TPC study)

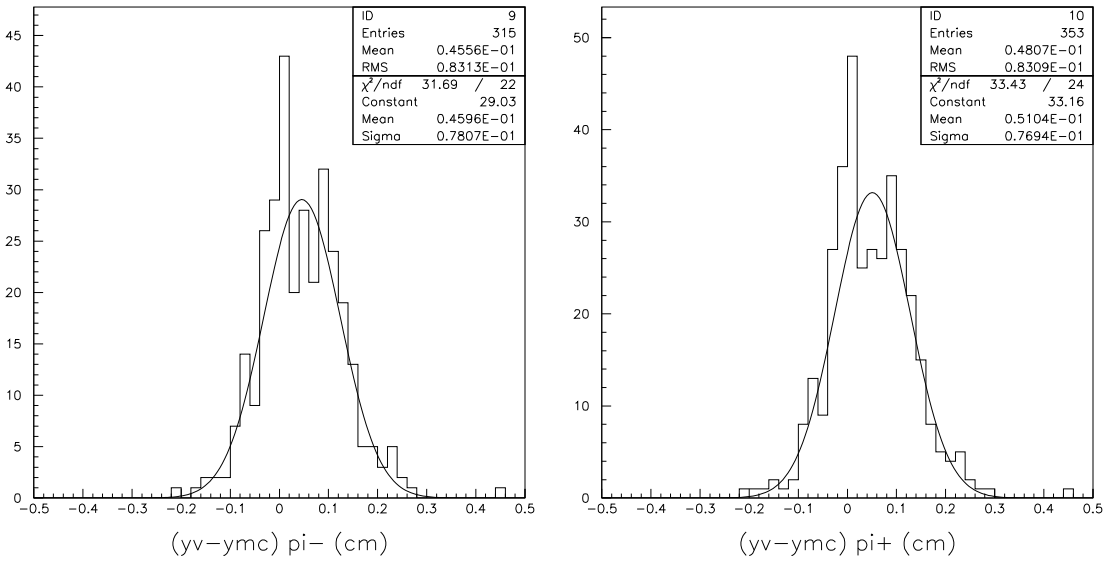

Figure 9.11: Fit of the vertex resolution in y (Be thin target, MC for TPC study)

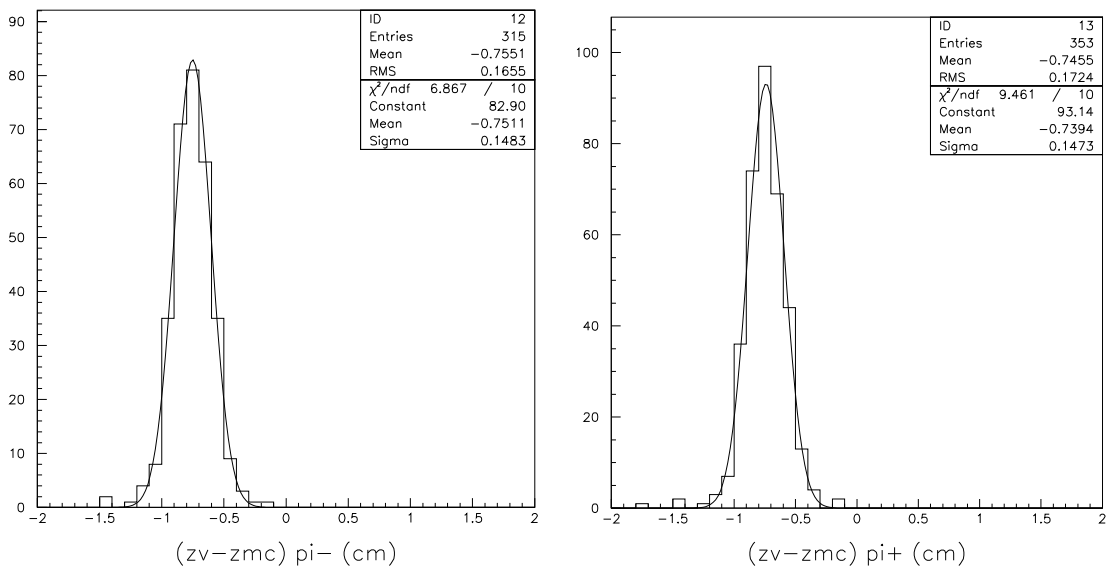

Figure 9.12: Fit of the vertex resolution in z (Be thin target, MC for TPC study)

Number of events	Number of MC particles	particle type
11	1	proton
971	3	proton, π^-, π^+
2	4	proton, π^-, π^+, μ^+
3	4	proton, π^-, π^+, μ^-
8	5	proton, π^-, π^+, μ^-, $\overline{\nu}_\mu$
5	5	proton, π^-, π^+, μ^+, ν_μ

Table 9.6: Monte Carlo particles registered, ('exclusive' generator for NDC study, no solenoid field)

Detector	Number of reconstructed particles	particles type
MWPC	872	proton
TPC	11	π^-
TPC	5	π^+
NDC	855	π^-
NDC	6	μ^+
NDC	11	μ^-
NDC	882	π^+
NDC	6	proton

Table 9.7: Detector and particle type of the reconstructed particle in the vertex fit (Be thin target, MC for NDC study, no solenoid)

NDC reconstruction and vertex performance study without solenoid field

For a study of NDC reconstruction and vertex performance we have simulated pions from Monte Carlo with $\theta = 150$ mrad and $\varphi = 0$. In this way, the pions are seen by the NDCs and not by the TPC. As preliminary study, we have used a TPC without solenoid field. For the track propagation in the TPC the straight line model is used (instead of the helix model) in absence of the solenoid field. This gives input on the possible misalignment problems we can encouter or a wrong estimate of the dipole field since it is the only field which remains switched on. We have produced 1000 Monte Carlo events. The Monte Carlo particles that have been produced are reported in Table 9.6. 931 events have been reconstructed with a vertex and 786 events have three particles at least. The detector and particle type of the 2648 reconstructed particles are given in Table 9.7. We are able to reconstruct some particles in the TPC despite their small θ angle due to the fact that they passed the cuts on the minimum number of rows that need to be hit or the minimum acceptance angle for accepting a TPC track. They have been excluded of the pull plots.
The NDC protons origin is the same as for the TPC study case.
The slight contamination in μ^- and μ^+ will give a contribution to the vertex for those events, which is pulling its position out of the true vertex position if they don't belong to the true vertex. They do not represent a important bias on the results. The reconstruction inefficiency fractions for the tracks entering the vertex fit are given in Table 9.8.
The χ^2/ndf of the track fit is given in Figure 9.13 for a cut at $\chi^2/ndf < 20$. It is peaked at a larger value than for the TPC study case. For the tracks entering the pull and vertex resolution plots, the cut below 20 is conserved.

Type	Parameters	Fraction of the tracks (%)
TPC	Negative flag	18.7
NDC	Momentum not measured	4.32

Table 9.8: Reconstruction inefficiency for TPC and NDC tracks entering in the vertex (Be thin target, MC for NDC study, no solenoid field)

The $\chi^2_k(filter)$ of the vertex fit is given in Figure 9.14 for a cut on its value below 20. As for the TPC

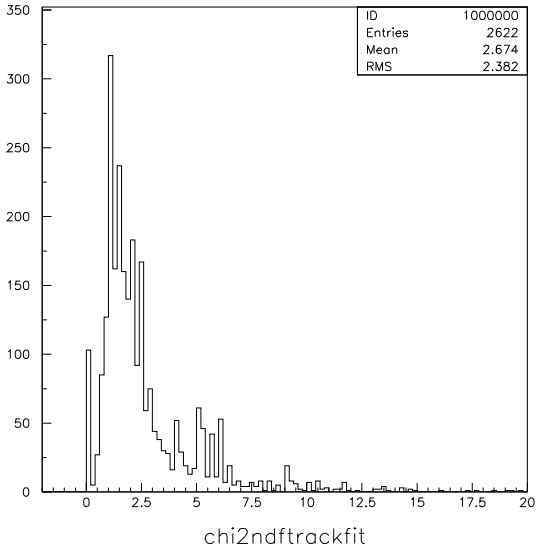

Figure 9.13: χ^2/ndf distribution of the track fit (Be thin target, MC for NDC study, no solenoid field), $\chi^2/ndf < 20$

study case it presents a very long tail. We kept this cut for the tracks entering the pull and vertex resolution plots.
The fit of the pulls for the vertex position, when three particles are reconstructed, are shown in Figures 9.15, 9.16 and 9.17 for both pions. The pulls in x still remain too large and are shifted by ~ 1. The same can be said concerning the pulls in y but they are correctly centered. The pulls in z have a reasonable σ but they are shifted by ~ 1.
The fit of the pulls for the momentum in p_x is shown in Figure 9.18 when three particles are reconstructed for both pions. They are shifted by ~ 0.36 and 0.40 for the π^- and the π^+ respectively and present a too small σ. This tells us that we are not reconstructing perfectly the momentum at the vertex.
The fit of the pulls for the momentum in p_y is shown in Figure 9.19 for the two pions when three particles are reconstructed. They are shifted by ~ 3.9 and 3.5 for the π^- and the π^+ respectively and the σ is too large for the π^- and too large for the π^+.
The fit of the pulls for the momentum in p_z is shown in Figure 9.20 for both pions, when three particles are reconstructed. The pulls are shifted by $\sim$ -0.2 and $\sim$ -0.4 for the π^- and the π^+ respectively which is the hint of a clear problem in the momentum reconstruction at the vertex. Bad pulls for the momentum can come from a wrong estimate of the momentum as input before the vertex fit and probably from misalignment in the dipole field estimation. The momentum estimated at the reference surface has been compared with the

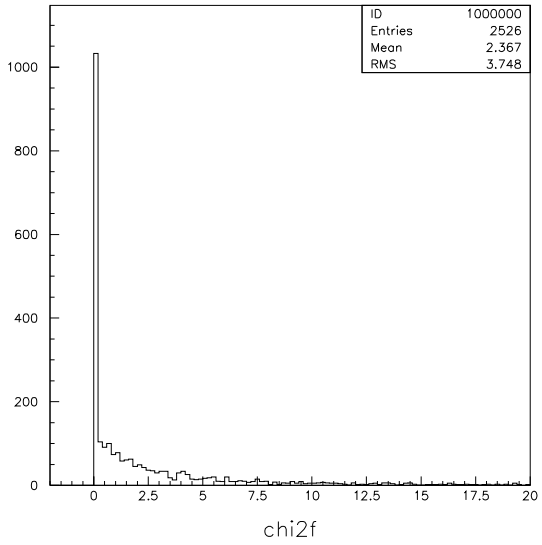

Figure 9.14: $\chi^2_k(filter)$ distribution of the vertex fit (Be thin target, MC for NDC study, no solenoid field), $\chi^2_k(filter) < 20$

Monte Carlo momentum (see Appendix B) showing that the vertex fit would certainly improve with some improvement of the NDC reconstruction.
The resolution of the vertex fit is shown in Figures 9.21, 9.22 and 9.23 for the two pions when three particles are reconstructed. The resolution in x is $\sim$ 1 mm for both pions which matches our expectations. The resolution in y is $\sim$ 1 mm but with a different shape as for the resolution in x. The resolution in z is $\sim$ 5 cm for the two pions which is of the same unit order as in the TPC case. The distribution is shifted by $\sim$ 6 mm as already observed in the pull plots in z.

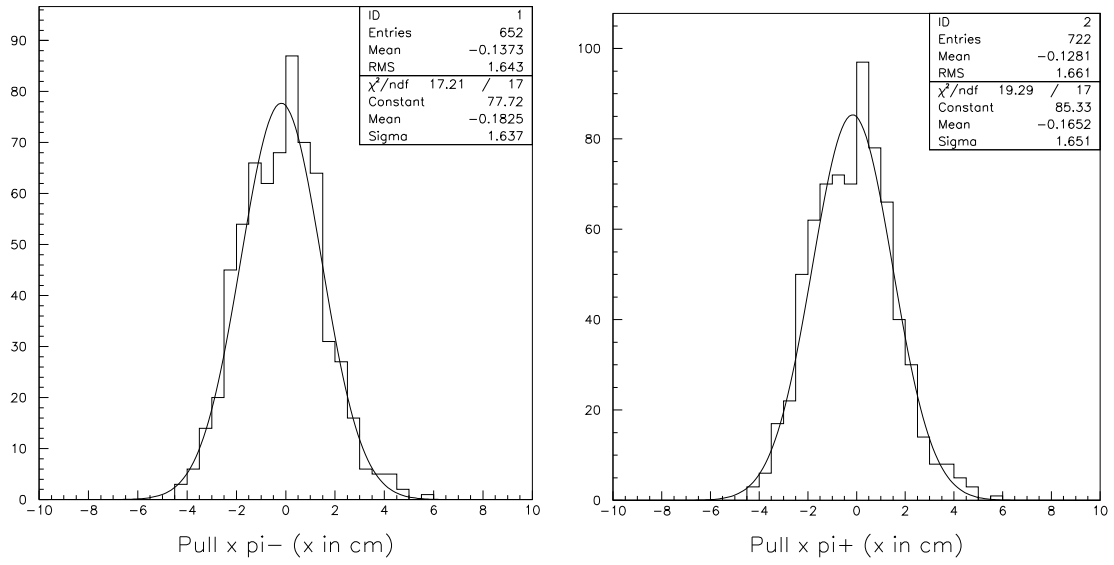

Figure 9.15: Fit of the pull distribution for the vertex position in x (Be thin target, MC for NDC study, no solenoid field)

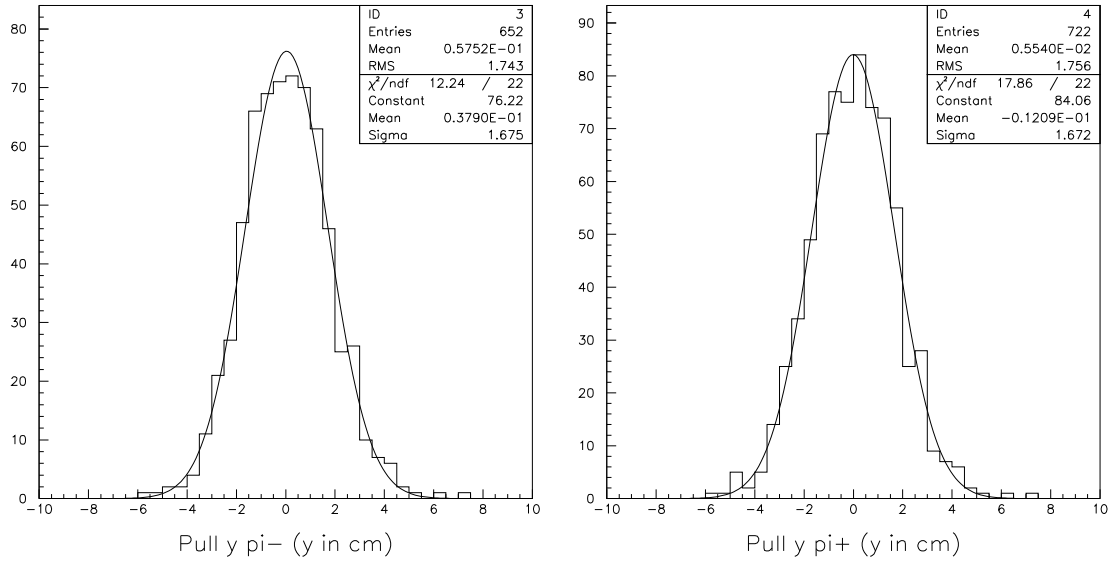

Figure 9.16: Fit of the pull distribution for the vertex position in y (Be thin target, MC for NDC study, no solenoid field)

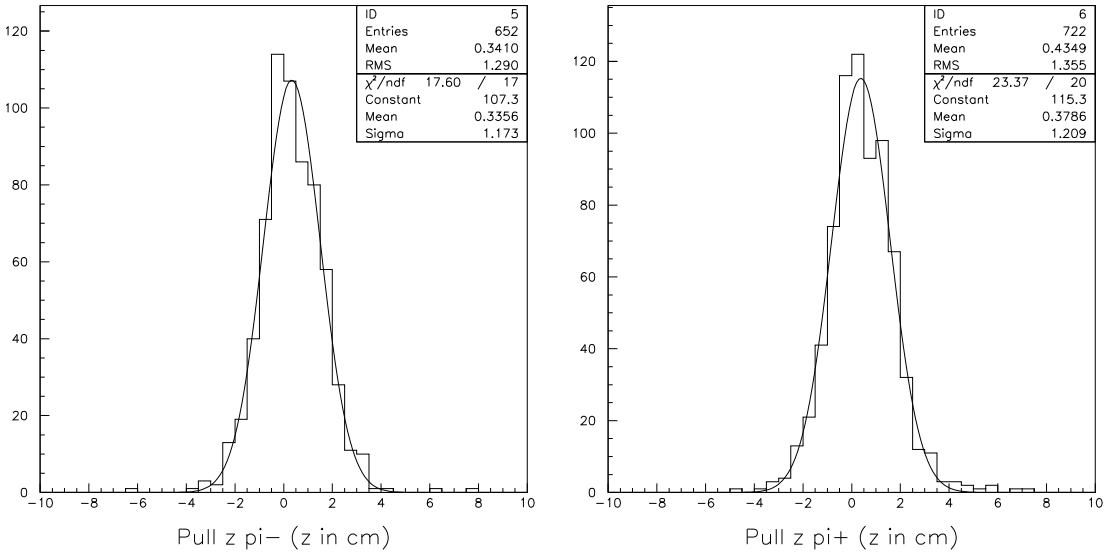

Figure 9.17: Fit of the pull distribution for the vertex position in z (Be thin target, MC for NDC study, no solenoid field)

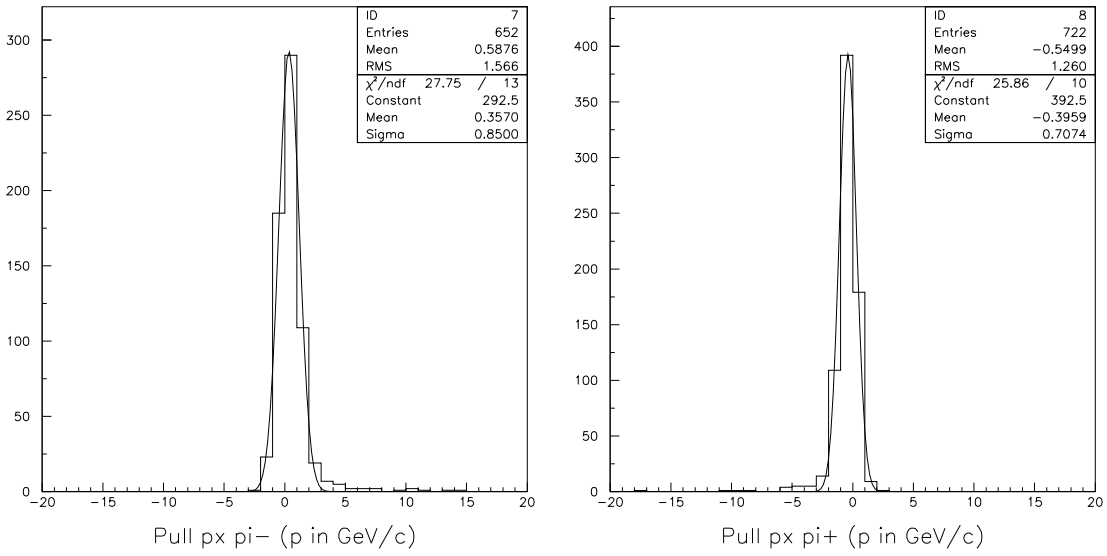

Figure 9.18: Fit of the pull distribution for the momentum in p_x (Be thin target, MC for NDC study, no solenoid field)

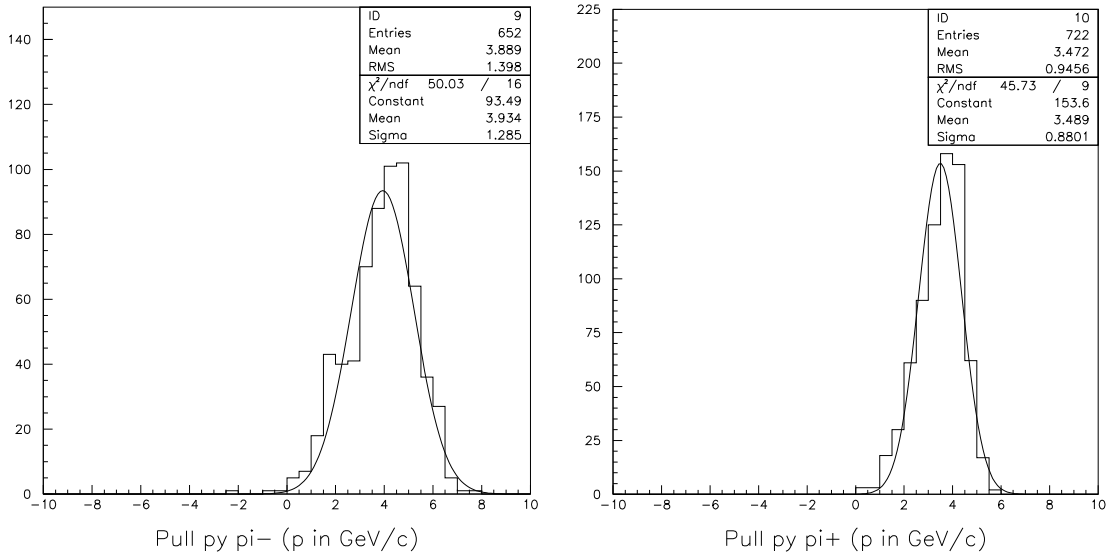

Figure 9.19: Fit of the pull distribution for the momentum in p_y (Be thin target, MC for NDC study, no solenoid field)

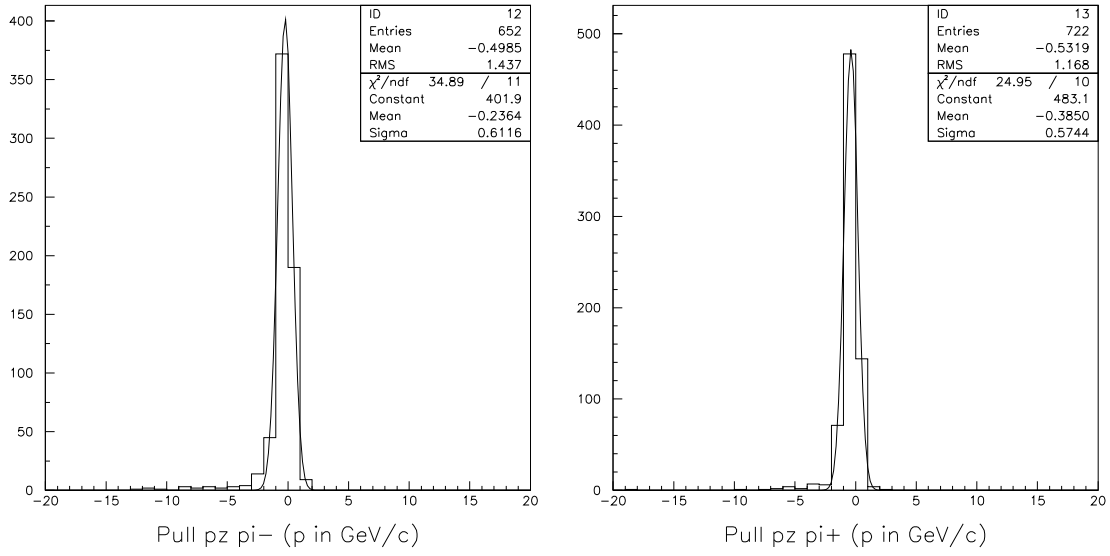

Figure 9.20: Fit of the pull distribution for the momentum in p_z (Be thin target, MC for NDC study, no solenoid field)

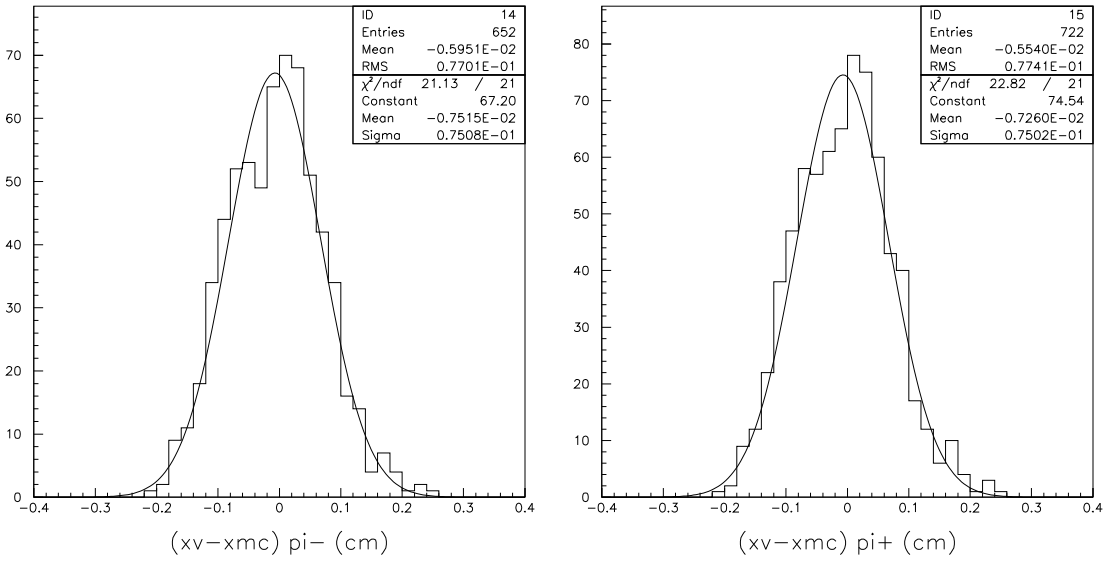

Figure 9.21: Fit of the vertex resolution in x (Be thin target, MC for NDC study, no solenoid field)

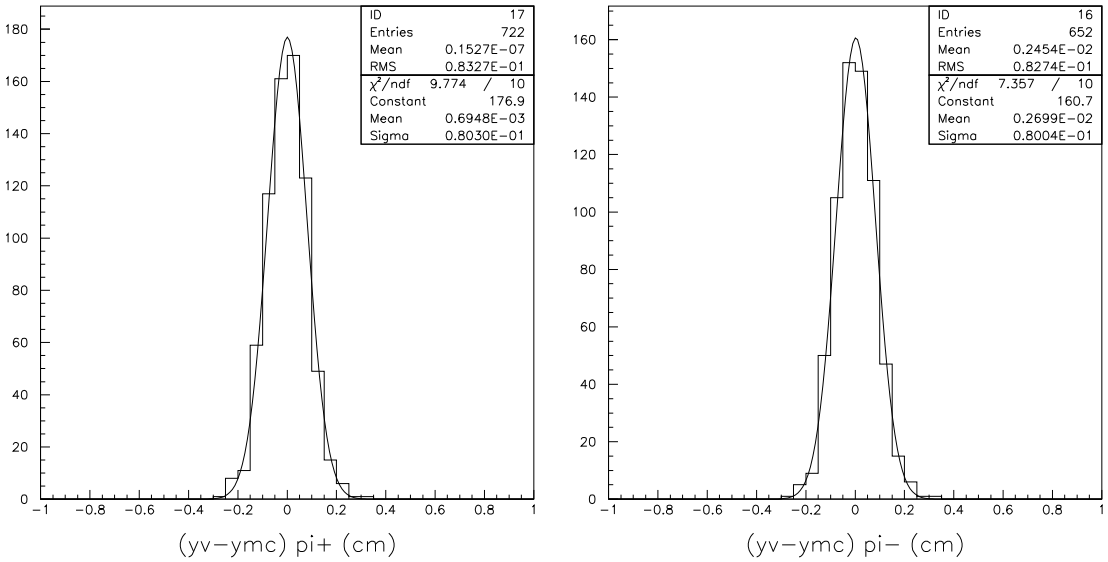

Figure 9.22: Fit of the vertex resolution in y (Be thin target, MC for NDC study, no solenoid field)

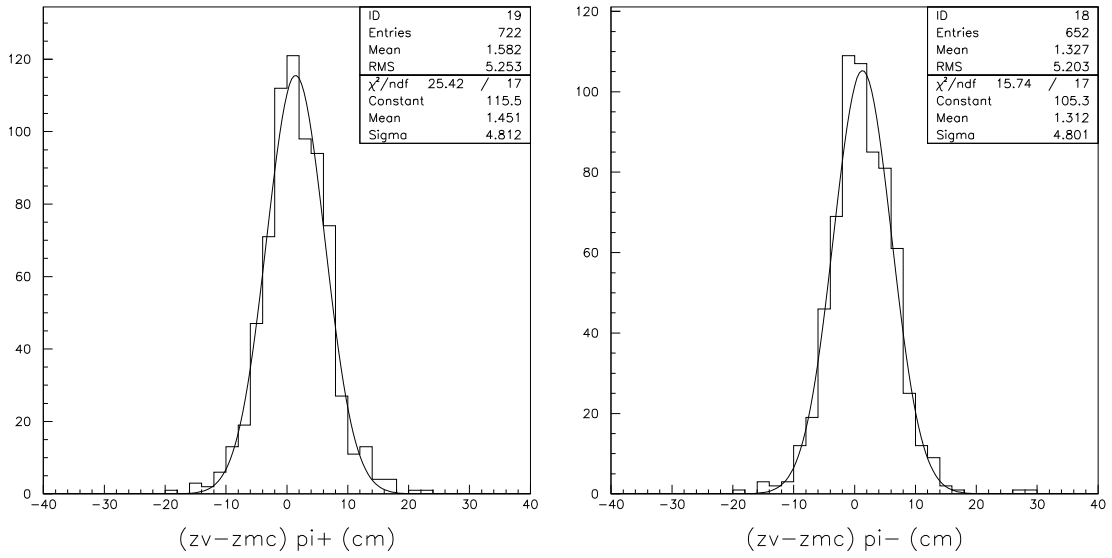

Figure 9.23: Fit of the vertex resolution in z (Be thin target, MC for NDC study, no solenoid field)

Detector	Number of reconstructed particles	particles type
MWPC	895	proton
NDC	5	π^+
NDC	878	π^-
NDC	9	μ^+
NDC	5	μ^-
NDC	866	π^+
NDC	8	proton

Table 9.9: Detector and particle type of the reconstructed particle in the vertex fit (Be thin target, MC for NDC study)

Type	Parameters	Fraction of the tracks (%)
NDC	Momentum not measured	13.7

Table 9.10: Reconstruction inefficiency for NDC tracks entering in the vertex (Be thin target, MC for NDC study)

NDCs reconstruction and vertex performances with the solenoid field

For the NDC study we also produced Monte Carlo data with the solenoid field at $\theta = 150$ mrad $\varphi = 0$. Over 1000 Monte Carlo events 943 have been reconstructed with a vertex and 786 events have three reconstructed particles. The detector and particle type of the 2661 reconstructed particles is given in Table 9.9. We get no TPC type particles. This is understandable since with the solenoid field they will curve in the TPC and not pass anymore the selection criteria of the track fit.
The NDC protons have been identified as beam particles.
The reconstruction inefficiency fractions for the tracks entering the vertex fit are given in Table 9.10. Tracks entering in the inefficiency table have been excluded from the plots.
The χ^2/ndf distribution of the track fit is given in Figure 9.24 with a cut on its value at 20. Its shape looks reasonable showing the quite good track reconstruction we have. In the measurements we present below we have used tracks for which χ^2/ndf <20.
The $\chi^2_k(filter)$ shape is shown in Figure 9.25 with a cut on its value at 20. Its shape is not satisfactory. In the measurements presented below we have applied a cut $\chi^2_k(filter) < 20$. The cuts on the χ^2/ndf, the $\chi^2_k(filter)$, and the selection on NDC tracks with momentum measured as well as three particles reconstructed results in 660 entries in the pull plots. This gives an overall effienciency for recontruction and vertex fit in the NDCs of 66%.
Results of the fit of the pulls for the position are summarised in Table 9.11 when three particles are reconstructed. For the position in x and y the σ remains too large. The pulls in z have a more reasonable σ but a $\sim$ -2 shift.
Results of the fit of the pulls for the momentum are summarised in Table 9.12 when three particles are reconstructed. The momentum reconstruction at the vertex is not completly satisfactory and there are differences between the pulls for the π^- and π^+.
Fit results of the vertex resolution are given in Table 9.13 for three particles reconstructed. This give a resolution of $\sim$ 1 mm in x and y and of $\sim$ 5 cm in z.

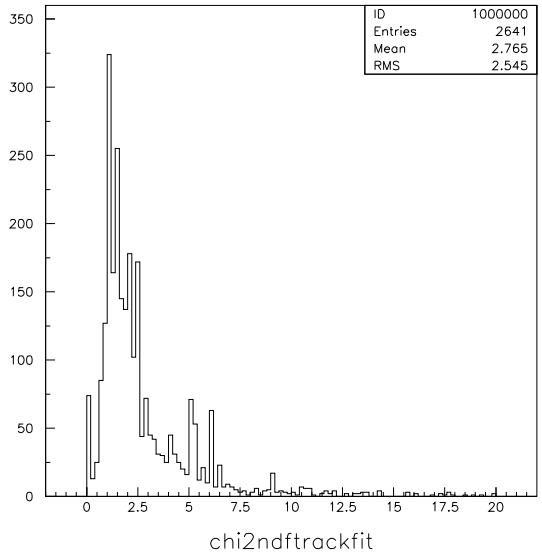

Figure 9.24: χ^2/ndf of the track fit (Be thin target, MC for NDC study), $\chi^2/ndf < 20$

	Pull x (π^-)	Pull x (π^+)	Pull y (π^-)	Pull y (π^+)	Pull z (π^-)	Pull z (π^+)
Mean	-0.04263	-0.04757	0.06958	0.02754	0.1988	0.1536
σ	1.698	1.689	1.531	1.488	1.267	1.176

Table 9.11: Fit results of the pulls for position (position in cm) at the vertex (Be thin target, MC for NDC study)

	Pull p_x (π^-)	Pull p_x (π^+)	Pull p_y (π^-)	Pull p_y (π^+)	Pull p_z (π^-)	Pull p_z (π^+)
Mean	0.0423	-0.7022	-0.01523	0.4799	-0.02424	-0.6047
σ	0.8676	0.7960	1.694	0.9059	0.6638	0.5881

Table 9.12: Fit results of the pulls for momentum (momentum in GeV/c) at the vertex (Be thin target, MC for NDC study)

	x (π^-)	x (π^+)	y (π^-)	y (π^+)	z (π^-)	z (π^+)
Mean	0.003275	0.001972	0.00541	0.002748	0.6454	0.5847
σ	0.07648	0.07776	0.07288	0.07072	5.040	4.840

Table 9.13: Fit results of the vertex resolution (cm) (Be thin target, MC for NDC study)

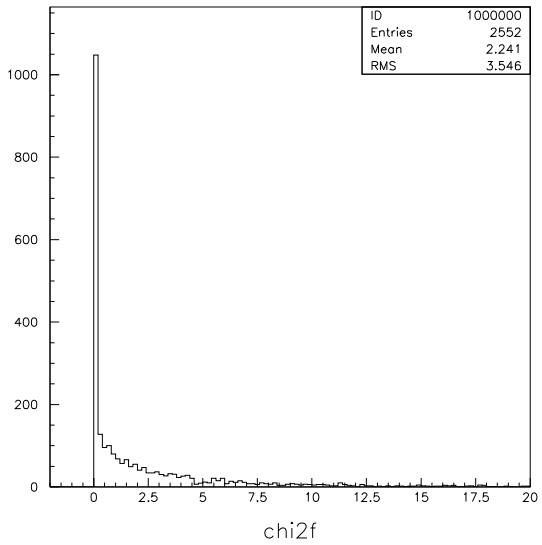

Figure 9.25: $\chi^2_k(filter)$ distribution (Be thin target, MC for NDC study), $\chi^2_k(filter) < 20$

Type	Parameter	Fraction of the tracks (%)
TPC	Momentum not computed at refSurf	0.05
TPC	Negative flag	7.96
NDC	Momentum not measured	34.0

Table 9.14: Reconstruction inefficiency for TPC and NDC tracks entering in the vertex (Be thin target, 12 GeV/c data

9.3 Vertex distribution for thin and thick Be targets

9.3.1 Vertex distibution for Be thin target

A test has been made on HARP 2002 12 GeV/c beam momentum data with a thin (5% λ_{int}) Be target. Over 5000 events, 4816 have been reconstructed with a vertex. The number of particles used for the vertex is shown in Figure 9.26. In most of the cases the vertex contains one reconstructed particle per event.

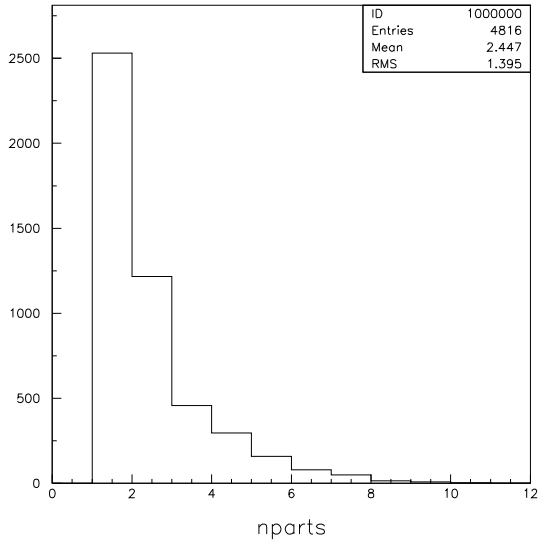

Figure 9.26: Number of recontructed particles used for the vertex fit (Be thin target, 12 GeV/c data)

About 47% (2285 in total) of the events have more than one reconstructed particle. This is mainly due to the trigger purity. In order to compare it with the exact trigger purity the number of DOWNSTROBE events in this sample has to be evaluated. We can also expect a slight inefficiency of the reconstruction algorithms leading to a loss of some tracks. Reconstruction inefficiency fractions for the track reconstructed are given in Table 9.14. The number of NDC type tracks for which module 1 was hit and the momentum not measured is quite high. We can expect to reduce this number only by improving the track matching efficiency between module 1 and module 2. However, module 1 suffers from beam saturation effects and the presence of multiple hits decreases the efficiency of the pattern recognition algorithms, therefore decreasing the probability to reconstruct a 3D segment or a plane segment (a wire per chamber, all wires being in the same plane) and to measure the momentum. Unfortunatly the constraint on the reference surface for accepting a track in the vertex is exactly in the spatial region where we expect the NDC track reconstruction

being less efficient as explained previously. The χ^2/ndf distribution of the track fit with a cut at $\chi^2/ndf < 50$ is given in Figure 9.27. It presents a quite long tail as compared to the data we reconstructed in the

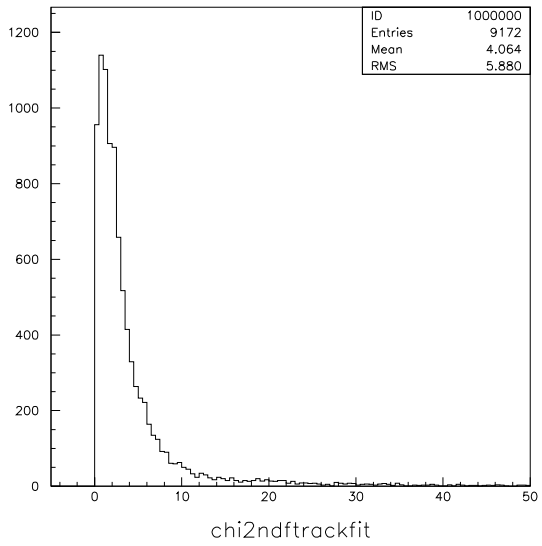

Figure 9.27: χ^2/ndf distribution of the track fit (Be thin target, 12 GeV/c data), $\chi^2/ndf < 50$

Monte Carlo simulation. For the vertex position plot we will use only tracks for which $\chi^2/ndf < 50$.
The $\chi^2_k(filter)$ presents a very long tail as shown in Figure 9.28 with a cut at $\chi^2_k(filter) < 100$. For the vertex position plots we kept the cut at this value to cancel part of the tail without loosing too much statistics.

Figures 9.29, 9.30 and 9.31 show the number of tracks as a function of the vertex position when at least two tracks are reconstructed. At first look from the distribution of the vertex position we can observe that events for which the MWPC particle is included in the vertex fit, will help to constrain the vertex position in the target volume in x and y, whereas in z a TPC track would also be required. In z the distribution is larger than the 2.03 cm of the length in z of Be 5% λ_{int} target and not centered at zero as expected for this target. This gives a hint of the resolution we can obtain in z. Distribution in x and y reflect quite well the beam position, which is not necessarily centered. Particles will also interact in the material around the target. The distribution in the z direction is not showing the expected distribution (peaked at a given value). There is good chance that in fact either the seed state value or the expansion point value that we have chosen is pulling the vertex position in a direction which is too much dependent on these input parameters. To get rid of this dependence a solution can be provided by using as expansion point the minimum approach point to the beam track but some study has to be done here to find which kind of seed state and expansion point could help to get a vertex distribution which does not depend on these parameters.

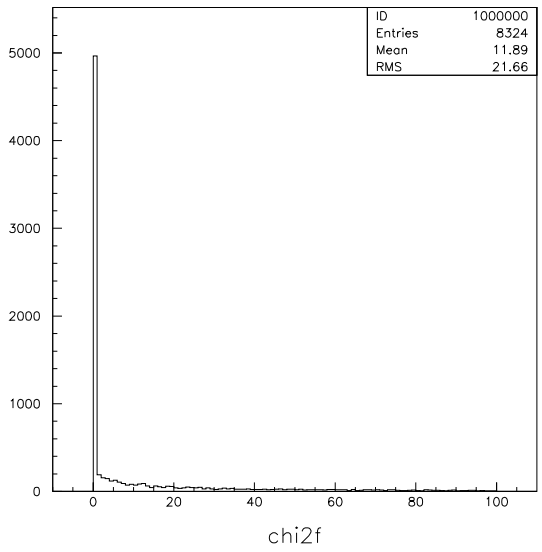

Figure 9.28: $\chi^2_k(filter)$ distribution (Be thin target, 12 GeV/c data), $\chi^2_k(filter) < 100$

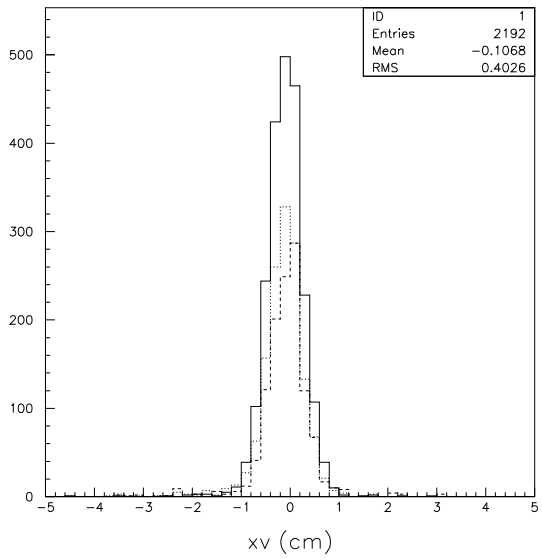

Figure 9.29: Vertex position (cm) in x (Be thin target, 12 GeV/c data), bold MWPC, dash TPC, dot NDC

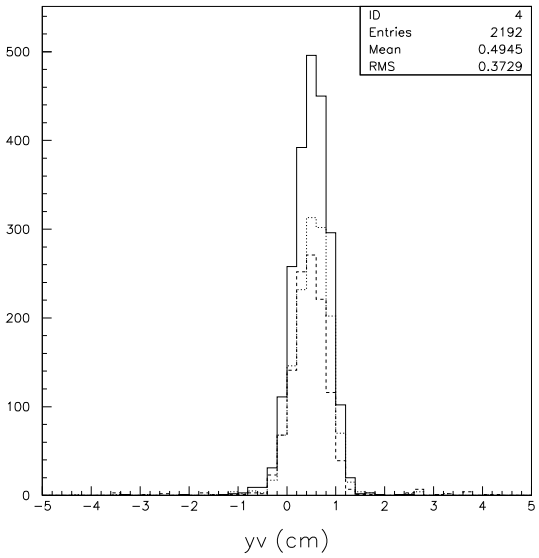

Figure 9.30: Vertex position (cm) in y (Be thin target, 12 GeV/c data), bold MWPC, dash TPC, dot NDC

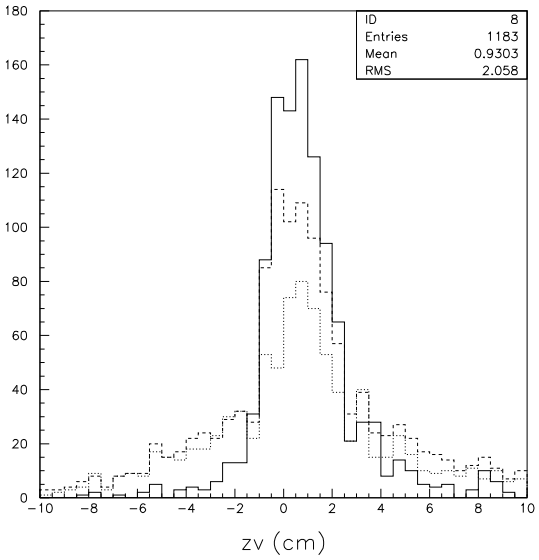

Figure 9.31: Vertex position (cm) in z (Be thin target, 12 GeV/c data), bold TPC, dash MWPC, dot NDC

Type	Parameter	Fraction of the tracks (%)
NDC	Tracks with a negative χ^2/ndf	0.02
TPC	Momentum not computed at refSurf	0.12
TPC	Negative flag	8.56
NDC	Momentum not measured	44.1
TPC	Negative D_{00} and D_{11}	0.02

Table 9.15: Reconstruction inefficiencies for TPC and NDC tracks entering in the vertex (Be thick target, 12 GeV/c data

9.3.2 Vertex distribution for Be thick target

Data taken at 12 GeV with the 100% λ_{int} Be target have also been studied. Over 5000 events, 4917 events are reconstructed with the vertex. This is of the same order as for the thin target with a sligh higher efficiency for vertex reconstruction but it is difficult to say here whether this is due to the fact that in the thick target case more particles enter the reference surfaces. Within these events 3906 events have at least two reconstructed particles ($\sim$ 79%). The reconstruction inefficiency fractions are given in Table 9.15. Particles entering in the reconstruction inefficiency table have been excluded from the vertex position plots. The number of particles used for the vertex reconstruction is shown in Figure 9.32. The χ^2/ndf distribution

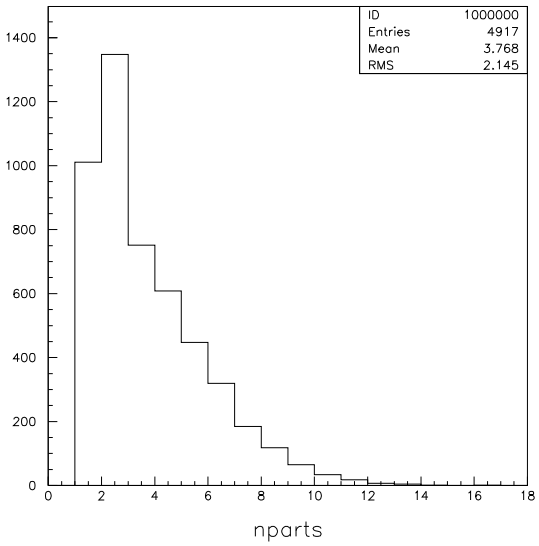

Figure 9.32: Number of reconstructed particles used for the vertex fit (Be thick target, 12 GeV/c data)

of the track fit with for $0 < \chi^2/ndf < 50$ is given in Figure 9.33. For the vertex position plots we used tracks with a χ^2/ndf below 50.

The $\chi^2_k(filter)$ present a very long tail as shown in Figure 9.34 with a cut at $\chi^2_k(filter) < 300$. For the vertex position plots we kept this loose cut to cancel part of the tail without loosing too much statistics.

The position of the vertex is shown in Figures 9.35, 9.36 and 9.37 for at least two tracks in the vertex. The same remarks can be made as for the thin target case concerning the shape of the distribution and the vertex resolution in z except that we observe vertices in the 40.6 cm long target as expected. As discussed earlier,

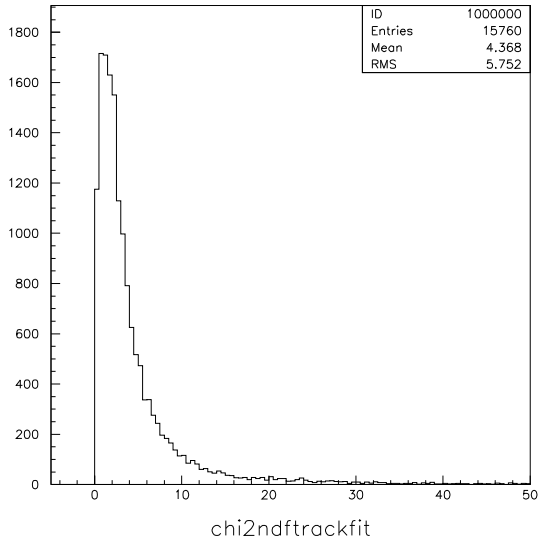

Figure 9.33: χ^2/ndf distribution of the track fit (Be thick target, 12 GeV/c data), $0 < \chi^2/ndf < 50$

the vertex fit parameters will need to be optimised in order to obtain reconstructed vertex distributions that match the physics case without bias.

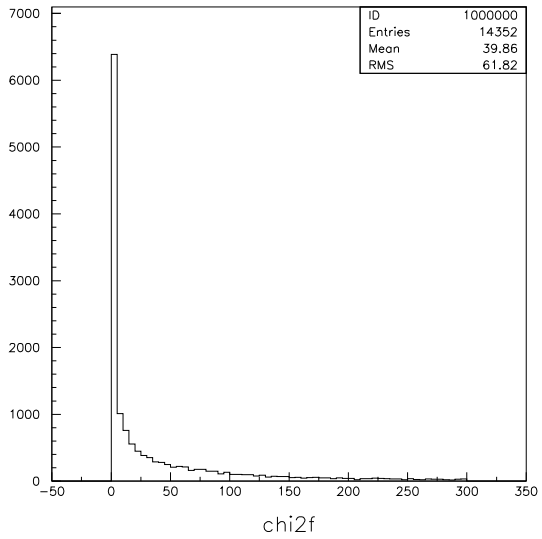

Figure 9.34: $\chi^2_k(filter)$ distribution (Be thick target, 12 GeV/c data), $\chi^2_k(filter) < 300$

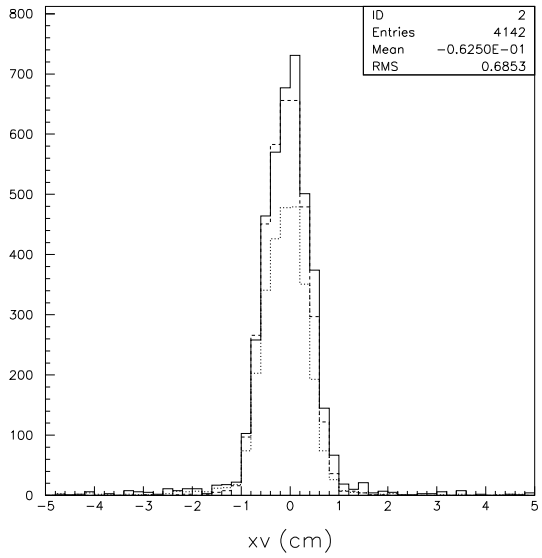

Figure 9.35: Vertex position (cm) in x (Be thick target, 12 GeV/c data), bold TPC, dashed MWPC, dotted NDC

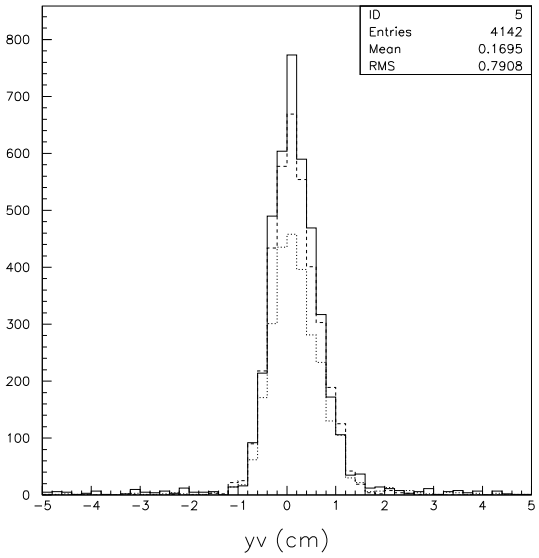

Figure 9.36: Vertex position (cm) in y (Be thick target, 12 GeV/c data), bold TPC, dashed MWPC, dotted NDC

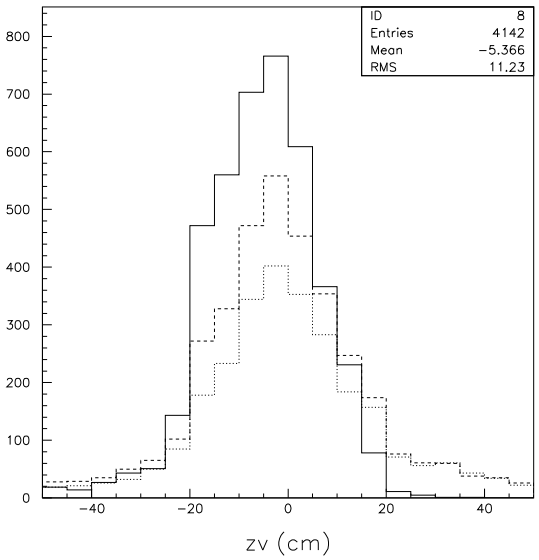

Figure 9.37: Vertex position (cm) in z (Be thick target, 12 GeV/c data), bold TPC, dashed MWPC, dotted NDC

Part V

Neutral strange particle production: K^0_S

Chapter 10

Invariant mass reconstruction efficiency (Monte Carlo)

We have used Monte Carlo data to estimate the reconstruction efficiency for the invariant mass computed from particles seen by the NDCs as a first order. A hadron production generator will allow us to obtain an estimate of the number of K^0_S that we are able to reconstruct in HARP. Some detector alignment efforts are still on-going and a better resolution for the invariant mass reconstruction is expected in the future.

10.1 Monte Carlo study using pions with defined kinematic

Monte Carlo data have been produced, using the 'exclusive' (see Appendix A) generator. This permits to test the performance of the invariant mass reconstruction algorithm. The generator does not allow forced secondary interactions for other particle than a proton or a charged pion. Therefore we have chosen as beam particle a 3 GeV/c proton. If a secondary particle has for 3D polar angles in the laboratory $\theta_1 = 150$ mrad and $\varphi_1 = 0$ rad, we can reconstruct it in the NDCs as demonstrated in the vertex study. The relation between θ_1 and the momentum of the parent K^0_S is given by Equation 10.1 for an angle $\theta^*_1 = \pi/2$ rad in the rest frame of the K^0_S.

$$tan(\theta_1) = \frac{|| \overrightarrow{p}^*_1 || \cdot c}{|| \overrightarrow{\beta}_{CM} || \cdot \gamma_{CM} \cdot E^*_1} \tag{10.1}$$

where $\overrightarrow{\beta}_{CM}$ is the Lorentz velocity and γ_{CM} the Lorentz factor of the K^0_S in the laboratory frame. $\overrightarrow{p}^*_1$ and E^*_1 are the momentum and the energy respectively, of the secondary pion in the K^0_S rest frame. The solution of Equation 10.1 gives for the momentum of the K^0_S in the laboratory, a value of ~ 2.73 GeV/c.
To create pions coming from a K^0_S decay we have proceeded as follows. A secondary π^+ is created in the K^0_S rest frame (we define here the K^0_S momentum being the one of the beam proton) with $\varphi^*_1 = 0$ and $\theta^*_1 = \pi/2$ rad. Its momentum in the K^0_S rest frame is given by the kinematic of two-body decay (see Appendix C). A secondary π^- is created in the K^0_S rest frame back to back from the π^+. Momentum and energy of the charged pions are then calculated in the laboratory frame.
Such 1000 fake K^0_S events have been created. For each event, the reconstructed particles are retrieved and $\frac{n\cdot(n-1)}{2}$ pairs of particles are built, n being the total number of reconstructed particles in the event. Each track of the pair is then propagated to $z = 0$, where the momentum is computed, as an estimate of the initial momentum. We have chosen this simple approximation in order to be independent of the vertex

Number of Monte Carlo events	Number of Monte Carlo particles	Particle type
19	1	beam proton
976	3	proton, π^-, π^+
2	5	proton, π^-, π^+, μ^+, ν_μ
3	5	proton, π^-, π^+, μ^-, $\overline{\nu}_\mu$

Table 10.1: Monte Carlo particles generated, simulation for K^0_S study ('exclusive' generator)

Number of reconstructed events	Number of reconstructed particles	Number of pairs
30	2	1
97	3	3
453	4	6
367	5	10
46	6	15
7	7	21

Table 10.2: Reconstructed particles, simulation for K^0_S study ('exclusive' generator)

performance.
The invariant mass is then calculated assuming that all reconstructed particles are pions except for the particle who crossed the MWPCs which is assumed to be a proton.
Table 10.1 gives the number of Monte Carlo events and particles generated by the simulation. We can see from it that there is a contamination of $\mu^\pm$ for some events. It is a feature of the generator.
All the Monte Carlo events have been reconstructed. Such events contain at least two and less than eleven reconstructed particles.
Reconstructed particles for which the Monte Carlo information is not available are discarded.
Table 10.2 shows the number of reconstructed events with the corresponding number of reconstructed particles and pairs. We reconstruct more particles than the number of Monte Carlo particles in the event. There is no matching between the TPC and the NDCs on one hand. On the other one, segments of tracks reconstructed in different NDCs modules and not matched, produce more than one reconstructed particle.
We have selected pairs of reconstructed particles in the NDCs exclusively for the invariant mass plots. The number of pairs remaining after cuts on the reconstructed particles is given in Table 10.3. This gives a final

Cut	Selection criteria	Number of pairs (in total 7546)
1	reconstructed in the NDCs	1235
2	& extrapolated at $z = 0$	948
3	& momentum measured	878
4	& pairs of opposite charge particles	878
5	& pairs with corresponding Monte Carlo particles being $\pi^+\pi^-$	873

Table 10.3: Number of pairs and cuts for reconstructed particles, simulation for K^0_S study ('exclusive' generator)

efficiency of $\sim$ 87%. An acceptable value even if not entirely satisfactory since all simulated $\pi^-\pi^+$ from K^0_S decay should normally be reconstructed in the NDCs. It seems that we loose some particles which could not be extrapolated $z = 0$ or for which the momentum could not be measured. We can expect a better efficiency with the improvements in the extrapolation or momentum computation in the reconstruction.
The charge assignment efficiency is of 100% for this Monte Carlo sample.
The fit of the true (computed from Monte Carlo mass, energy and momentum) and reconstructed invariant masses for pairs with cuts one to five applied is given in Figure 10.1. The peak of the reconstructed

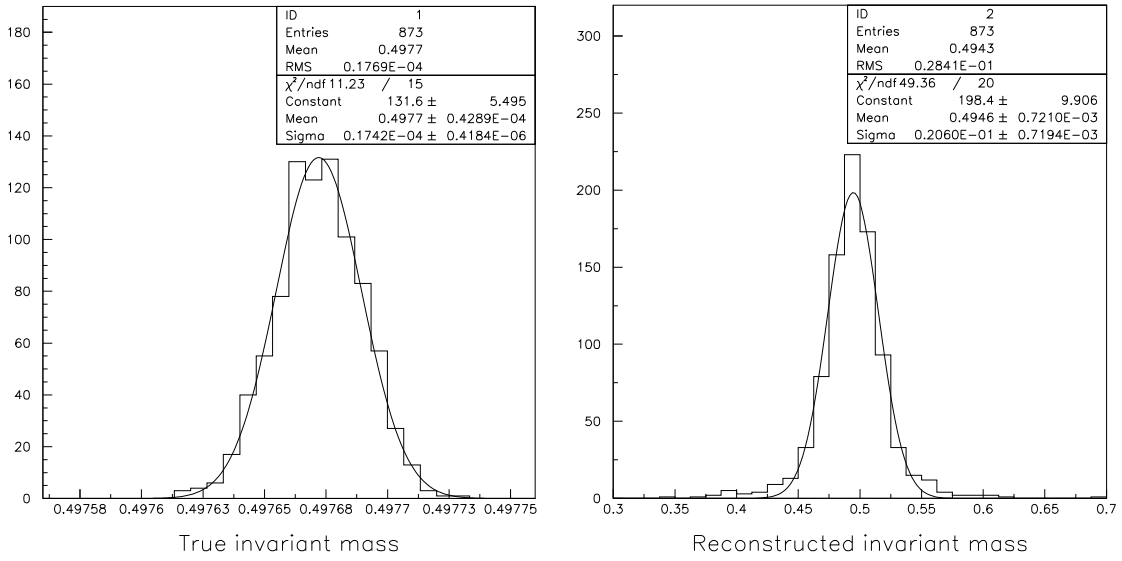

Figure 10.1: Fit of the true (left) and reconstructed (right) invariant mass (GeV/c^2) of opposite signs pions pairs reconstructed in the NDCs ('exclusive' generator)

invariant mass is at 494.3 MeV/c^2 and the standard deviation is of 28.41 MeV/c^2 giving thus an estimate of the invariant mass resolution we can obtain with the reconstruction. From this result we know that in a first approximation, both the tracking efficiency and the momentum estimate close to the vertex point are good enough to allow a K^0_S study in the NDCs for secondaries produced at a small θ angle and in absence of combinatorial pion background. The $\sim$ 3 MeV/c^2 shift between the true invariant mass and the reconstructed one is probably due to the fact that the energy loss while extrapolating the tracks to $z = 0$ is not taken into account.

10.2 Using the hadron generator QGSP

10.2.1 Over a sample of 10000 events

The hadron generator 'QGSP' has been designed to simulate the hadron production for medium energy (15-50 GeV) on light targets. This generator is a combination of the 'Quark Gluon String' model and the 'Precompound' model. The primary particle interacting in the nucleus is represented as a string with large momentum/energy transfer. To simulate the deexcitation of the nucleus the 'Precompound' model is applied. As a result low energy protons and neutrons are emitted. It has been used to produce Monte Carlo data with K^0_S events as in normal physics conditions.

Cut	Selection criteria	Number of pairs (total 126745)
1	reconstructed in the NDCs	20471
2	& extrapolated at $z = 0$	8115
3	& momentum measured	2819
4	& pairs of opposite charge particles	1413
5	& pairs with corresponding Monte Carlo particles being $\pi^-\pi^+$	354

Table 10.4: Number of pairs remaining and cuts for the reconstructed particles, simulation for K^0_S study ('QGSP' generator)

	q_1^{mc}=1 & q_1^{rec}=1	q_1^{mc}=1 & q_1^{rec}=-1	q_1^{mc}=-1 & q_1^{rec}=1	q_1^{mc}=-1 & q_1^{rec}=-1
q_2^{mc}=1 & q_2^{rec}=1	1242	76	30	763
q_2^{mc}=1 & q_2^{rec}=-1	74	9	1	33
q_2^{mc}=-1 & q_2^{rec}=1	16	0	0	2
q_2^{mc}=-1 & q_2^{rec}=-1	492	38	5	38

Table 10.5: Charges assignment for pairs remaining with cuts 1 to 3 applied, simulation for K^0_S study ('QGSP' generator)

In order to get a overview of the performance of the reconstruction and the invariant mass algorithm, we have produced a sample of 10000 Monte Carlo events for a 12 GeV/c proton beam on a 5% λ_{int} Be target. A total of 220 K^0_S are contained in this sample. A total of 8454 events was reconstructed. The number of pairs remaining after cuts on the reconstructed particles are given in Table 10.4. The charge assignment statistics is given in Table 10.5. We are left with $\sim$ 11% of pairs of opposite charge with a wrong charge assignment. This not negligible fraction will enter in the combinatorial $\pi^-\pi^+$ background.
The true and reconstructed invariant masses for pairs with cuts one to five applied are given in Figure 10.2.
We get a total of 338 pairs which have passed the cuts one to five and are coming from the same parent particle. The parent particle list is given in Table 10.6.
A fraction of $\sim$ 2% of the K^0_S events can be reconstructed in the NDCs with the cuts we have applied. Unfornutaly the signal is completly hidden by the combinatorial pion background.
Figure 10.3 shows the true invariant mass for pairs (cut one to five applied) which have as parent the same proton. We can distinguish a $\rho(770)^0$ resonance with no width in this invariant mass peak. First of all we should not expect a peak at the $\rho(770)^0$ mass if the parent particle is assigned to a proton. Furthermore,

Number of $\pi^-\pi^+$ pairs in the NDCs	Parent
1	$\rho(770)^0$
13	η
4	K^0_S
2	$\eta(958)$'
318	proton

Table 10.6: Parent particle list of pairs with the same parent, cuts 1 to 5 applied ('QGSP' generator)

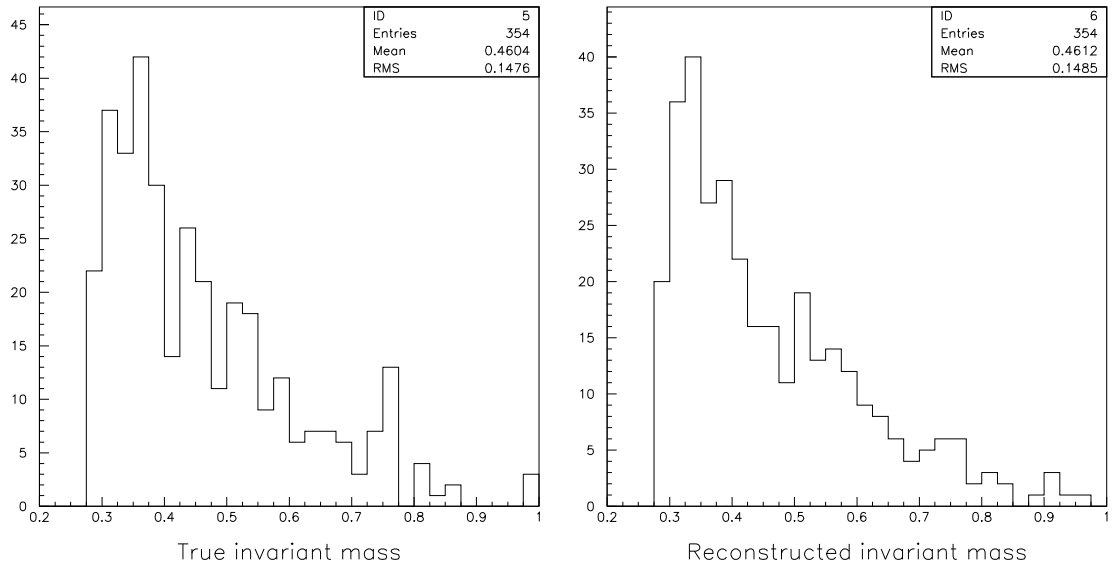

Figure 10.2: True (left) and reconstructed (right) invariant mass (GeV/c^2) of opposite charge pions pairs in the NDCs remaining after cuts ('QGSP' generator)

concerning the $\rho(770)^0$ width, a check on the invariant mass peak with the parent particle being a $\rho(770)^0$ gives also the same behaviour as shown in Figure 10.4. This generator feature comes from the string hadronization of the quark-gluon string model [56] in the generator. Investigations are on-going to correct it.

Figure 10.5 shows the true and the reconstructed invariant masses for pairs in the NDCs with cuts one to five applied and with the same K^0_S parent. There is a large difference for the invariant mass value in the four remaining events. Still there is hope to recognize some of the K^0_S with more statistics and subtracting the combinatorial $\pi^-\pi^+$ background using Monte Carlo data.

Since the combinatorial $\pi^-\pi^+$ signal is the most important background we made a further check on the origin of the parent proton itself and it appears that for all the cases the parent proton is a secondary produced at the target. Apparently it reinteracts and produces charged pions. We have to assume this as being the background from the interaction in the target.

As an example of what we should expect from subtraction of physics data by Monte Carlo we have made the exercise on this sample. Figure 10.6 shows the reconstructed invariant mass for pairs with cuts one to five applied, where the pairs coming from the same parent K^0_S have been removed.

By subtracting the right plot in Figure 10.2 by the plot in Figure 10.6 we get the right plot in Figure 10.5. By looking at the excess of events for values of the invariant mass comprised between 0.450 and 0.550 GeV/c^2 and if we increase the statistics we should be able to see a signal from K^0_S decay.

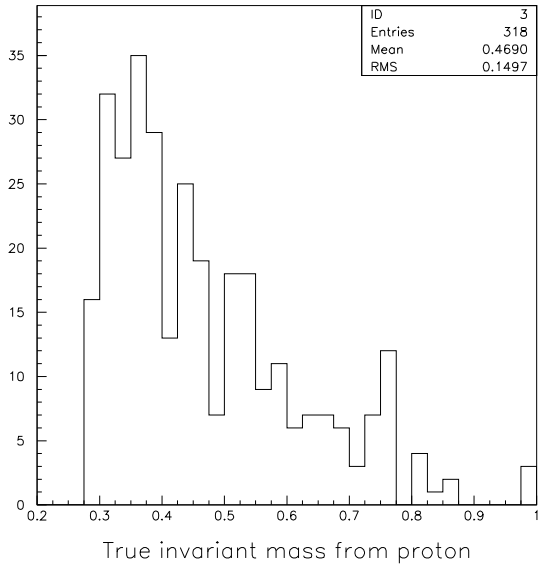

Figure 10.3: True invariant mass (GeV/c^2) for pairs with cuts 1 to 5 applied with the same parent proton ('QGSP' generator)

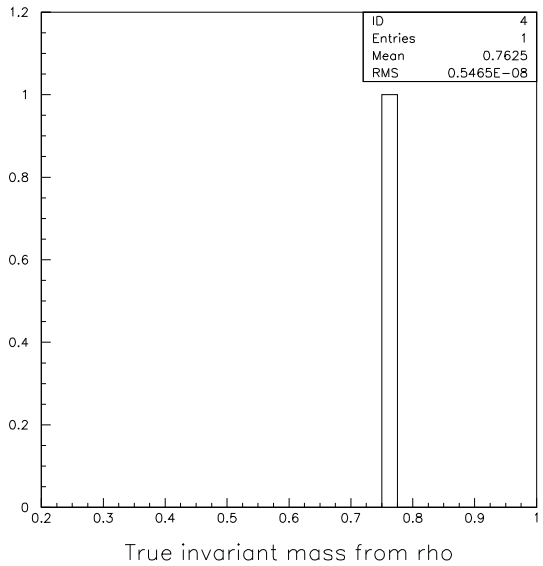

Figure 10.4: True invariant mass (GeV/c^2) for pairs with cuts 1 to 5 applied and with the same $\rho(770)^0$ parent particle ('QGSP' generator)

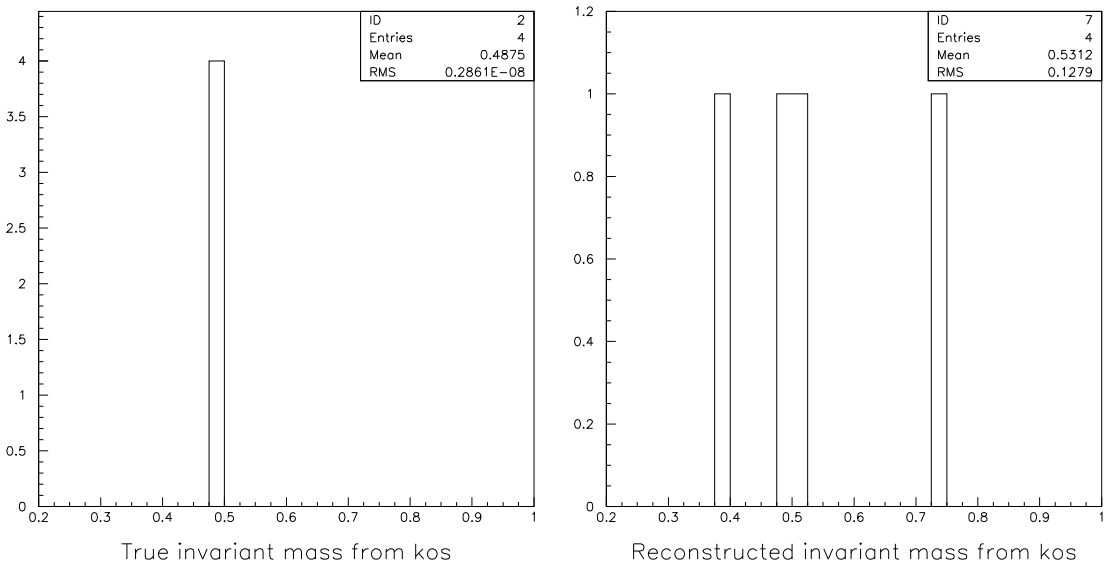

Figure 10.5: True (left) and reconstructed (right) invariant mass (GeV/c^2) for pairs with cuts 1 to 5 applied and with the same K^0_S parent ('QGSP' generator)

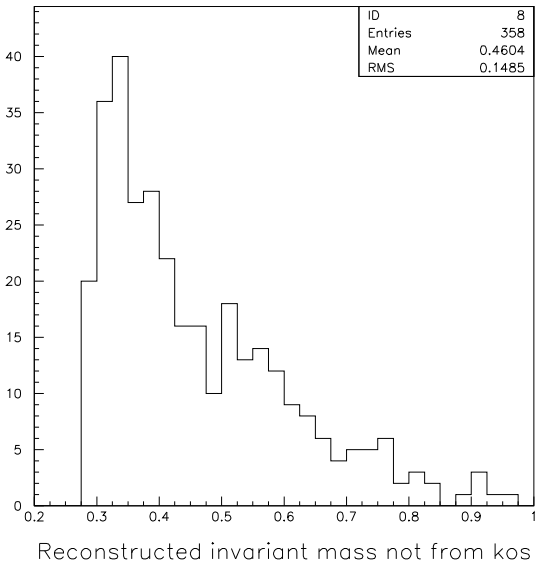

Figure 10.6: Reconstructed invariant mass (GeV/c^2) for pairs, cuts 1 to 5 applied. Pairs coming from the same parent K^0_S have been removed ('QGSP' generator)

Total number of events processed	600 000
Number of events retrieved	432711
Number of events reconstructed	238620

Table 10.7: Processing and reconstruction efficiencies for Monte Carlo data ('QGSP' generator)

Cut	Selection criteria	Number of pairs (total 747705)
1	reconstructed in the NDCs	747705
2	& modules downstream fired	361297
3	& extrapolated at $z = 0$	190182
4	& momentum measured	176073
5	& χ^2/ndf of the track fit < 20	163315
6	& $\sigma_p/p < 40\%$	155548
7	& $0.2 <$ p < 12.0 GeV/c	145266
8	& pairs of opposite charge particles	72489
9	& pions pairs	18335
10	& $\|\|\overrightarrow{r_1} - \overrightarrow{r_2}\|\| < 20$ cm at $z = 0$	17805

Table 10.8: Number of pairs and cuts on the reconstructed particles (Monte Carlo 'QGSP' generator)

10.2.2 High statistics study with one million events

A sample of one million Monte Carlo events has been generated using the 'QGSP' generator and a proton beam of momentum 12.0 GeV/c over a Be 5% λ_{int} target. The efficiencies for the events processing and reconstruction are given in Table 10.7. The events which are reconstructed have at least two and at most ten reconstructed particles. The reconstruction efficiency for such events is low ($\sim$ 55%). Due to a format error in reading the mDSTs many events could not be read.
The efficiency for the pair reconstruction is given in Table 10.8.

The pairs are all reconstructed in the NDCs, because, due to an unexpected feature of the format we use, the Monte Carlo information of the MWPC track is lost.
The cut on the χ^2/ndf of the track fit has been estimated from the distribution in Figure 10.7 and from the distribution we obtain for the Be 5% data sample at 12 .0 GeV/c.
Distributions for both Monte Carlo and data sample are for pairs with cuts one to four in Table 10.8 applied. The distribution for the data sample is reported in the next chapter.

The cut on the relative error on the momentum σ_p/p has been estimated from the distribution in Figure 10.8 and from the distribution in the data sample (see next chapter). These distributions have been obtained (Monte Carlo and data) from pairs with cuts number one to five applied.

The cut on the distance between the two particles extrapolated at $z = 0$ has been estimated from what we get from pairs coming from the same parent K^0_S (plot left in Figure 10.9), and the distribution obtained (plot right) for all pairs. Cuts one to nine have been applied in both plots. Distribution of the distance between the two particles at $z = 0$ for the data sample is compatible with this cut and reported in the next section.

The left plot in Figure 10.10 shows the invariant mass for pairs with cuts 1 to 10 applied. The right plot shows the invariant mass distribution where pairs coming from the same K^0_S parent have been removed.

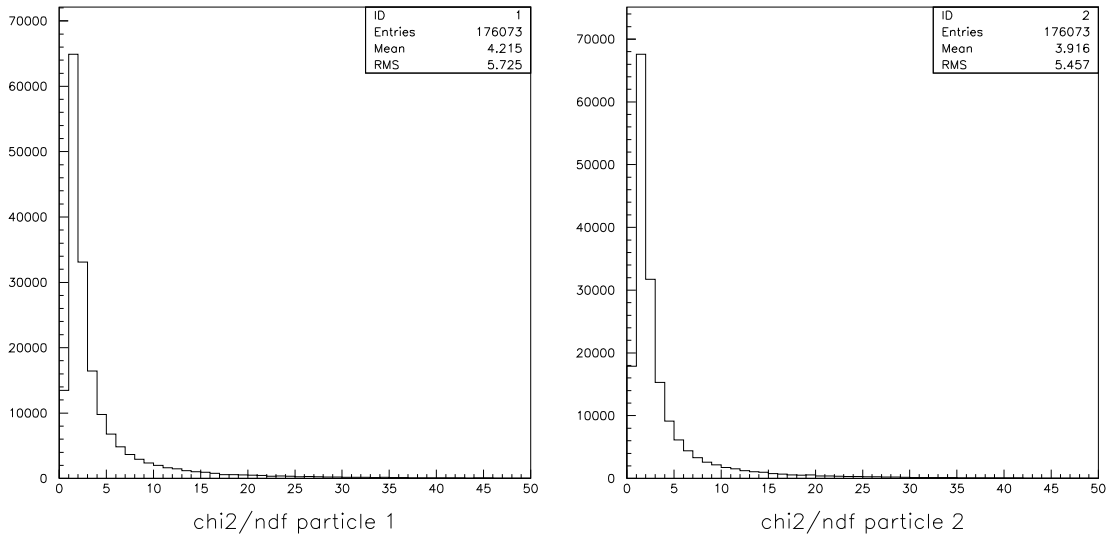

Figure 10.7: χ^2/ndf of the track fit for the first (left) and the second (right) particle in pairs, cuts 1 to 4 applied (Monte Carlo 'QGSP' generator)

Figure 10.11 shows reconstructed invariant mass for pairs coming from the same parent K^0_S. The number of K^0_S for which we are able to reconstruct the decay products represents 12% of the K^0_S present (in total) in our Monte Carlo sample. This leave us with a better K^0_S reconstruction efficiency compared to the small Monte Carlo sample using the same generator. It is difficult to understand exactly why we get such a different number since the reconstruction and the generator haven't changed. Nevertheless, there is a noticable difference for the cuts 'extrapolated at z=0' and 'momentum measured' between mini Data Summary Tape (mDST) and iDST format (see Appendix **??**) that could be responsible for this feature. In the iDST case, we were controlling that the Kalman extrapolator could perform the measurement at $z = 0$ and rejecting events for which it was not the case. In the mDST case we control that the vertex position in x and y is not equal to zero since no information on the extrapolator is available. Concerning the cut 'momentum measured' if we retrieve the same information for both formats we should not expect a difference. If it is statistical fluctuations, one has to understand it running several time the generator on the same reconstruction.

The invariant mass distribution which contains no pion pairs from the same parent K^0_S will serve as an estimate of the combinatorial pion background. By subtracting the invariant mass distribution obtained in our data sample by the Monte Carlo distribution of the combinatorial background reweighted by a factor $R^i_{DATA/MC}$ per bin i we should get the number of K^0_S as follows:

$$N^i_{K^0_S} = N^i_{DATA} - R^i_{DATA/MC} \times N^i_{MC}$$

If the Monte Carlo reproduces well the physics and if there is no systematics introduced by the difference in the reconstruction between Monte Carlo and data (e.g alignement or detector simulation) we should expect this number being close to zero outside the K^0_S mass region and positive if a K^0_S signal can be extracted in the K^0_S mass region.

By using the same cuts for the data and Monte Carlo sample and if we assume the same reconstruction efficiency, we should expect the same distribution outside of the K^0_S invariant mass region. From what we obtain for the Monte Carlo (see Table 10.8) and the data it is clear that one would have to compute precisely

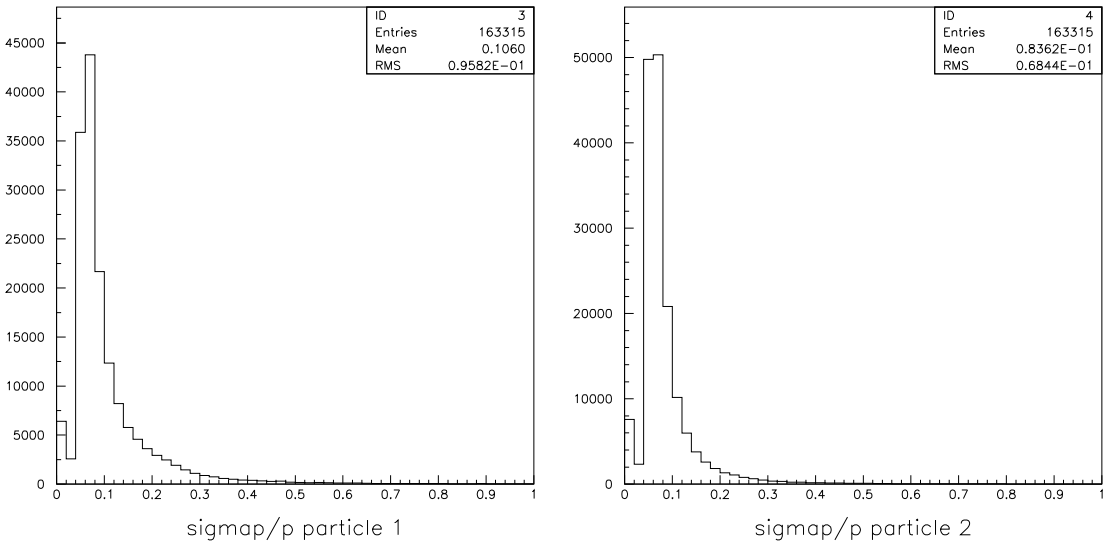

Figure 10.8: σ_p/p of for the first (left) and the second (right) particle in pairs, cuts 1 to 5 applied (Monte Carlo 'QGSP' generator)

the reconstruction efficiencies for the tracking in the NDCs in order to scale properly the Monte Carlo to the data.
However concerning the tracking efficiency one can assume that it will be constant as a function of momentum above 2.5 GeV/c and as a function of θ_x angle for 50 mrad $< |\theta_x| <$ 150 mrad as shown in Figures D.1 (in Appendix D). If we look at the momentum (see Figure 10.12) for pairs (cut one to ten applied) with the same K^0_S parent we can see that we would suppress a large part of the K^0_S signal when selecting daughters with momentum above 2.5 GeV/c.
The same can be said for θ_x angle (see Figure 10.13) where a cut would suppress statistics and increase the risk to bias our K^0_S sample.

One cannot estimate the pion identification efficiency from Monte Carlo data because the simulation of the particle identification detectors is not fully implemented. In the Monte Carlo, the pion identification is done while looking at the true particle, while in the data the particle identification detectors are used. The pion correction factor for pion identification efficiency and purity as a function of the track type and the momentum are assumed to be flat (see Appendix E) so we do not expect the invariant mass distribution to depend on it.
We can expect a slight difference in the shape for the invariant mass distribution between Monte Carlo and data due the hadronisation model of the generator.
As an exercise we show for this sample how we compute the scaling factor $R^i_{DATA/MC}$ for the Monte Carlo distribution before subtraction from the data sample.
Assuming that, in absence of K^0_S decay or other resonance, the combinatorial background has an exponential shape. As we can see from the plots in Figure 10.14, in the region 400-475 MeV/c^2 the exponential curve is not reproduced. This does not seem to be due to a statistical fluctuation since the shape does not change while increasing the statistics (see Figure 10.6 for comparison). Furthermore in the region 475-525 MeV/c^2 we get a excess of events as it would be for pions from the same parent K^0_S. Unfortunatly they are flagged by the Monte Carlo generator as particles coming from the same parent proton. It is believed that it is a

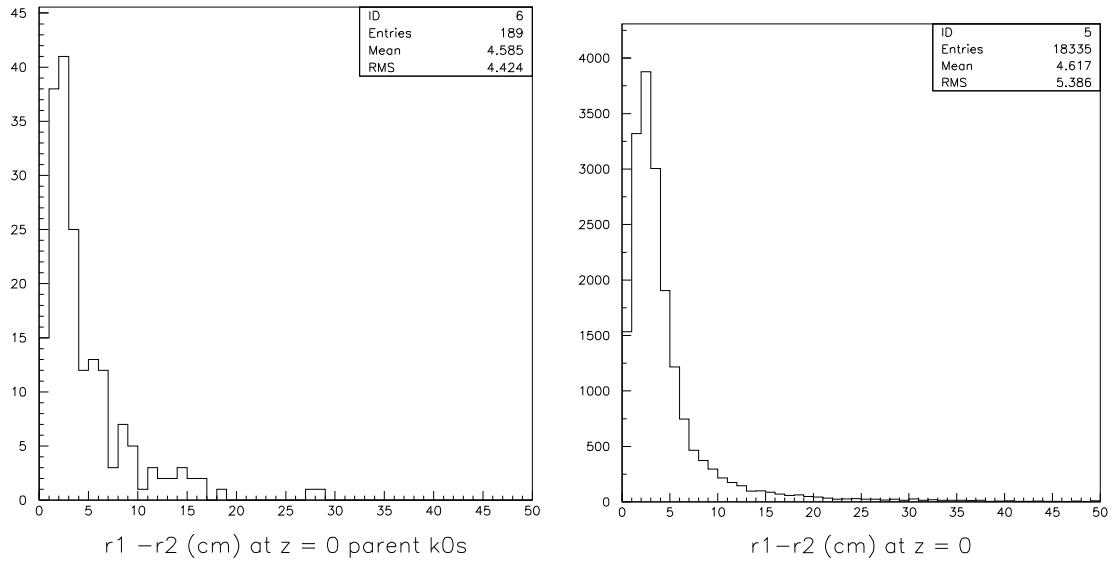

Figure 10.9: Distance between the two particles extrapolated at $z = 0$ for pairs, cuts 1 to 9 applied, with the same K^0_S parent (left) or all pairs (right) (Monte Carlo 'QGSP' generator)

feature of the generator since we already saw this trend in the small Monte Carlo sample in the case of the $\rho(770)^0$, where we also see an excess of events in the parent proton sample at the $\rho(770)^0$ mass. If we have a look now at the invariant mass without doing any selection on the parent particle and we try to fit the region outside the K^0_S invariant mass (we have chosen the region below 400 MeV/c^2 and above 600 MeV/c^2) to an exponential (see plots in Figure 10.15) by computing the ratio $R^i_{DATA/MC}$ of the side-band function obtained this way f^i_{SB} by the function obtained from the Monte Carlo curve with no K^0_S parent $f^i_{MC(0K^0_S)}$ we should get a scale factor per bin around one. Figure 10.16 gives the value for this ratio $R^i_{DATA/MC}$. As we can see the regions below 400 MeV/c^2 and 600 MeV/c^2 have a quite different contribution to the ratio. All the fits have been computed for a value of the invariant mass above 360 MeV/c^2.
As a proof of work of this method, Figure 10.17 gives the shape for the invariant mass distribution after removal of the combinatorial pion background. Even if we know that we have some K^0_S in our Monte Carlo sample it is not possible to achieve our goal and select a K^0_S signal for the resulting plot after background subtraction. However one can make an estimate of the number of K^0_S produced in the region of the invariant mass comprised between 460 and 560 MeV/c^2 as follows:

$$N_{K^0_S} = \frac{1}{\varepsilon} \times \frac{N - f_{bkg}}{N_p^{inc}}$$

where ϵ is our efficiency for K^0_S reconstruction. It is equal to:

$$\varepsilon = \frac{N^{rec}_{K^0_S}}{N^{tot}_{K^0_S}}$$

$N^{rec}_{K^0_S}$ is the number of K^0_S reconstructed in this region and $N^{tot}_{K^0_S}$ the total number of K^0_S generated.
N is the number of event selected in this region.

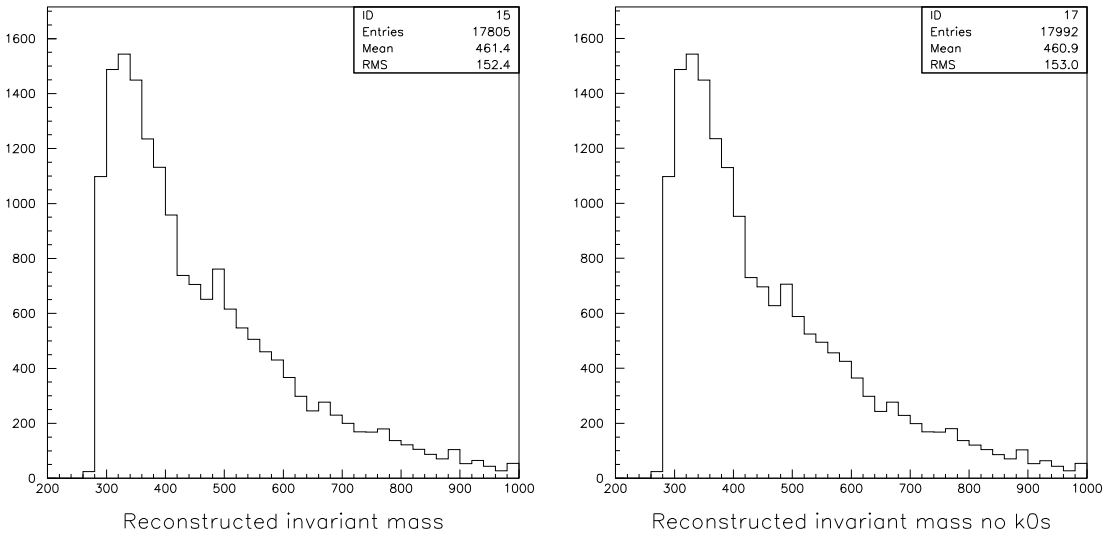

Figure 10.10: Invariant mass (MeV/c^2) for pairs, cuts 1 to 10 applied, for all pairs (left) and pairs not coming from the same parent K^0_S (Monte Carlo 'QGSP' generator)

$N^{tot}_{K^0_S}$	1540
$N^{rec}_{K^0_S}$	187
f_{bkg}	3049 $\pm$ 0.24
N^{inc}_p	432711
N	2855 $\pm$ 53

Table 10.9: Numbers relevant for the calculation of the number of K^0_S events

f_{bkg} is the number of background events in the region selected. This number is obtained from the exponential fit we get in Figure 10.15.
N^{inc}_p is the number of incident protons on the target. It can be estimated from the number of events that we can reconstruct.
Table 10.9 gives the different values we get for this Monte Carlo sample. The resulting number of K^0_S is equal to:

$$N_{K^0_S} = (-3.69 \pm 1.00) \cdot 10^{-3}$$

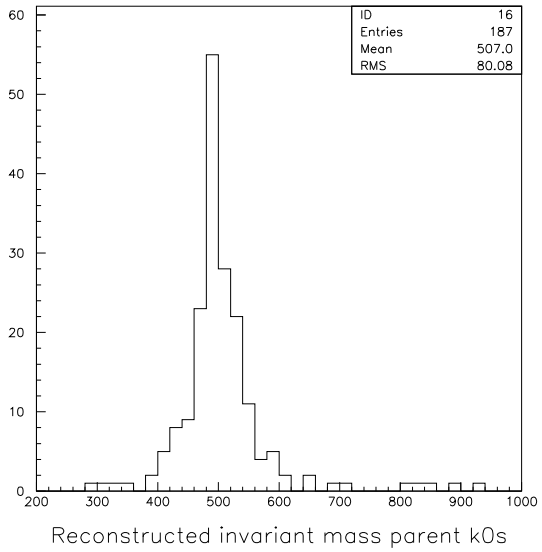

Figure 10.11: Invariant mass (MeV/c^2) for pairs coming from the same K^0_S parent, cuts 1 to 10 applied (Monte Carlo 'QGSP' generator)

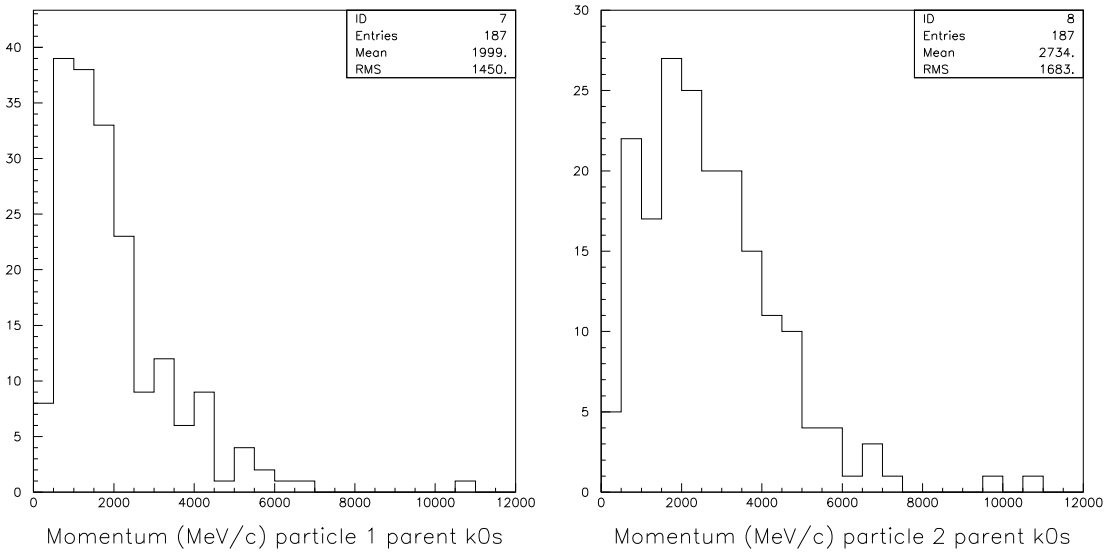

Figure 10.12: Momentum for the first (left) and the second (right) particle in pairs with the same parent K^0_S, cuts 1 to 10 applied (Monte Carlo 'QGSP' generator)

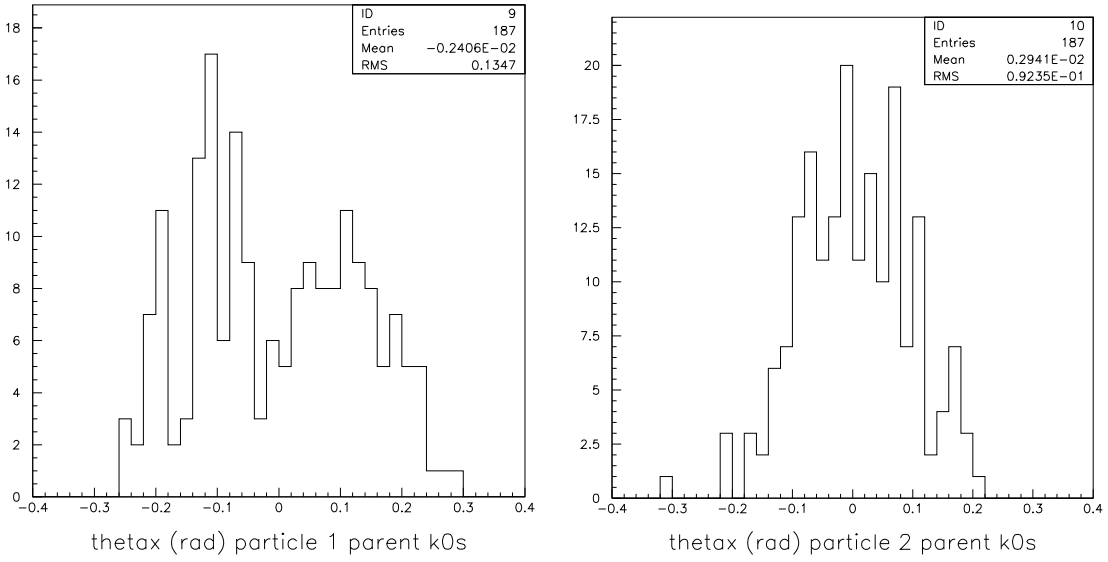

Figure 10.13: θ_x angle for the first (left) and the second (right) particle in pairs with the same parent K^0_S, cut 1 to 10 applied (Monte Carlo 'QGSP' generator)

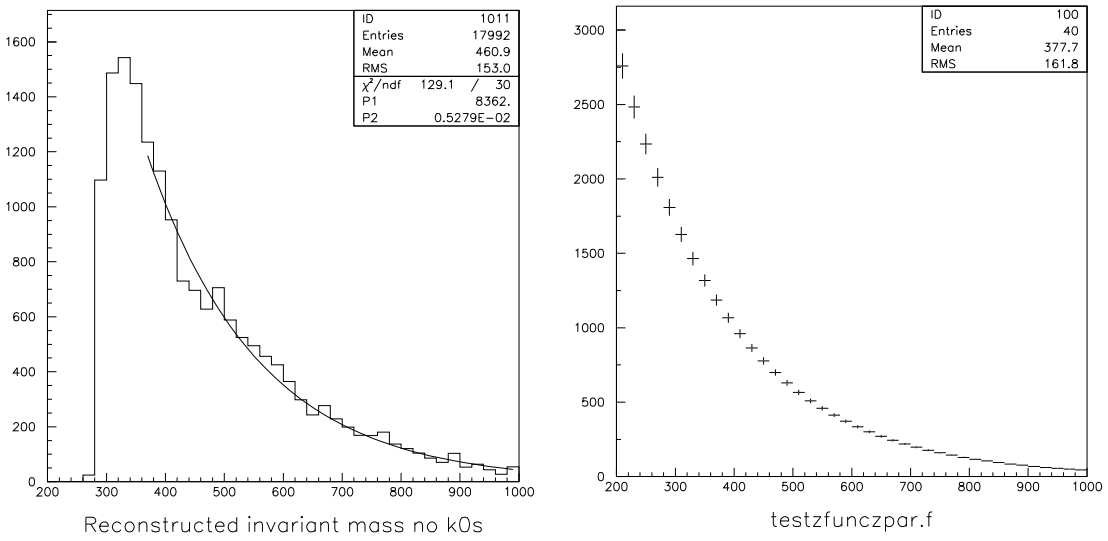

Figure 10.14: Fit of the invariant mass (MeV/c^2) for pairs with cuts 1 to 10 applied (Monte Carlo 'QGSP' generator)

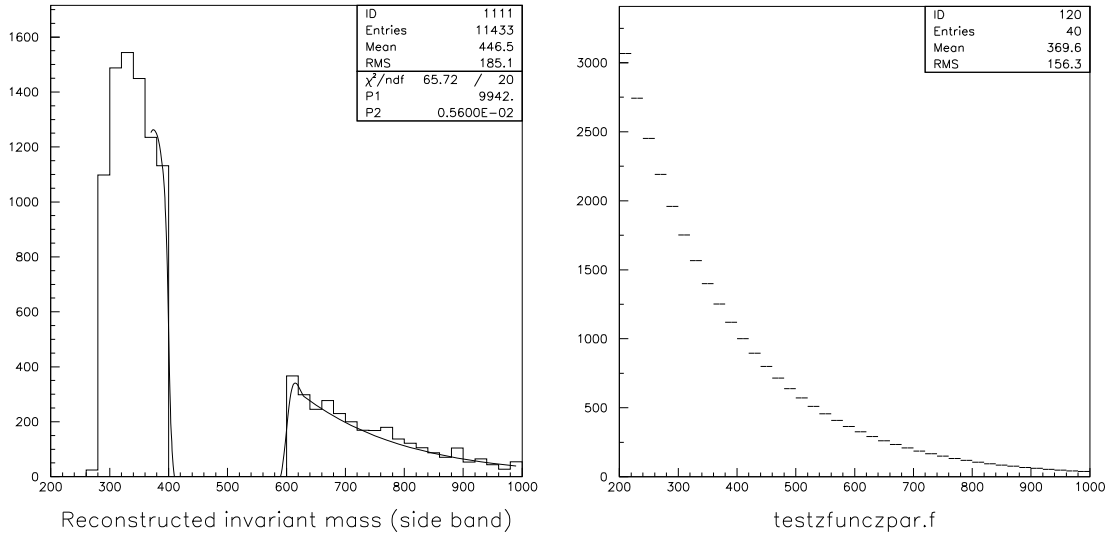

Figure 10.15: Fit of the invariant mass (MeV/c^2) for pairs with the region 400-600 Mev/c^2 excluded, with cuts 1 to 10 applied (Monte Carlo 'QGSP' generator)

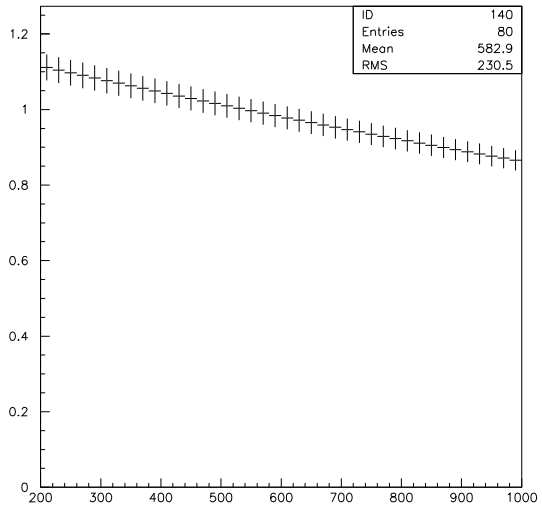

Figure 10.16: Ratio between the fit of the invariant mass with the region 400-600 Mev/c^2 excluded and the fit of the invariant mass with pairs from the same K^0_S parent excluded, with cuts 1 to 10 applied (Monte Carlo 'QGSP' generator)

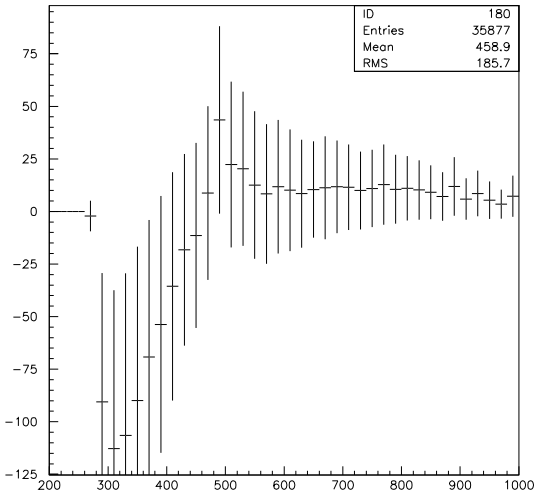

Figure 10.17: Invariant mass (MeV/c^2) for pairs after background subtraction, with cuts 1 to 10 applied (Monte Carlo 'QGSP' generator)

Chapter 11

K^0_S invariant mass reconstruction from physics data

11.1 Using 12 GeV/c Be thin target data

11.1.1 Over a sample of 10000 events

As an exercise we have tried to reconstruct the invariant mass for physics data by reconstructing 10000 events on Be 5% of an interaction length target and for 12 GeV/c beam.
A total of 8440 events have been reconstructed, leading to a smaller efficiency compared to the Monte Carlo data produced using the 'QGSP' generator.
The number of pairs obtained is given in Figure 11.1. The reconstruction efficiencies are given in Table

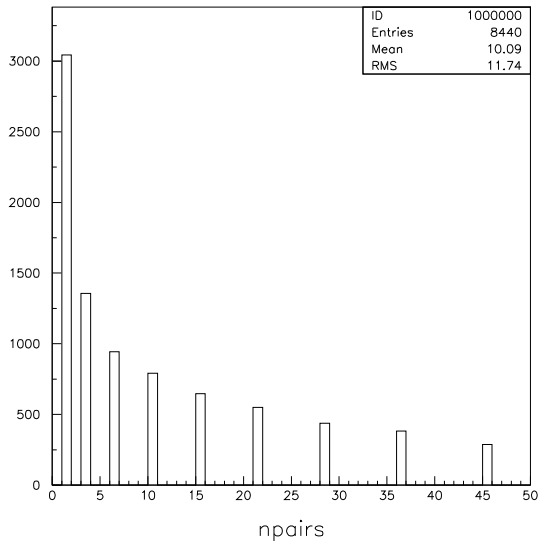

Figure 11.1: Number of pairs reconstructed (Be 5%, 12 GeV/c beam)

11.1. The fraction of pairs remaining after cuts is of the same order as for the K^0_S study with the 'QGSP' generator ($\sim$ 1%).
Figure 11.2 gives the reconstructed invariant mass for pairs with cuts one to four applied.

Cut	Selection criteria	Number of pairs (total 80925)
1	reconstructed in the NDCs	27054
2	& extrapolated at $z = 0$	3220
3	& momentum measured	1240
4	& pairs of opposite charge particles	606

Table 11.1: Number of pairs and cuts for reconstructed particles (Be 5% target, 12 GeV/c beam)

Figure 11.3 gives the reconstructed invariant mass after subtraction of the combinatorial pion background

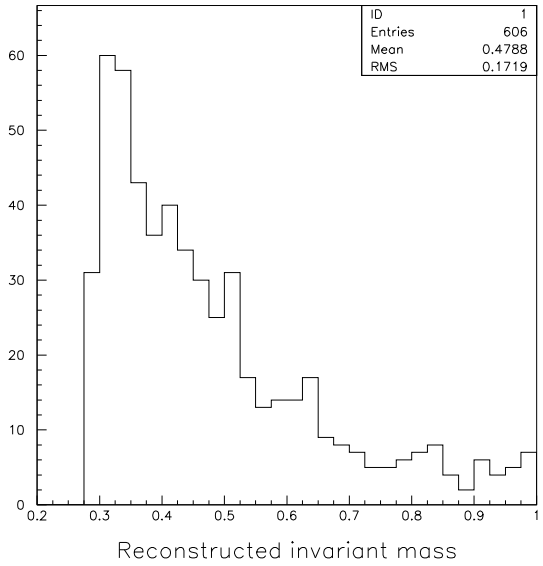

Figure 11.2: Reconstructed invariant mass (GeV/c^2) for pairs, cuts 1 to 4 applied (Be 5%, 12 GeV/c beam)

obtained with the Monte Carlo simulation (see Figure 10.6). There is the hope to select K^0_S looking at the excess of events in the region around 0.5 GeV/c^2 with about hundred time more statistics. A particle identification should also help to cut on background not coming from opposite charge pion pairs and help to resolve the K^0_S peak.

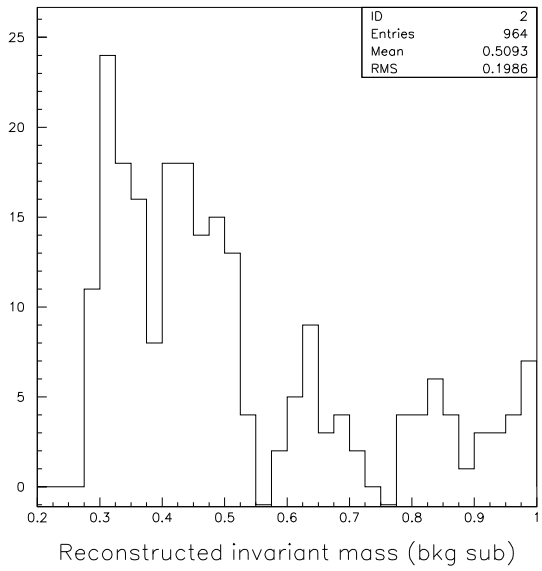

Figure 11.3: Reconstructed invariant mass (GeV/c^2) for pairs, cut 1 to 4 applied, after background subtraction (Be 5%, 12 GeV/c beam)

Total number of events processed	1089265
Number of events retrieved	607657
Number of events reconstructed	565898

Table 11.2: Processing and reconstruction efficiencies (Be 5% target, 12 GeV/c beam)

Cut	Selection criteria	Number of pairs (total 3812942)
1	reconstructed in the NDCs	2377893
2	& modules downstream fired	1475484
3	& extrapolated at $z = 0$	1170746
4	& momentum measured	90157
5	& χ^2/ndf of the track fit < 20	73621
6	& $\sigma_p/p < 40\%$	70352
7	& $0.2 <$ p < 12.0 GeV/c	60192
8	& pairs of opposite charge particles	29390
9	& probability to be a pair of pions above 60%	6593
10	& $\|\|\overrightarrow{r_1} - \overrightarrow{r_2}\|\| < 20$ cm at $z = 0$	5660

Table 11.3: Number of pairs remaining after cuts on the reconstructed particles (Be 5% target, 12 GeV/c beam)

11.1.2 With the statistics of one million events

A sample of one million events from the Be 5% of an interaction length target at 12.0 GeV/c beam momentum has been processed corresponding to $\sim$ 50% of the Be 5% 12 GeVc setting. The efficiencies for the events processing and reconstruction are given in Table 11.2. The reconstruction efficiency for the events is quite good ($\sim$ 93%).
The efficiency for the pair reconstruction is given in Table 11.3.
The cut on the χ^2/ndf of the track fit is compatible with the distribution in Figure 11.4 for pairs with cuts one to four in Table 11.3 applied.
The cut on the σ_p/p is compatible with the distribution in Figure 11.5 for pairs with cuts 1 to 5 applied.
The cut on the distance between the two particles extrapolated at $z = 0$ is compatible with the Figure 11.6 for pairs with cut one to nine applied.
The cut on the pion probability permits to select particles which have been identified as pions and reject the unwanted background (see Figure 11.7).
Figure 11.8 show the invariant mass for pairs with cuts one to ten applied. Plots in Figure 11.9 show the result of the fit on the invariant mass for pairs with cuts one to ten applied and where the region 400-600 MeV/c^2 has been excluded. This fit can be used to subract the combinatorial pion background from the invariant mass plot. We do the exercise on the data sample and we obtain the Figure 11.10. Again we are not able to resolve the K^0_S invariant mass peak. However the number of K^0_S we can set for this data sample can be calculated as for the Monte Carlo case. Table 11.4 gives the different values we get for the data sample. Using the efficiency computed from the Monte Carlo sample $\varepsilon = 12.1\%$, we get:

$$N_{K^0_S} = (-5.82 \pm 0.54) \cdot 10^{-4}$$

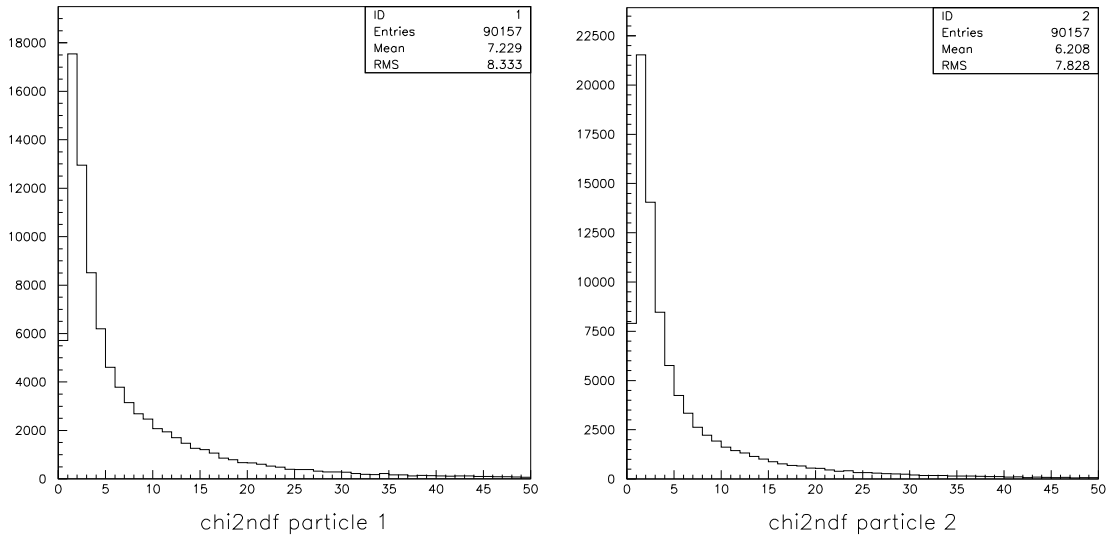

Figure 11.4: χ^2/ndf of the track fit for the first (left) and the second (right) particle in pairs, cut 1 to 4 applied (Be 5% target, 12 GeV/c beam)

f_{bkg}	902 ± 33
N_p^{inc}	607657
N	859 ± 29

Table 11.4: Numbers relevant for the calcul of the limit on the K_S^0 events

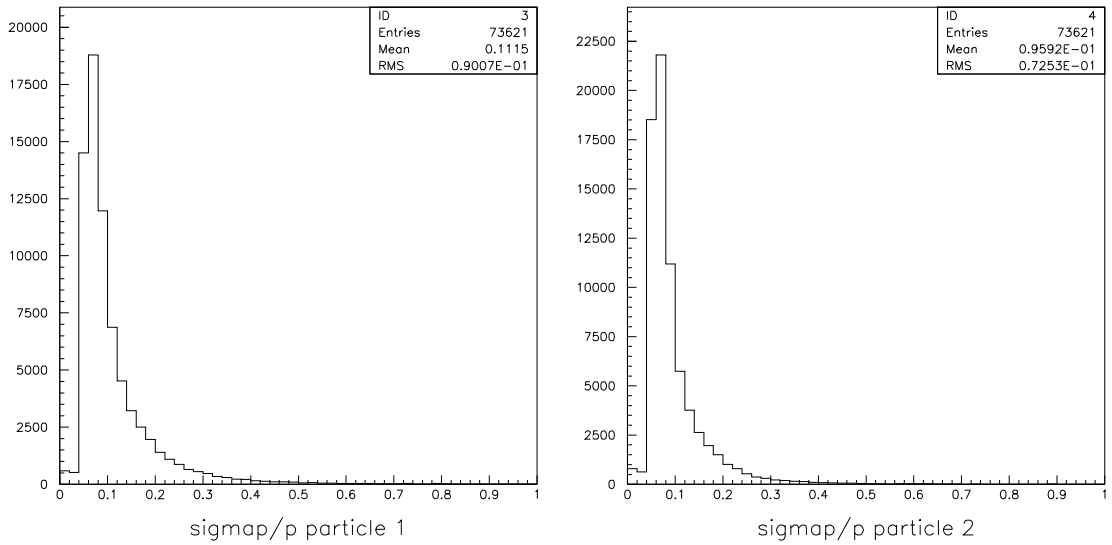

Figure 11.5: σ_p/p for the first (left) and the second (right) particle in pairs, cut 1 to 5 applied (Be 5% target, 12 GeV/c beam)

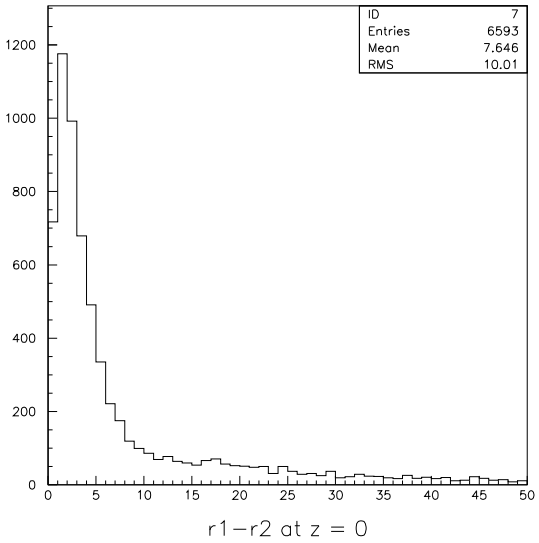

Figure 11.6: Distance (cm) between the two particles extrapolated at $z = 0$ for pairs with cut 1 to 9 applied (Be 5% target, 12 GeV/c beam)

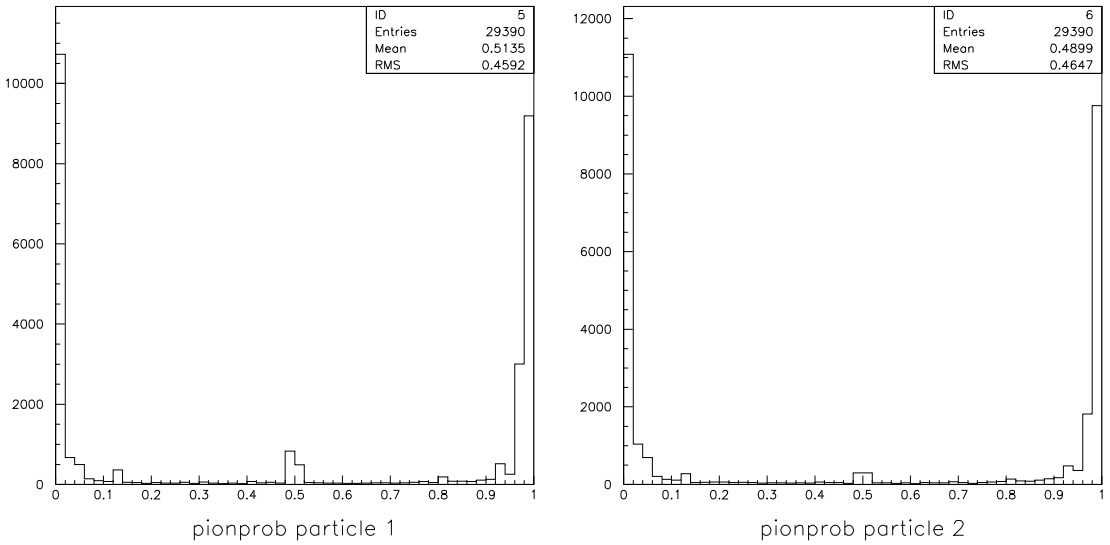

Figure 11.7: Pion probability for first (left) and second (right) particle for pairs with cut 1 to 10 applied (Be 5% target, 12 GeV/c beam)

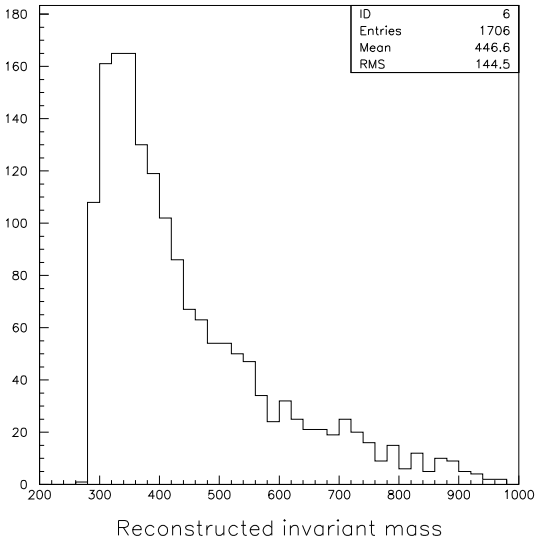

Figure 11.8: Invariant mass (MeV/c^2) for pairs, cuts 1 to 10 applied (Be 5% target, 12 GeV/c beam)

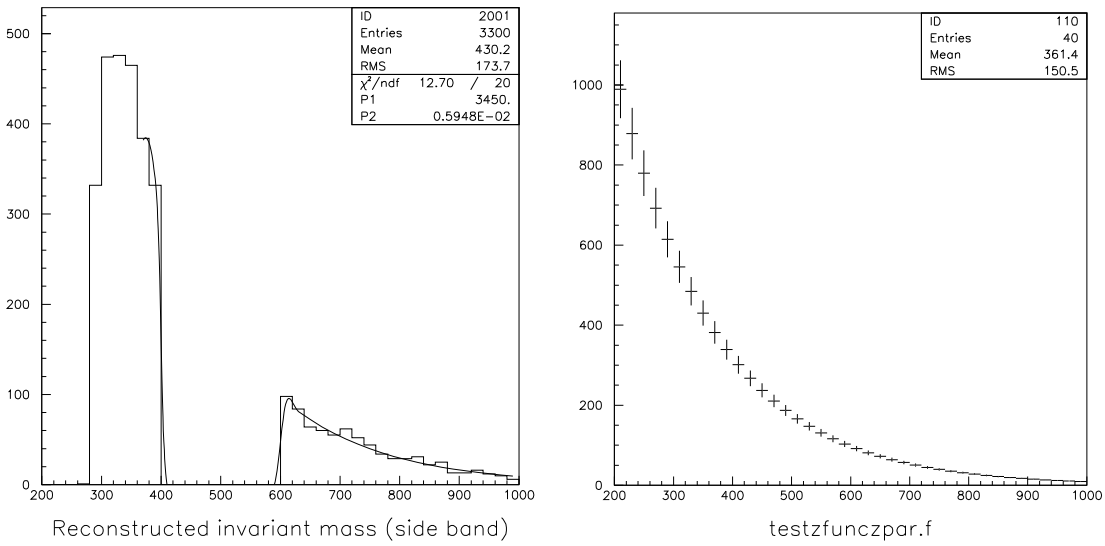

Figure 11.9: Fit of the invariant mass (MeV/c^2) for pairs, cuts 1 to 10 applied with region 400-600 MeV/c^2 excluded (Be 5% target, 12 GeV/c beam)

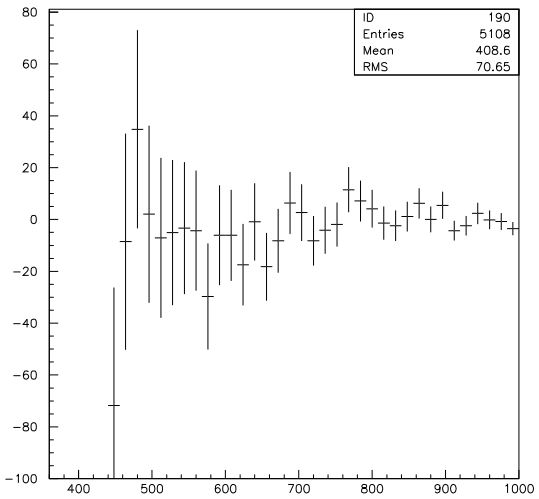

Figure 11.10: Invariant mass (MeV/c^2) after background subtraction for pairs with cuts 1 to 10 applied (Be 5% target, 12 GeV/c beam)

Chapter 12

Conclusion

The Be 5% and 100% λ_{int} at 12 GeV/c beam data set provided by the HARP experiment have served to study the reconstruction efficiency of a vertex fit based on a Kalman fitter procedure for the NDCs and the TPC detectors. Whereas some improvements are needed in the reconstruction to fit correctly the TPC tracks with the Kalman track fit, we were able to estimate the efficiency of the vertex for the NDCs tracks from Monte Carlo simulation. It is expected that some improvement in the calibration, and alignment as well as the magnetic field mapping would help to obtain better results for the vertex fit. Nevertheless once the tracking will be validated for both detectors, a detailed and systematic study of the input parameters to the fitter, as well as the reference surface acceptance would be required. This would help to build a robust vertex fitter that can fit primary and secondary vertices and allow for track rejection through the χ^2 computation.
As a validation of the HARP reconstruction, and with the hope to provide numbers on the K^0_S production for conventional neutrino beams, a search for K^0_S in 50% of the Be 5% 12 GeV/c beam setting has been performed. A Monte Carlo generator has permitted first to validate the invariant mass reconstruction efficiency for charged pions coming from K^0_S with defined kinematics. A hadronic Monte Carlo generator was used to estimate the combinatorial pion background and the K^0_S reconstruction efficiency. This permitted to set number of K^0_S events in the Be 5% data sample to $N_{K^0_S} = (-5.82 \pm 0.54) \cdot 10^{-4}$ and in the Monte Carlo sample to $N_{K^0_S} = (-3.69 \pm 1.00) \cdot 10^{-3}$. These two number are compatible between them and compatible with zero K^0_S events. We have demonstrated with the Monte Carlo sample that we are not able to find K^0_S events at present. However, a precise understanding of the Monte Carlo generator and corrections for unexpected features in it would help to compute with accuracy the combinatorial pion background. On the reconstruction side, calibration of the particle identification detectors and precise alignment of the NDCs would permit to gain in resolution and observe in the future a K^0_S signal. The efficiencies of the simulation and reconstruction for the different detectors are required in order to get a proper normalization between the data and the Monte Carlo. Efforts are pursued at present in order to enter the detector response in the simulation part and good progress have been done for numerous HARP detectors. Improvements that we will obtain in the next future will help to find signal from neutral particles decay such as K^0_S.

Remerciements

Je voudrai tout d'abord remercier Lucie Linssen et Alain Blondel, mes superviseurs, sans qui cette aventure de quatre années n'aurait jamais pu commencer ni se terminer.
J'aimerai remercier Allan Clark pour avoir gentiment accepté de faire partie du jury, de lire et de juger ce travail.
Je tiens à remercier aussi les autres participants du jury, Jaap Panman et Jacques Dumarchez pour leurs conseils à la lecture et à la correction de mon manuscrit.
Des personnes embarquées sur le bateau HARP, nombreuses sont celles à qui je suis reconnaissante de m'avoir fait partager leur passion pour la physique, leur enthousiasme et leur connaissance. Merci entre autre, à Petr Gorbounov, Jean-Claude Legrand et Piero Zucchelli qui ont guidé mes premiers pas dans l'expérience sur les chambres multi-fils à compteur proportionnel (MWPC) et la chambre à projection temporelle (TPC), ainsi qu'a Emilio Radicioni notre maître DAQ.
Merci à Claude Detraz, José Mulon et Mario Scandurra pour leur disponibilité et les bons moments passés ensemble, ainsi qu'à tout les membres de l'équipe de support technique TA1 du CERN qui nous a suivie dans ce voyage.
Merci a Claude Millerin et Nicole Wauquier de l'atelier de montage électronique et soudure du CERN ainsi qu'à leurs collègues qui ont soufferts pendant la période de montage du détecteur.
Merci à Luciano Musa et Roberto Campagnolo de la TPC d'ALICE pour leur support, nombreux coups de mains et conseils sur les cartes de lectures de la TPC dont nous avons partagé l'électronique.
Merci à Markus Joos et James Rouet de l'équipe de support des systèmes électronique du CERN pour leur aide précieuse dans le développement des logiciels de lecture de l'électronique la TPC.
Merci à Anselmo Cervera, mon maître à penser du vertex, pour sa patience et sa disponibilité lorsqu'il à fallu descendre dans l'arène pour empoigner le taureau Kalman.
Merci à mes collègues de HARP, doctorants ou jeunes docteurs, Jean-Sébastien Graulich, Alexander Grossheim, Aysel Kayis-Topaksu, Cristina Morone, Silvia Borghi, Lara Howlett et Stefan Piperov pour les agréables moments passés ensemble et leur soutien durant les phases les plus noires de cette thèse.
Au tour des moins jeunes maintenant, merci à Valeri Serdiouk notre expert TPCino, Isabelle Lenique du secrétariat HARP, Dimitar Kolev et Ilya Tsukerman les experts en remontant.
Merci à mes amis et collègues de l'université de Genève Simone Gilardoni, Shulamit Moed, Mario Campanelli, Evelyne Delmeire et Raphäel Schröeter, ainsi qu'a Catherine Blanchard au secrétariat du DPNC pour sa disponibilité et son aide constante.
Cette thèse a été financée en partie grâce au soutien du programme des étudiants doctorants du CERN et en partie par l'université de Genève. Merci donc à ces deux institutions qui m'ont donné la chance de pouvoir conduire et mener à terme ce travail.
A mes amis[1], en particulier Nadia Zuodar, Sébastien Kessler, Gisèle Balet et Jérôme Knöbl, mes parents Jacqueline et Christian et ma précieuse famille, pas de mots assez fort pour vous exprimer mon immense gratitude pour votre présence, votre soutien et votre confiance en moi. Merci aussi pour m'avoir ramenée bien souvent à la réalité du monde en dehors de la physique. Cette thèse est en partie la vôtre.
Enfin, pardon à celles et ceux que j'oublie ici, ne m'en veuillez pas trop c'est bien connu que les physiciens ont la tête en l'air.

[1] ma bande de ph3iens, de geeks et les filles je ne vous oublie pas mais il commence à y avoir beaucoup de monde sur cette page...alors le coeur y est même si vous ne voyez pas votre nom.

Appendix A

Software release $v7r4$

For the study done using the $v7r4$ software release, some packages have been modified and used locally. The modifications are described in more details below. We are linking dynamically to $v7r4$ version of the packages which are not local.

A.1 Local packages

A.1.1 *Simulation*

For *Simulation* the reference tag $Tv7r4 - T20041012$ has been used locally.
Different versions of $HsExclusiveGenerator$ have been written:

- creation of two 1 GeV/c momentum pions with $\varphi_{\pi^-} = \varphi_{\pi^+} = 0$ and $\theta_{\pi^+} =$ - $\theta_{\pi^-} = \pi/4$ rad for the TPC reconstruction and vertex performance study.
- creation of two 1 GeV/c momentum pions with $\varphi_{\pi^-} = \varphi_{\pi^+} = 0$ and $\theta_{\pi^+} = \theta_{\pi^-} = 150$ mrad for the NDC reconstruction and vertex performance study.
- creation of two charged pions with $\varphi^* = 0$ and $\theta^* = \pm\pi/2$ rad for K^0_S study.

The beam particle starts at (0,0,-450) cm in order to be reconstructed by the MWPCs.
The code is available on the PC computer PCCH90 in /localscratch1/gprior/mycmt/Simulation/v7r4/.

A.1.2 *Reconstruction*

The reference tag $Tv7r4$ of the *Reconstruction* package is used locally. It contains a modified version of $VertexFindingAlg$ in order to place the reference surfaces for the vertex computation at the position $z = 0$. It contains a modified version of $SetupKalmanAlg$ which loads stray field and solenoidal field only if the corresponding volumes are defined. It contains a modified version of $ComputeNdcMomentumAlg$ with a fix for NDCs tracks of $typeIII$ which were having a wrong momentum computation before. It contains a modified version of $BeamPartIDAlg$ to take into account the cuts on the ADC variables of the TOF A and TOF B detectors for 12.0 GeV/c beam momentum. The code can be found on the PC computer PCCH90 under /localscratch1/gprior/mycmt/Reconstruction/v7r4/src/Reconstruction in HarpParticle/ for $VertexFindingAlg$, in Kalman/ for $SetupKalmanAlg$, in Ndc/ for $ComputeNdcMomentumAlg$ and in BeamPid/ for $BeamPardIDAlg$.

A.1.3 *tests*

The reference tag $Nv7r4-T20041012$ of the tests package is used locally. In SystemTests/Vertex/ directory we have modified locally the algorithm $VertexReadingAlg$ in order to place the reference surface at the position $z = 0$. The jobOptions used for the vertex study can also be found at the same place.
The reference surface for the extrapolation to z=0 is a circle centered in (0,0,0) with axis of rotation z and 100 cm radius.
In SystemTests/ a MakeiDST/ directory has been created locally. It contains jobOptions to create iDSTs from Monte Carlo simulation and the iDSTs that we used for vertex and invariant mass study.
A InvariantMass/ directory has been created in SystemTests/. It contains the algorithm which computes the invariant mass ($InvariantMassAlg$) and the corresponding jobOptions files.
The local package tests/ can be found on the PC computer PCCH90 under /localscratch1/gprior/mycmt/tests/.

A.1.4 *Analysis*

The reference tag $Tv7r4a1$ of the Analysis package is used locally. In MiniDstReader/ the name of the file $GaudiMain.cpp$ has been changed to $GaudiMain\_MdstReader.cpp$ in order not to overwrite the version of $Gaudimain.cpp$ used to write mini data summary tapes (mDSTs). In miniDST/ the algorithm $MiniDstWriterAlg$ has been modified to save the PDG code of the parent particle as well as the pointer to the parent. The directory InvariantMassFromMdst/ contains the code which calculates the invariant mass from data stored under mDST format.

A.2 Data storage format

A.2.1 iDST

The iDST format has been chosen for the Monte Carlo data produced for the vertex study as well as for the K_S^0 study with the 'exclusive' generator.

A.2.2 mDST

The mDST format has been chosen for the processing over large a sample of events for both Monte Carlo data with the generator 'QGSP' and HARP data. The TPC information is not saved in mDST so it cannot be compared to the reconstruction we had either from iDSTs or while looking at raw data. Concerning the Monte Carlo information of the beam particle it seems that the matching between the reconstructed particle and the Monte Carlo particle is not done properly.

Appendix B

Comparison between Monte Carlo and reconstructed momentum

B.1 Momentum reconstruction in NDC detector

The difference between the true Monte Carlo momentum and the reconstructed particle momentum extrapolated at a reference surface situated in $z = 0$ for the π^- and the π^+ is shown in Figures B.1, B.2 and B.3 for NDCs tracks. The reference surface is a disc of 100 cm radius with rotation axis being z. It has been chosen so to be as close as possible to the true vertex point and therefore the true momentum that we would expect. These plots are coming from the Monte Carlo data produced for the vertex study with production of two secondaries at $\varphi = 0$ and $\theta = 150$ mrad and with the solenoid field switched off. This way we can estimate the influence of the dipole field map since it is the only field that the particle will cross. Tracks for which the momentum is not measured have been excluded from the plots. A cut on the χ^2/ndf of the track fit below 20 and on the $\chi^2_k(filter)$ of the vertex fit below 100 as well as three reconstructed particles are required to select the tracks that have been chosen for the vertex pull computation. There is a difference in the shape for the π^- and the π^+ showing that the treatement of the particle by the reconstruction depends on its sign. For the difference in momentum in x, we get a ~ 7 MeV/c shift for the π^- and ~ 10 Mev/c shift for the π^+. The resolution is of 20-30 MeV/c order which is worse than expected but possibly dominated by the tail. The momentum difference in y is shifted by ~ 26 MeV/c for both pions with a noticable difference between the two particles. The resolution is ~ 10 MeV/c which is still large. Given the wire position (in the vertical plane) we normally expect a better resolution in x than in y which is not the case. In fact the momentum resolution in x is not good enough to keep the reconstruction efficiency for the momentum in x better than in y as we would expect from the wire position.
We have to recall that in the simulation the π^+ is produced in the ($+x$,z) plane and will bend to the left if we look downstream whereas the π^- is produced in the (-$-x$,z) plane and will bend to the right. It seems here that there is an asymmetry problem in the mapping of the dipole field as a function of the x coordinate or an inequal treatement between particles of different charge in the reconstruction of the NDCs.
The momentum difference in z is shifted by ~ 40 MeV/c and ~ 60 MeV/c for the π^- and π^+ respectively and the σ is ~ 100 MeV/c which is quite large even if we don't expect a good resolution in z for NDCs detectors. The difference between the total Monte Carlo momentum and the total momentum at the reference surface is shown in Figure B.4 for the absolute value of the difference below 1 GeV/c. It gives the overall resolution we can expect for momentum reconstruction for both the positive and the negative pions. It seems that the problem comes from the momentum estimate in z. We can only expect some improvement

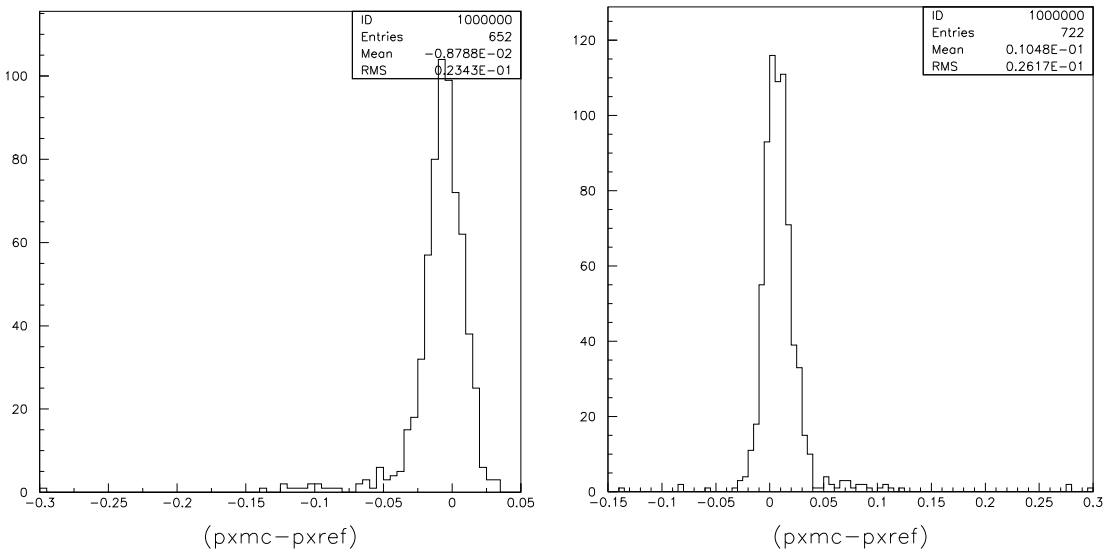

Figure B.1: Difference (in GeV/c) between the Monte Carlo and the reconstructed momentum at $z = 0$ in p_x for the π^- (left) and the π^+ (right) for the NDC detector, simulation for the vertex study

here with an accurate control of the HARP field map as well as a precise alignment of the NDCs wires.

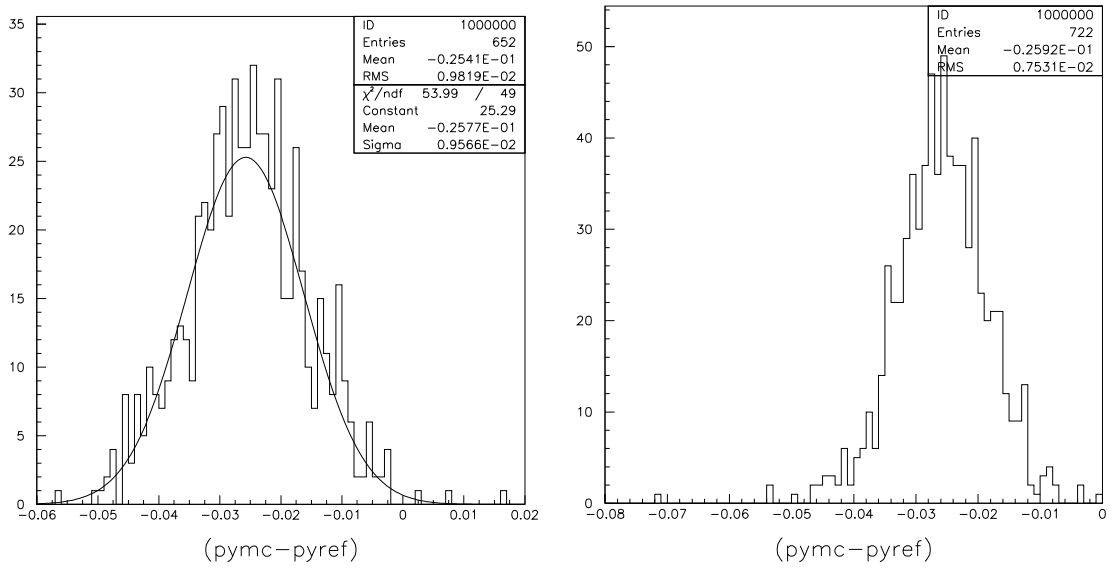

Figure B.2: Difference (in GeV/c) between the Monte Carlo and the reconstructed momentum at $z = 0$ in p_y for the π^- (left) and the π^+ (right) for the NDC detector, simulation for the vertex study

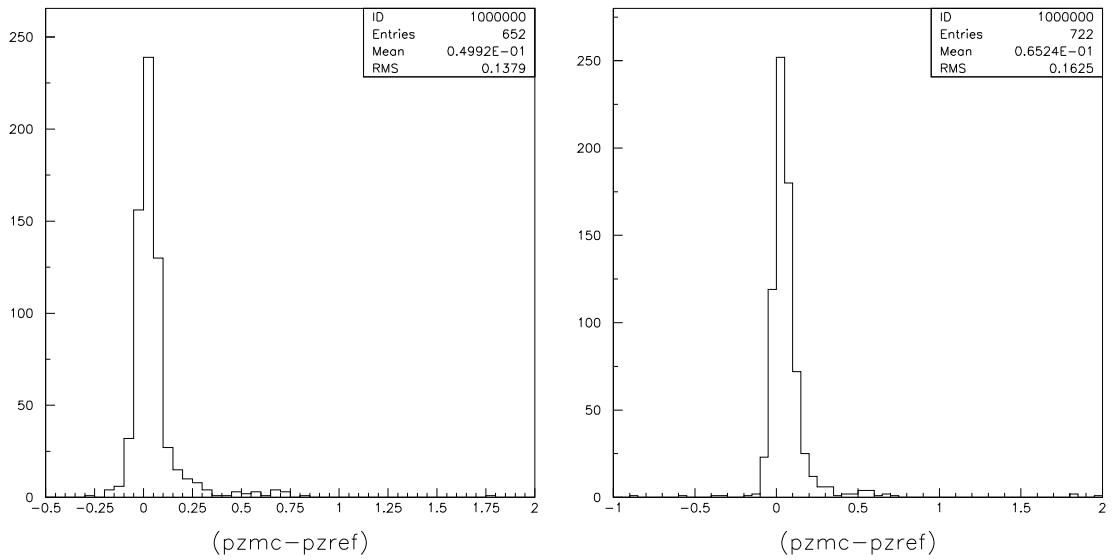

Figure B.3: Difference (in GeV/c) between the Monte Carlo and the reconstructed momentum at $z = 0$ in p_z for the π^- (left) and the π^+ (right) for the NDC detector, simulation for the vertex study

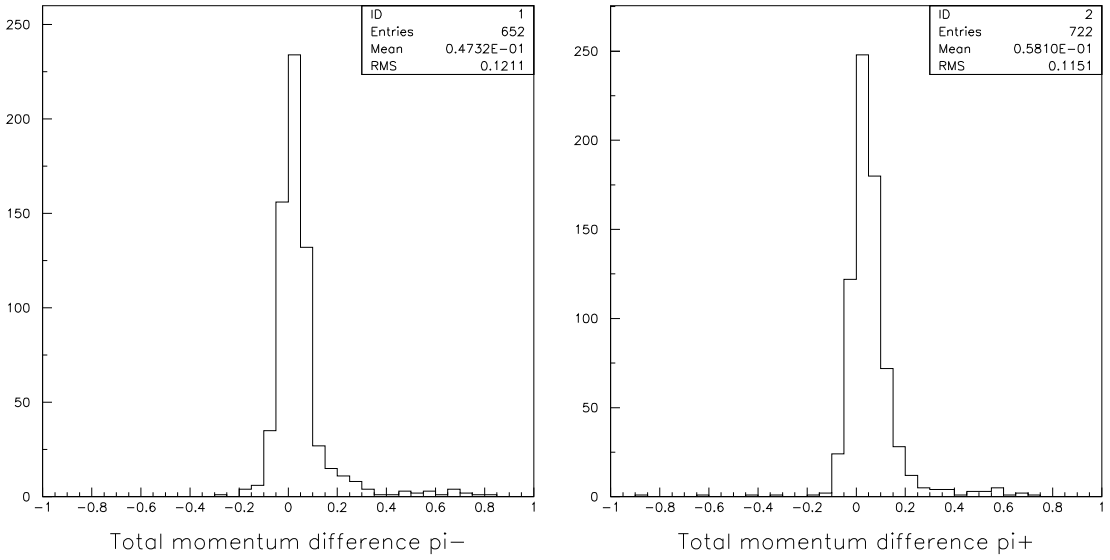

Figure B.4: Difference (in GeV/c) between the Monte Carlo and the reconstructed momentum at $z = 0$ for the π^- (left) and the π^+ (right) for the NDC detector, simulation for the vertex study

B.2 Momentum reconstruction in the TPC detector

The fit of the difference between the Monte Carlo momentum and the reconstructed particle momentum extrapolated at the reference surface for TPC tracks is shown in Figures B.5, B.6 and B.7 for a value of the difference in p_x, p_y or p_z not exceeding 20 GeV/c. These plots are coming from the Monte Carlo data produced for vertex study with two secondaries at $\varphi = 0$ and $\theta = 785$ mrad. The same cuts have been used as for the TPC vertex study case in order to select the events that entered the pull computation.

The difference in momentum in p_x, p_y and p_z are at unacceptable large values showing that the fit of

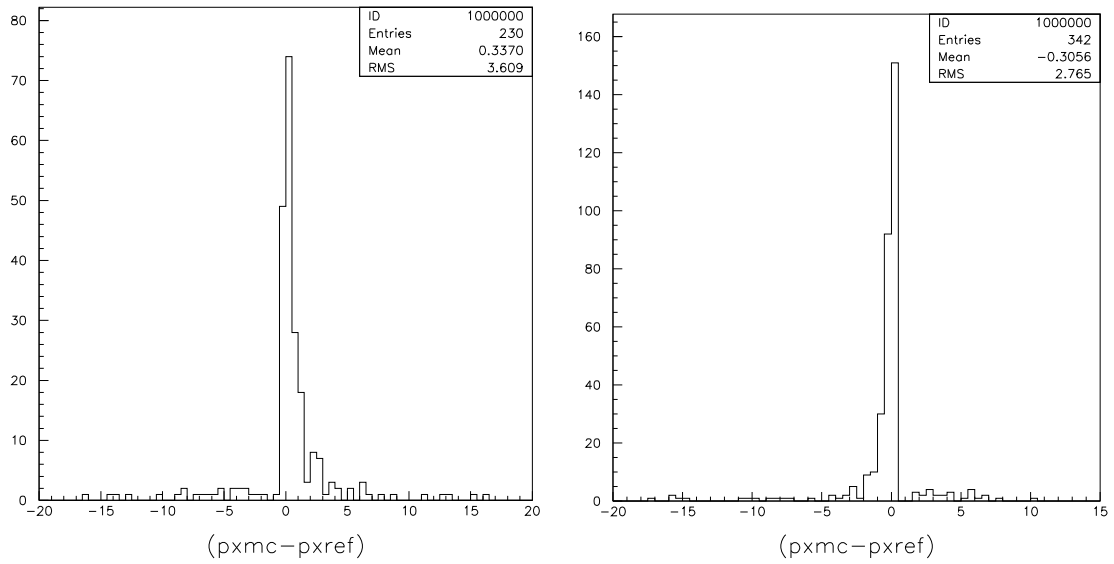

Figure B.5: Difference (in GeV/c) between the Monte Carlo and the reconstructed momentum at $z = 0$, in p_x for the π^- (left) and the π^+ (right) for the TPC detector, simulation for the vertex study

the TPC tracks with the Kalman fitter is not performing well. The difference between the Monte Carlo momentum and the reconstructed momentum from the helix fit is shown in Figures B.8, B.9 and B.10 for the π^- and the π^+. The difference for the momentum from the helix fit has more reasonnable values but still the resolution is not really satisfactory. Morever the difference of shape between the π^- and the π^+ is not explained. The momentum difference between the Monte Carlo momentum and the momentum extrapolated at the reference surface is shown in Figure B.11 for absolute value of the momentum difference below 20 GeV/c. We can see here that the distribution is not symmetric and can come from some default value assigned to the momentum for the TPC track fit done by Kalman and not updated in the algorithm later on. The difference between the total Monte Carlo momentum and the total momentum calculated by the helix fit is shown in Figure B.12 for absolute values of the momentum difference below 2 GeV/c. Here the distribution looks better but still not entirely satifactory. A detailed study of the algorithm which creates TPC Kalman tracks has to be performed in order to understand the momentum reconstruction. Concerning the helix fit in the TPC, which does perform better, some improvement are expected in the understanding of the difference between the particle of different charges.

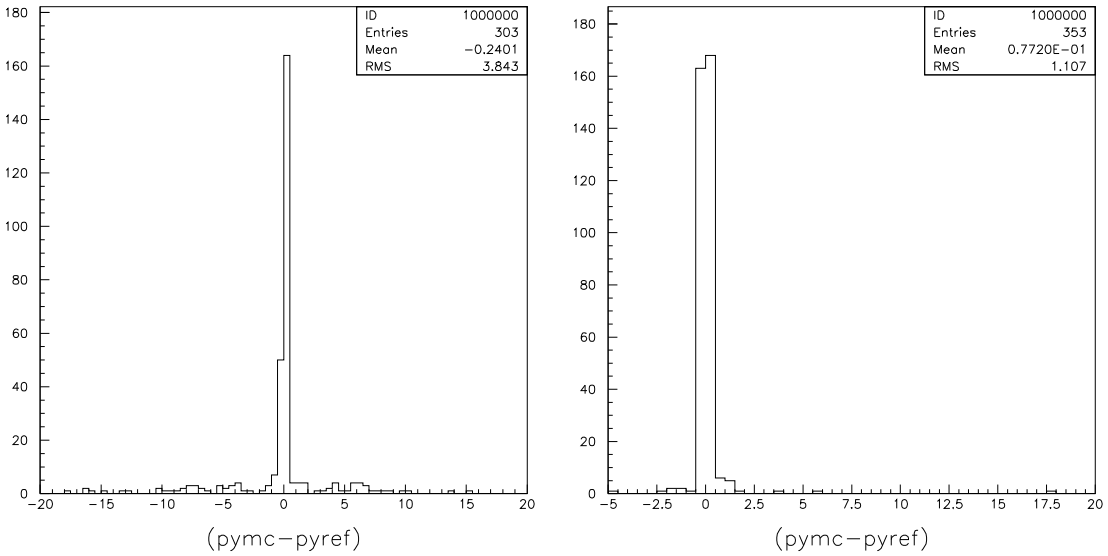

Figure B.6: Difference (in GeV/c) between the Monte Carlo and the reconstructed momentum at $z = 0$ in p_y for the π^- (left) and the π^+ (right) for the TPC detector, simulation for the vertex study

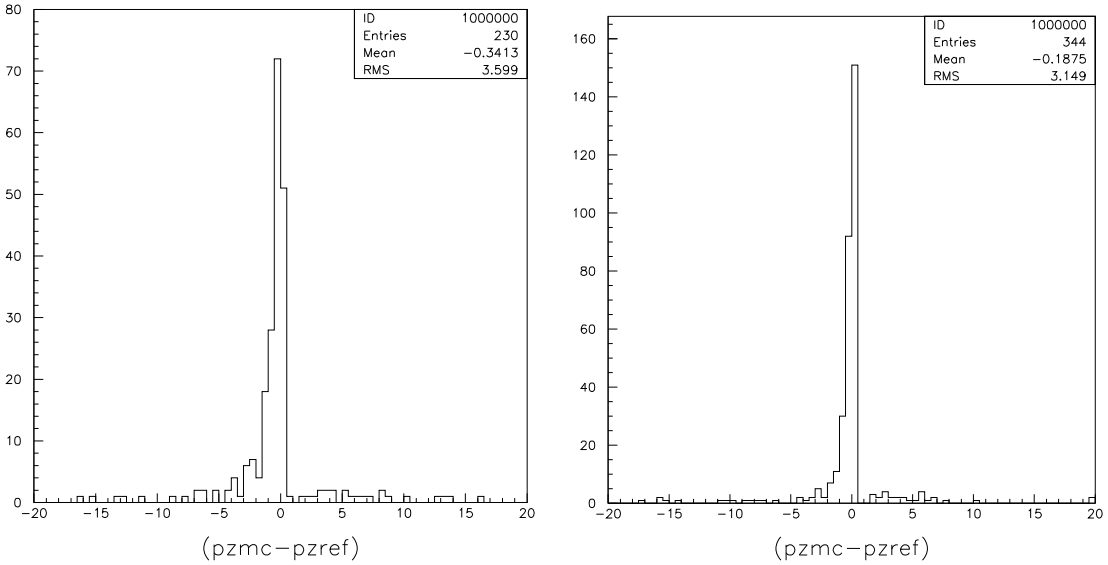

Figure B.7: Difference (in GeV/c) between the Monte Carlo and the reconstructed momentum at $z = 0$ in p_z for the π^- (left) and the π^+ (right) for the TPC detector, simulation for the vertex study

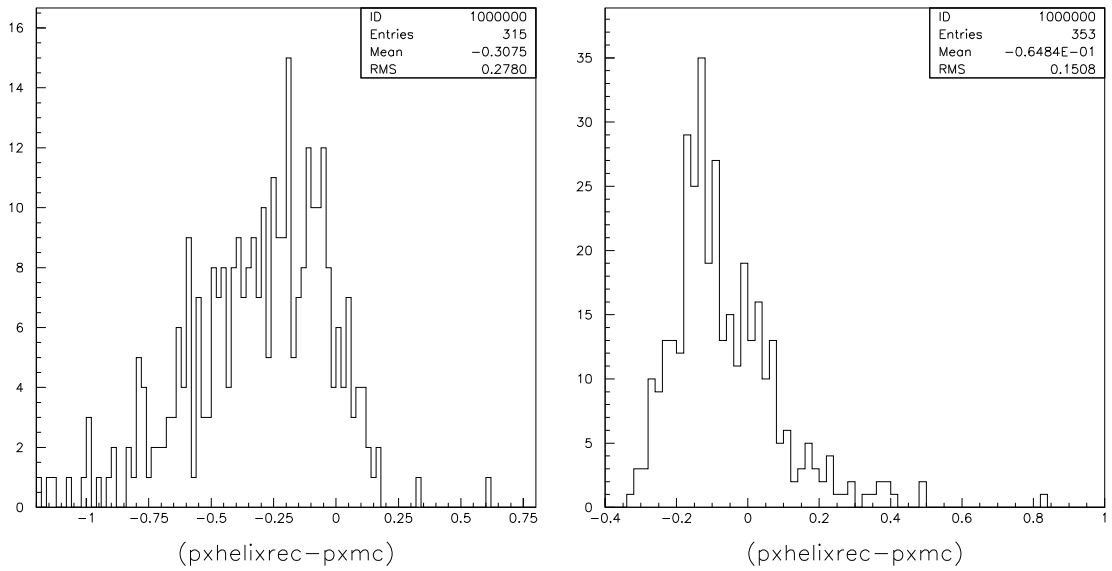

Figure B.8: Difference (in GeV/c) between the Monte Carlo and the reconstructed momentum at $z = 0$ from the helix fit in p_x for the π^- (left) and the π^+ (right) for the TPC detector, simulation for the vertex study

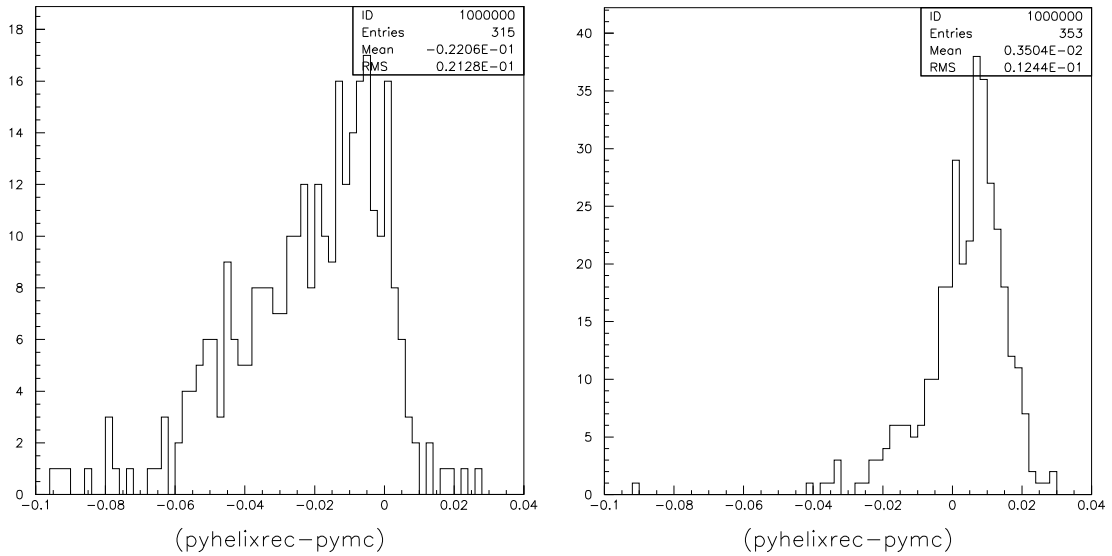

Figure B.9: Difference (in GeV/c) between the Monte Carlo and the reconstructed momentum at $z = 0$ from the helix fit in p_y for the π^- (left) and the π^+ (right) for the TPC detector, simulation for the vertex study

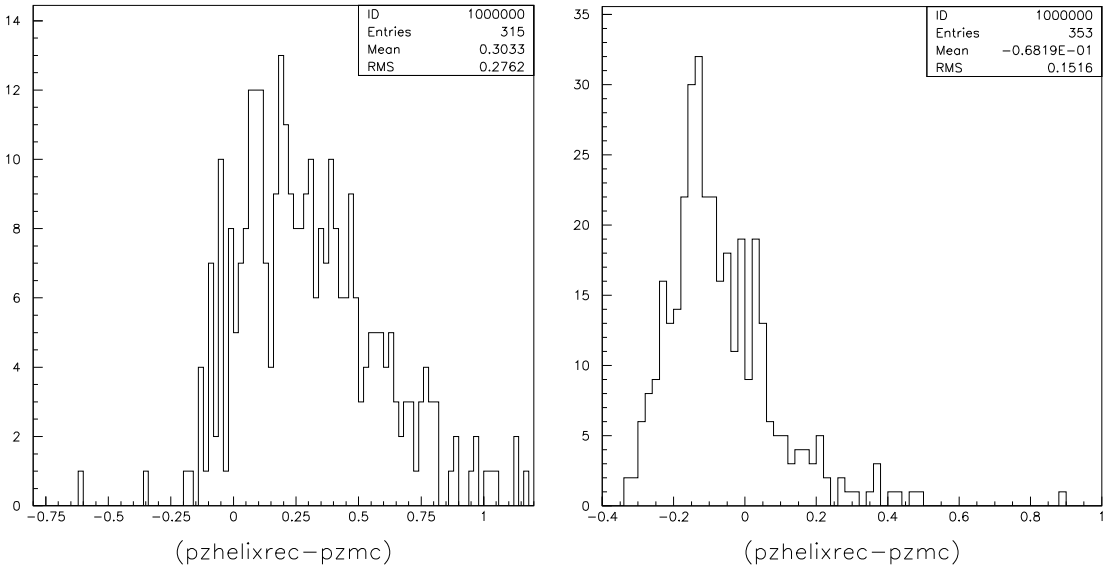

Figure B.10: Difference (in GeV/c) between the Monte Carlo and the reconstructed momentum at $z = 0$ from the helix fit in p_z for the π^- (left) and the π^+ (right) for the TPC detector, simulation for the vertex study

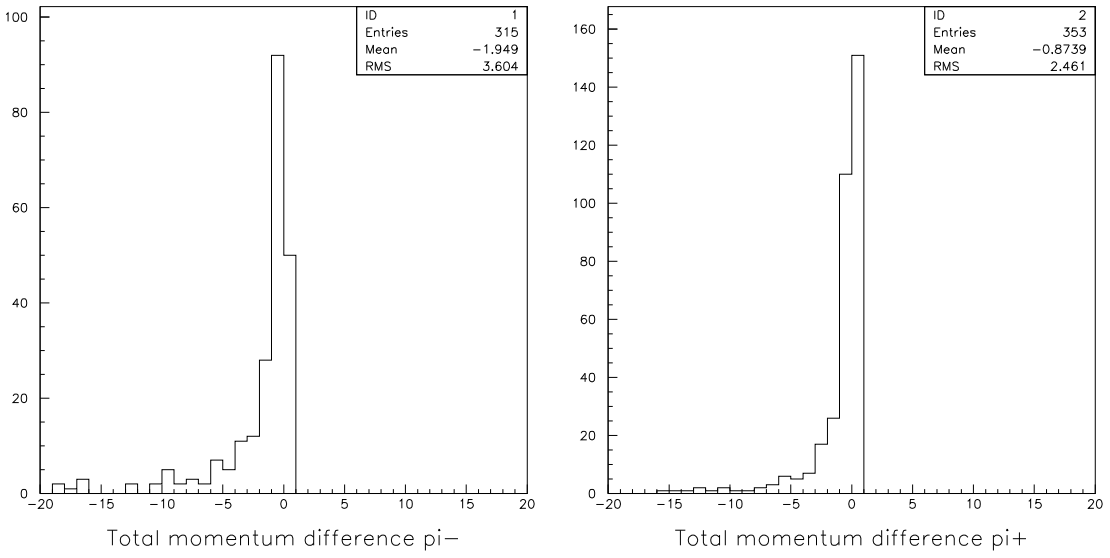

Figure B.11: Difference (in GeV/c) between the Monte Carlo and the reconstructed momentum at $z = 0$ for the π^- (left) and the π^+ (right) for the TPC detector, simulation for the vertex study

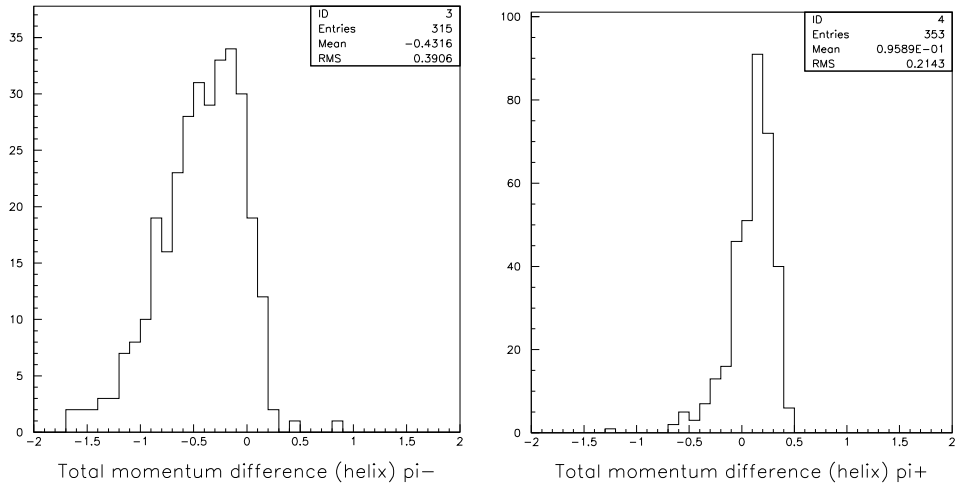

Figure B.12: Difference (in GeV/c) between the Monte Carlo and the reconstructed momentum at $z = 0$ from the helix fit for the π^- (left) and the π^+ (right) for the TPC detector, simulation for the vertex study

Appendix C

Kinematic of two-body decay

Given a particle of four-momentum vector $\mathbf{P} = (E, \overrightarrow{p} \cdot c)$ and mass m which decays in two particles of momentum $\overrightarrow{p}_1$ and $\overrightarrow{p}_2$ and mass m_1 and m_2 respectively. In the rest frame of the particle of mass m the invariant quantity is given by the following relation:

$$|| \overrightarrow{p}_1^* ||=|| \overrightarrow{p}_2^* ||= \frac{\sqrt{(m^2 - (m_1 + m_2)^2) \cdot (m^2 - (m_1 - m_2)^2)} \cdot c}{2 \cdot m} \tag{C.1}$$

with $\overrightarrow{p}_1^*$ and $\overrightarrow{p}_2^*$ being the momentum of the particle 1 and 2 respectively, in the rest frame of the particle of mass m. The energy-momentum conservation tells us that:

$$\mathbf{P^2} = (\mathbf{P_1} + \mathbf{P_2})^\mathbf{2}$$

where $\mathbf{P_1}$ and $\mathbf{P_2}$ are the four-momentum vectors of particle one and two respectively.
The mass m obeys to the invariant mass relation:

$$m^2 = m_1^2 + m_2^2 + 2 \cdot (\frac{E_1 \cdot E_2}{c^4} - \frac{\overrightarrow{p}_1 \cdot \overrightarrow{p}_2}{c^2}) \tag{C.2}$$

For decay products whose parent particle is a K_S^0 the invariant mass is set at 497.648 $\pm$ 0.022 MeV/c.

Appendix D

Tracking efficiency for the NDCs

The tracks detected in the NDC modules have been characterized into three different types, depending on the available information. Tracks with complete information upstream (in module NDC1) and dowstream (in module NDC2) of the dipole magnet are called *type-I*. When only a 2D-segment (one wire per chamber, all four wires being at the same rotation angle) upstream of the magnet is reconstructed and the information is complete downstream they are of *type-II*. Tracks which have no segment upstream of the magnet but with complete information downstream are of *type-III*. The momentum of *type-III* tracks is computed by adding a target constraint. We encounter a significant number of *type-II* and *type-III* tracks due to a beam saturation effect in NDC1, thus degrading the chamber performance. In addition, the high density of hits in this module does not allow for a full efficiency of the pattern recognition algorithm. The tracking efficiency will in turn depend on the track type. It can be computed as follows for a given bin i of the phase space of momentum p and 3D polar angle θ:

$$\epsilon_i^{track} = \frac{N_i^P}{N_i^{acc}} = \epsilon_i^{down} \cdot \epsilon_i^{up-down} \tag{D.1}$$

where N_i^P represent the number of primary particles with momentum measured, N_i^{acc} the number of primary particles accepted (particles which have crossed both modules NDC1 and NDC2), ϵ_i^{down} is the tracking efficiency for NDC modules downstream of the spectrometer and $\epsilon_i^{up-down}$ the upstream-downstream matching efficiency.

Detector inefficiencies and hardware effects have been measured by looking at physics data, whereas geometrical effects have been computed using Monte Carlo data. As a result, plots in Figure D.1 show the total efficiency as well as the efficiency for the different track type as function of momentum, and the angle between the projection of the momentum in the $x - z$ plane and the z axis, θ_x.

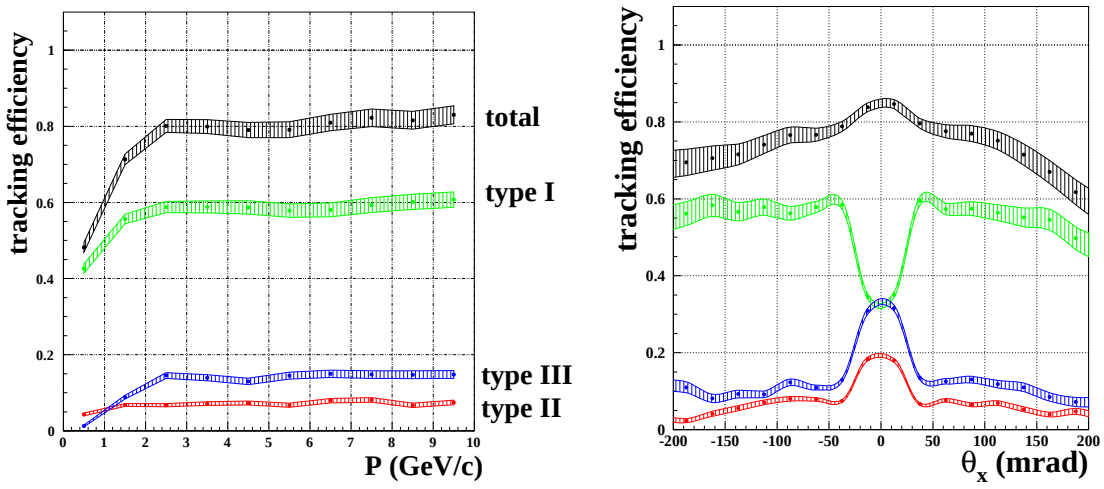

Figure D.1: Tracking efficiency as a function of the track momentum (left) and the θ_x angle

Appendix E

Pion efficiency and purity correction factor

A Bayesian approach has been used to compute the pion identification probability in the downstream spectrometer. Assuming that the measurements coming from the detectors are independent, the probability of identifying a pion as such can be computed from the product of single conditional probabilities coming from the time-of-flight P(p, $\lambda|\pi$) (with $\lambda = m^2/p^2$), the Cherenkov P(p, $N_{phe}|\pi$) (N_{phe} being the number of photo-electrons produced) and the electron identifier P(p, E_1, $E_2|\pi$). The momentum distribution of the particle is used as a prior. An iterative procedure is then used to remove the dependence on the prior and compute the final particle identification probabilities.
The yield of each type of track (t) in NDCs detectors must be corrected by the pion efficiency $\epsilon_j^{\pi-(t)}$ and purity $\eta_j^{\pi-(t)}$ which can be obtained by the following formulae:

$$\epsilon_j^{\pi-(t)} = \frac{N_j^{\pi-true-obs}}{N_j^{\pi-true}} \qquad \eta_j^{\pi-(t)} = \frac{N_j^{\pi-true-obs}}{N_j^{\pi-obs}} \tag{E.1}$$

with $N_j^{\pi-true-obs}$ being equal to the number of observed pions $N_j^{\pi-obs}$ minus the number of background pions. $N_j^{\pi-true}$ is the number of true pions. Pion efficiency and purity have been obtained by selecting clean samples of beam (non-interacting) particles using the beam detectors. They have been measured independently for the different track types. The pion correction factor $\eta_j^{\pi-(t)}/\epsilon_j^{\pi-(t)}$ obtained from 1.5, 3 and 5 GeV/c beam momentum samples is shown in Figure E.1.
For particles of momentum above 5 GeV/c, the pion correction factor has not been estimated yet but the particles we select for the invariant mass are to not expected to have a higher momentum.

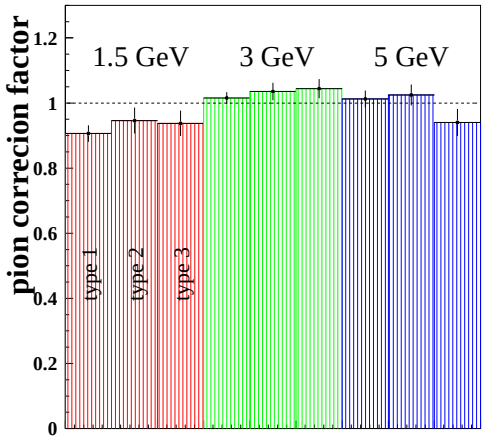

Figure E.1: Pion correction factor for the three types of tracks as a function of the momentum

Bibliography

[1] S. Eidelman et al. (Particle Data Group). Review of particle physics. *Physics Letters B*, 592/1-4, 2004.

[2] Q.R. Ahmad et al. Measurement of the rate of ν_e+d→p+p+e^- interactions produced by ^{8}b solar neutrinos at the sudbury neutrino observatory. *Physical Review Letters*, 87(7), 2001.

[3] Y. Fukuda et al. (Super-Kamiokande collaboration). Measurement of a small atmospheric ν_μ/ν_e ratio. *Physics Letters B*, 433:9–18, November 1998.

[4] http://www.phys.cmu.edu/∼clark/imb.html.

[5] Y. Fukuda et al. (Super-Kamiokande collaboration). Evidence for oscillation of atmospheric neutrinos. *Physics Review Letters*, 81:1562–1567, 1998.

[6] W.W.M. Allison et al. (Soudan-2 collaboration). The atmospheric neutrino flavor ratio from a 3.9 fiducial kiloton year exposure of soudan2. *Physics Letters B*, 449:137–144, 1999.

[7] S. Hatakeyama et al (Kamiokande collaboration). Measurement of the flux and zenith-angle distribution of upward through-going muons in kamiokande ii+iii. *hep-ex/9806038*, 1998.

[8] M. Ambrosio et al (MACRO collaboration). The macro detector at gran sasso. *Nuclear Instruments and Methods in Physics Research A*, 486:663–707, 2002.

[9] http://neutrino2004.in2p3.fr/.

[10] B.T.Cleveland et al. (Homestake collaboration). Update on the measurement of the solar neutrino flux with the homestake chlorine detector. *Nuclear Physics B (Proc. Suppl.)*, 38:47–53, 1995.

[11] W. Hampel et al. (GALLEX collaboration). Gallex solar neutrino observation: Gallex iii results. *Physics Letters B*, 388:384–396, 1996.

[12] J.N. Abdurashitov et al. (SAGE collaboration). The russian-americain gallium experiment (sage) cr neutrino source measurement. *Physical Review Letters*, 77:4708, 1996.

[13] Q.R. Ahmad et al. (SNO Collaboration). Direct evidence for neutrino flavor tranformation from neutral-current interactions in the sudbury neutrino observatory. *Physical Review Letters*, 89(1), 2002.

[14] T. Araki et al. Measurements of neutrino oscillation with kamland: Evidence of spectral distortion. *hep-ex/0406035*, 2004.

[15] C. Athanassopoulos et al. (LSND collaboration). Evidence for $\overline{\nu}_\mu \rightarrow \overline{\nu}_e$ oscillations from the lsnd experiment at los alamos meson physics facility. *Physical Review Letters*, 77(15), 1996.

[16] B. Armbruster et al. (Karmen collaboration). Upper limits for neutrino oscillations $\overline{\nu}_\mu \to \overline{\nu}_e$ from muon decay at rest. *Physical Review D*, 65:112001, 2002.

[17] I. Stancu et al. (MiniBooNE Collaboration). The miniboone detector technical design report. Technical report, FERMILAB-TM-2207.

[18] M.G. Catanesi et al. Proposal to study hadron production for the neutrino factory and for the atmospheric neutrino flux. *CERN-SPSC/99-35,SPSC/P315*, November 1999.

[19] B. Autin et al. Prospective study of muon storage rings at cern. In *cernrep 99-02*.

[20] S. Gilardoni. *Study of particle production and capture for a neutrino factory.* PhD thesis, University of Geneva, 2005.

[21] J. Collot et al. Pion production models and neutrino factories. *Nuclear Instruments and Methods in Physics Research A*, 451:327–330, 2000.

[22] A. Blondel et al. A thin target scheme for the muon source. *Nuclear Instruments and Methods in Physics Research A*, 451:349–352, 2000.

[23] T. K. Gaisser et al. Comparison of atmospheric neutrino flux calculations at low energies. *Physical Review D*, 54(9), 1996.

[24] M. Aguilar et al. (AMS collaboration). The alpha magnetic spectrometer on the international space station part i: Results from the test flight on the space shuttle. *AMS-06*, 2002.

[25] K. Aber et al. Measurement of proton, helium and muon spectra at small atmospheric depths with the bess spectrometer. *astro-ph/0304102*, 2003.

[26] L. Howlett. *Simulation and correction of cross-talk in the HARP Time Projection Chamber.* PhD thesis, University of Sheffield, 2004.

[27] S. Agostinelli et al. Geant4 – a simulation toolkit. *Nuclear Instruments and Methods in Physics Research A*, 506:250–303, 2003.

[28] M. H. Ahn et al.(K2K Collaboration). Indications of neutrino oscillation in a 250 km long-baseline experiment. *Physical Review Letters*, 90(4), 2003.

[29] A. E. Ball et al. Cngs:update on secondary beam layout. *SL-Note-2000-063 EA*.

[30] J. Altegoer et al. (NOMAD collaboration). The nomad experiment at the cern sps. *Nuclear Instruments and Methods in Physics Research A*, 404:96–128, 1998.

[31] E. Eskut et al. (CHORUS collaboration). The chorus experiment to search for $\nu_\mu \to \nu_\tau$ oscillation. *Nuclear Instruments and Methods in Physics Research A*, 401:7–44, 1997.

[32] V. Ableev et al. Tpg development. *Nuclear Instruments and Methods in Physics Research A*, 518:113–116, 2004.

[33] http://hep04.phys.iit.edu/cooldemo/.

[34] S.R. Amendolia et al. Tpc90, a test model for the aleph time projection chamber. *Nuclear Instruments and Methods in Physics Research A*, 252:392–398, 1986.

[35] http://www.vectorfields.com/files/html/products/opera3d.html.

[36] H. Wind. Processing magnetic field data. *Journal of Computational Physics*, 2:274–278, 1968.

[37] M. Bogomilov et al. The harp rpc time-of-flight system. *Nuclear Instruments and Methods in Physics Research A*, 508:152–158, 2003.

[38] G. Barr et al. Performance of multigap rpc detectors in the harp experiment. *Nuclear Instruments and Methods in Physics Research A*, 533:214–220, 2004.

[39] M. Anfreville et al. The drift chambers of the nomad experiment. *Nuclear Instruments and Methods in Physics Research A*, 481:339–364, 2002.

[40] M. Baldo-Ceolin et al. The time-of-flight tofw detector of the harp experiment: construction and performance. *Nuclear and Methods in Physics Research A*, 532:548–561, 2004.

[41] F. Bal. V451-cirq vme/vsb interrupt request module. *ECP/EDA DQ*, February 1993.

[42] M.G. Beuzekom et al. (CHORUS collaboration). The trigger system of the chorus experiment. *Nuclear Instruments and Methods in Physics Research A*, 427:587–606, 1999.

[43] R. Brun and F. Rademakers. Root - an object oriented data analysis framework. *Nuclear Instruments and Methods in Physics Research A*, 389:81–86, 1997.

[44] http://www.mysql.com/.

[45] CERN ALICE DAQ group. Date 3.5: Alice date user's guide. *ALICE 99/46 Internal Note/DAQ*, December 1999.

[46] http://lhcb-comp.web.cern.ch/lhcb-comp/frameworks/gaudi/.

[47] http://www.tcl.tk/software/tcltk/.

[48] A. Lundborg. Electrostatic simulation of parts of the harp tpc. HARP internal note 00-009, August 2000.

[49] G. Prior. The harp time projection chamber. *Nuclear Physics B. (Proc. Suppl.)*, 125:37–42, 2003.

[50] G. Vidal Sitjes. *The HARP Time Projection Chamber.* PhD thesis, Universidad de Valencia, 2003.

[51] S. Borghi et al. Clustering algorithm. HARP Memo 03-012, March 2003.

[52] M. C. Morone. *Evaluation of Silicon sensors for the ATLAS Silicon Tracker and TPC reconstruction in the HARP experiment.* PhD thesis, Université de Genève, 2003.

[53] R. Früwirth P. Billoir and M. Regler. Track element merging strategy and vertex fitting in complex modular detectors. *Nuclear Instruments and Methods in Physics Research A*, 241:115–131, 1985.

[54] R. Frühwirth. Application of kalman filtering techniques to track and vertex fitting. *Nuclear Instruments and Methods in Physics Research A*, 262:444–450, 1987.

[55] A.Grossheim. *Particle production yields induced by multi-GeV protons on nuclear targets.* PhD thesis, University of Dortmund, December 2003.

[56] Vladimir Ivantchenko and Hans-Peter Wellish: private communication.